©2019 Erik Huemiller

PROBING PROXIMITY-INDUCED SUPERCONDUCTIVITY IN Nb- Bi_2Se_3 BILAYERS WITH LOW-TEMPERATURE TRANSPORT AND JOSEPHSON INTERFEROMETRY

BY

ERIK DAMON HUEMILLER

DISSERTATION

Submitted in partial fulfillment of the requirements
for the degree of Doctor of Philosophy in Physics
in the Graduate College of the
University of Illinois at Urbana-Champaign, 2019

Urbana, Illinois

Doctoral Committee:

Professor Nadya Mason, Chair
Professor Dale J. Van Harlingen
Associate Professor Smitha Vishveshwara
Associate Professor Virginia D. Lorenz

ABSTRACT

Superconductors and topological insulators are two condensed matter systems that differ at the most fundamental level. Superconductors, discovered serendipitously, spontaneously break gauge symmetry. In contrast, topological insulators are defined by a topological invariant of their band structure. Theoretical work in 2008 proposed a novel way to engineer an exotic superconducting system using the proximity effect to blend the electronic properties of these two systems. They showed that the resulting system resembles a spinless p-wave superconducting Hamiltonian.

This work explores the limits of Hamiltonian engineering in superconductor-topological insulator bilayers made of niobium and bismuth selenide. Low temperature transport measurements demonstrate the presence of proximity-induced superconductivity in the topological insulator thin film. Non-local measurements show a surprising nonlocal signal at low bias that is odd in the bias on both contacts. Sharp high bias resistance dips exhibit unexpected behavior as a function of the opposite bias. With proximity-induced superconductivity established in the topological insulator film, Josephson interferometry measurements were conducted with a niobium – bismuth selenide bilayer as one of the contacts. Corner junctions show evidence for critical current asymmetry between the two halves of the junction. The critical current versus field measurements are compared with numerical simulations to rule out possible alternative explanations. Signatures attributed to p-wave superconductivity in other work such as chiral domains and asymmetrical diffraction patterns were not observed. This collection of work provides an original contribution to the body of work exploring the superconducting properties of Nb-Bi_2Se_3 bilayers.

To my grandparents
Clarence, Avilda, Anna, and Richard

ACKNOWLEDGEMENTS

First off, I would like to thank my advisor Dale Van Harlingen for his mentorship and financial support over the years. His mentoring style has provided me the freedom to explore, experiment, fail, and ultimately learn a great deal personally and professionally while in graduate school. The post docs I have worked with, Vlad, Aaron, Cihan, Vincent, and Guang have been invaluable resources, teaching me numerous details from sample fabrication to cryogenic measurements and everything in between. They have also been unending testers of my fundamental understanding of the physics behind the equipment we use, and for that I thank them. David, Kenny, Can, Lu, Adam and the rest of the DVH crew, you made the timely lunches, long nights, group meeting discussions, and March Meeting trips a time to remember. I don't think there is anyone I spent more time with than you, and it wouldn't have been the same without you.

The members of the physics department have been invaluable in providing support as collaborators and friends while in graduate school. Working with theory collaborators Moon Jip and Suraj who have been willing to answer endless questions about the theoretical underpinnings of our work. Lance Cooper has provided an excellent resource for getting feedback in times of need and on short notice. I am also grateful to the resources and staff at the Seitz Materials Research Lab at the University of Illinois, without which this research would have failed

Despite the long hours, my time in Urbana was not solely spent in the lab, and the support of friends and family has made this a great place to live. My family, Laura, Tim, Karl, and Adel have been unending sources of support, even with long distance and infrequent phone calls. Phil, Sean, and Garret, living with you for the last few years has been great from the late nights, to the road trip, and 4th of July BBQs. The PGSA provided an avenue to make connections in the department and explore my creativity at the Physical Revue. The ultimate community, from Prion to the Majorana Meatballs, have provided me with a reason to stay active while making lasting friendships that have been an evening keel in turbulent times. To Kate, I am grateful for her unending support and for ensuring this thesis was finished despite hell, high water, and a hurricane of other priorities that cropped up. Lastly, I would like to thank my committee for being a part of my defense. It is an important moment for me and you helped make it possible.

This work was carried out in part in the Materials Research Laboratory Central Facilities at the University of Illinois at Urbana/Champaign and was funded by grants from the Microsoft Station Q and under NSF Grant DMR-1411067.

Table of Contents

1. Introduction

1.1 Superconductivity - Experimental Signatures and Theoretical Descriptions

Superconductivity (SC) is a macroscopic quantum phenomenon that has intrigued condensed matter physicists for over a century[1]. This bizarre state of matter that forms below a critical temperature is marked by three experimentally verifiable characteristics. Most well-known is the property of zero DC electrical resistance[2] discovered in mercury in 1911. Additionally, as Meissner discovered in 1933, superconductors expel magnetic fields from within their bulk[3], even when cooled in field[3], [4]. The last of the experimental hallmarks was first seen in heat capacity[5] and electromagnetic absorption measurements[6], [7] that showed evidence for a gap in the electronic density of states far below the critical temperature of the material. To this day, new materials need to exhibit these characteristics to be classified as superconductors[8].

The underlying physics of SC proved to be a formidable foe with two theoretical frameworks emerging as the culmination of several decades of work. At the University of Illinois, Bardeen, Cooper, and Schrieffer developed a microscopic picture based on pairs of electrons condensing into a charged superfluid condensate[9]. The Cooper pairs, as they are known, are made up of opposite spin electrons in a singlet state coupled via the weak electron-phonon interactions in the material[4], [9]. The other main framework that is used to describe superconducting systems is the phenomenological theory of phase transitions developed by Ginzburg and Landau (G-L)[10]. The foundation of G-L theory lies in minimization of free energy density and the formation of a condensate described by a single pseudo wave function $\Psi = \Psi_0 e^{i\phi}$, known as the superconducting order parameter[4], [11]. This order parameter can vary on a length scale ξ, called the coherence length, and can spill over into adjacent conducting materials in close

proximity to the SC[4]. In 1959, Gor'kov showed that G-L theory could be derived from BCS theory in the limit of the temperature being "in the neighborhood of Tc"[12] with the BCS gap function being related to $|\Psi|^2$. The ability of these two theoretical frameworks to describe SC spurred an abundance of research into applications and fundamental tests of SC systems[4], [13].

1.2 Topological Insulators – Negative Mass and Spin-Momentum Locked Surface States

In contrast to superconductors, topological insulators (TI) are a class of materials that have exotic surface electronic states resulting from the topology of their electronic band structure in the bulk[14], [15]. In materials with strong enough spin-orbit coupling, the valence and conduction bands invert in the bulk of the material. This results in two regions in real space next to each other that are band gap insulators with different band topology[14]. In considering the electron energies of the relativistic form[14]

$$E = c\sqrt{p^2 + m^2c^2}, \tag{1.1}$$

this topologically non-trivial property of the material is captured by a negative effective mass. This negative mass results in there needing to be a gapless point in real space, at the boundary between the two materials[15]. This boundary state with no gap to excitations results in a topologically protected conduction channel. Instead of the conducting electronic state being the result of a global order parameter, in these systems the state is a result of the band inversion, which is a property of the material's bulk.

1.3 Hamiltonian Engineering - Proximitized Topological Insulators

In 2008, Fu and Kane considered combining these two materials to engineer a Hamiltonian[16] that resembles that of an unconventional superconductor. Although conventional SC is relatively well understood with BCS and G-L theory[4], [11], unconventional superconducting systems remain open topics of research to this day[17]. They found that at the

interface between the conventional SC and the TI, where the spin and superconducting properties of the two systems blend, a Hamiltonian resembling spinless $p_x + ip_y$ $\mathrm{p_x + ip_y}$ SC emerged[16]. This type of SC is particularly rare; the other candidate is Sr_2RuO_4[17], [18], a material that is hard to work with and full of confounding results[18], [19]. Fu and Kane also found that these systems could be the host to Majorana Fermions[16], particles that are their own anti-particle[20]. These Majorana particles also obey non-abelian statistics, which means their history influences the state they are in[21]. This non-abelian property can be harnessed to make a topological quantum computer[22], a fascinating topic that is beyond the scope of this thesis.

1.4 This Work - Objective and Organization

The goal of this work is to explore the boundaries of Hamiltonian engineering by probing the properties of the superconductor-topological insulator interface proximity region with two experiments. The first experiment investigates the effect of spin injection on the local and non-local transport in three terminal devices made of Bi_2Se_3 and Nb thin films. The second experiment is targeted at gaining insight into the properties of the order parameter in Nb-Bi_2Se_3 bilayers using Josephson interferometry. Organizationally, this thesis will continue from Ch 1 to a more rigorous overview of topological insulators in Ch 2, specifically the Bi_2Se_3 thin films these devices are made from. In Ch 3, relevant background theory on the proximity effect, transport and Hamiltonian engineering will be covered. Unique technical challenges for this research will be included in Ch 4. Three terminal device data will be presented and analyzed in Ch 5 before Ch 6 where measurements of corner and edge junctions on Nb-Bi_2Se_3 will be presented. The main text will conclude with Ch 7 which will bring things back together and propose future directions to continue this work. The appendix will include more details on the Josephson interferometry simulations I adapted to MATLAB for the numerical analysis in this thesis.

2. Topological Insulators

The recent recognition of the work by Haldane[23], Kosterlitz[24], [25], and Thouless[24]–[26] by the Nobel Committee[27] is the culmination of decades of research into systems that are defined by topological invariants rather than broken symmetries. In this chapter I will begin by introducing topological invariants in the band structure of topological insulator (TI) systems before presenting their first experimental realization in two and three dimensions. I will then present the road map that led to the development of the thin films grown by molecular beam epitaxy (MBE) that I worked with in this thesis.

2.1 Topology Applied to Band Theory

Although this topic is often reduced to comparing oranges and bagels[14], the topology in TIs is in fact a quantitative method for describing how two seemingly similar systems are fundamentally different. In conventional band insulators, the electronic structure around the Fermi energy has a gap in the density of states, leaving no states for small excitations of electrons for conduction[28]. With strong spin-orbit coupled materials, there can be a similar gapped electronic structure; however, the conduction band and valence band in the material are inverted relative to those of an ionic insulator or the vacuum[14]. At the real space boundary between these two types of materials, there must be some region where the two bands cross each other, providing a surface state that is robust to smooth transformations of the Hamiltonian. This surface state is protected by the topology of the band structure and can provide gapless states near the Fermi energy for small excitations, depending on the topology of the bands[29].

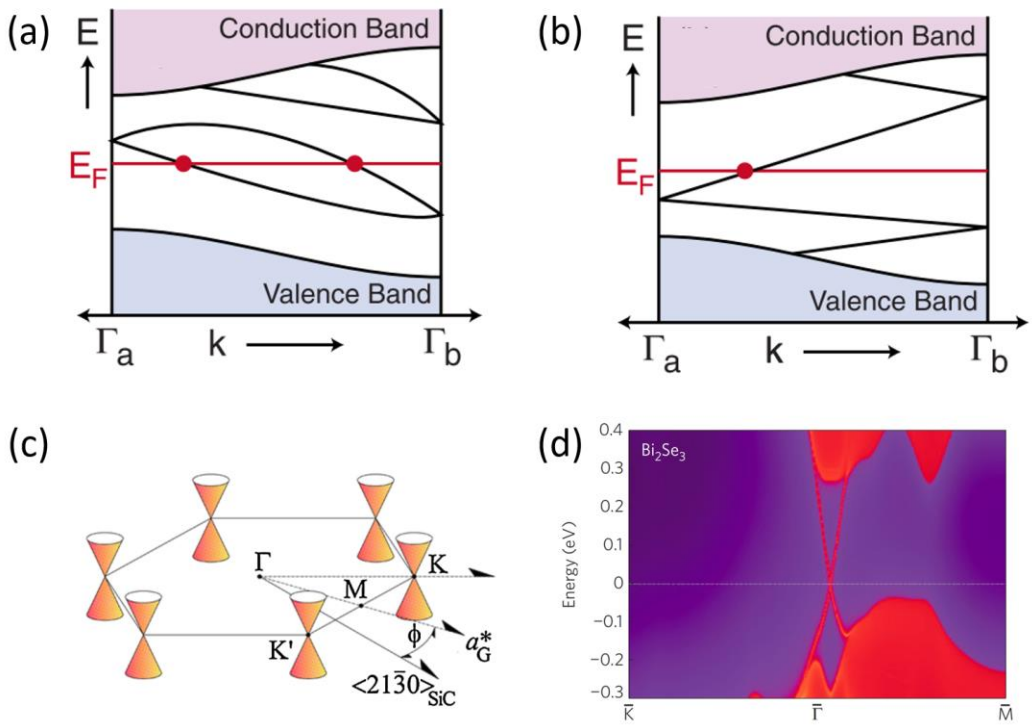

Figure 2.1 Two possible 1-D surface state band structures (a, b) between high symmetry points in the Brillouin zone[14] of a time reversal symmetric material. In the case of an odd number of Fermi energy crossings (b), there is a topologically protected conducting surface state. For 2-D materials, the number of crossings is generalized to the number of Dirac cones. The band structure for graphene[30] (c) has 6 crossings while the band structure for Bi_2Se_3 (d) has a single Dirac cone, and a topologically protected conduction channel[31].

This phenomenological understanding of TIs can be quantified by counting the number of Kramer's degenerate states in the surface band structure that cross the Fermi energy between high symmetry points in the Brillouin zone[15]. Kramer's theorem states that "if a system composed of an odd number of spin ½ particles has a Hamiltonian that is invariant under time reversal, then all its stationary states are degenerate" (p 292)[32]. Between high symmetry points, the degeneracy is satisfied by symmetry about zero momentum. The spin-orbit coupling of the TI splits the spin degeneracy of the states at any one point without breaking the symmetry about zero momentum. At the Dirac point this does not hold and the bands converge to maintain the double degeneracy dictated by Kramer's theorem[29]. The topological protection of the conducting

surface state is encoded in which 2 bands are connected at adjacent high symmetry points. If the bands at adjacent symmetry points are the same, then the conduction of the surface state is not guaranteed by the band topology. This is the case where an even number of Fermi level crossings are present. If the two bands that contribute to the degeneracy are of different origins, then there will be an odd number of Kramer's degenerate pair-crossing the Fermi energy, and the conducting surface state will be topologically protected[14]. This is illustrated in Figure 2.1 Two possible 1-D surface state band structures (a, b) between high symmetry points in the Brillouin zone[14] of a time reversal symmetric material. In the case of an odd number of Fermi energy crossings (b), there is a topologically protected conducting surface state. For 2-D materials, the number of crossings is generalized to the number of Dirac cones. The band structure for graphene[30] (c) has 6 crossings while the band structure for Bi_2Se_3 (d) has a single Dirac cone, and a topologically protected conduction channel[31].Figure 2.1 where the surface bands that connect at adjacent high symmetry points can either be the same pair or different. In 3D materials, the surface states are 2D in nature, and counting the number of crossings is analogous to counting the number of Dirac cones in the Brillouin zone[29]. An odd number of Dirac cones is the signature of a topologically protected conduction channel at their surface, while an even number indicates a lack of topological protection[15].

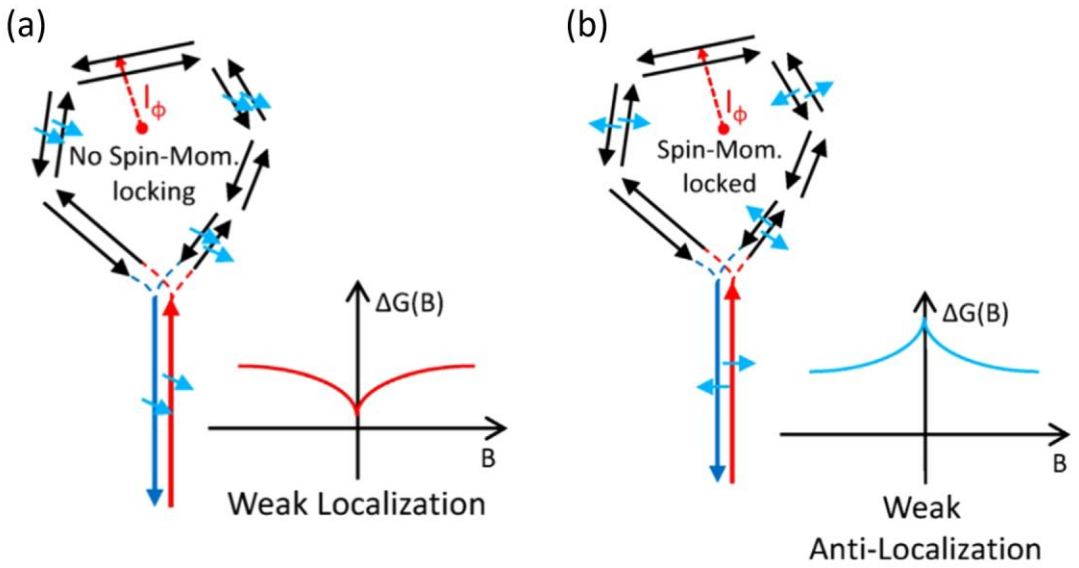

Figure 2.2 Possible underlying mechanisms of weak localization (a) and weak anti-localization (b) are shown with their effect on magneto conductance measurements. In conventional metals, counter propagating trajectories will constructively interfere (a) to enhance backscattering at low field. Conversely, in materials with a Berry phase of π as in (b), the disordered paths of backscattered electrons will interfere deconstructivly, causing a suppression of backscattering at low field[33]. Demonstrating weak anti-localization in samples is commonly used to show that there is suppressed backscattering in topological insulators. This is effect is expected from the spin-momentum locking induced Berry phase of π between electrons that trace out a closed path in momentum space[14].

Strong spin-orbit coupling can lead to the band inversion characteristic of 3D TIs, and it results in spin-momentum locked surface states together with suppressed backscattering from nonmagnetic impurities. In these materials, the spin degeneracy of the electronic states is split by the spin-orbit coupling strength. Due to Kramer's theorem and the spin-orbit Hamiltonian's time reversal symmetry invariance, the surface states with opposite momentum must have opposite spin[14]. This spin-momentum locking results in a Berry phase contribution to the wave function of the particle. The Berry phase is a geometrical phase that the particle accumulates due to adiabatic changes in the Hamiltonian based on the path it takes in the material[23]. Due to the winding of the spin around the Brillouin zone, the Berry phase contributed is π for any particle that takes a path around the Dirac point in momentum space, as illustrated in Figure 2.2. With a phase

of π, the reflected particle destructively interferes with the incoming particle. This destructive interference results in a reduction of the effects of nonmagnetic disorder, and the realization of weak anti-localization[33].

2.2 Experimental Realization of 3D Topological Insulators

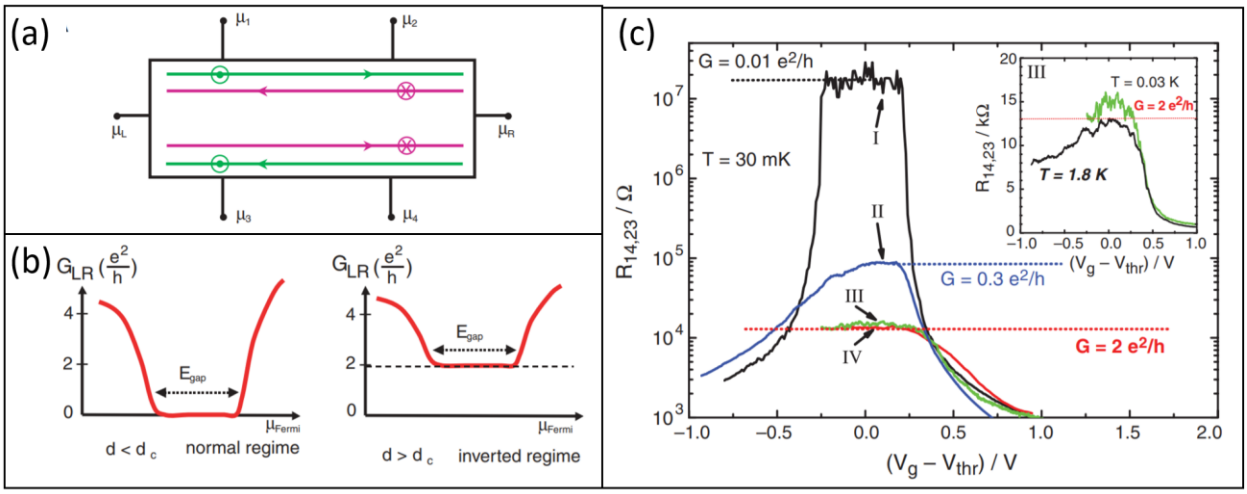

Figure 2.3 Schematic of HgTe devices (a) predicted to demonstrate the existence of a quantum spin Hall insulator[34]. Depending on the thickness of the HgTe well as shown in (b), the 6 terminal device conductance would plateau to $0\ e^2/h$ or to $2\ e^2/h$ with *e* as an electronic charge and *h* representing Planck's constant. In the figure, *d* is the thickness of the quantum well and d_c is the critical thickness where band inversion occurs[34]. Data from the first realization of a quantum spin Hall insulator (c) shows resistance plateaus for different thickness quantum wells[35]. Sample I (*d*: 5.5 nm, area: 20.0 mm × 13.3 mm) is in the normal regime while samples II-IV (*d*: 7.3 nm, area: 20.0 mm × 13.3 mm, 1.0 mm × 1.0 mm, and 0.5 mm × 1.0 mm respectively) are samples with inverted bands. Comparison of samples III and IV show that the quantization of transport does not depend on the width of the device which is evidence of edge channel localized conduction[35].

The suitability of band theory to describe the interesting phenomena in TI systems has enabled theoretical predictions to lead experimental progress in the field for several years. In 2006, Bernvig Hughes and Zhang (BHZ) predicted that HgTe quantum wells could be used to make a 2D material with band inversion tuned by the quantum well thickness as seen in Figure 2.3[34]. Shortly thereafter, the group led by Laurens Molenkamp grew and characterized these precise materials, realizing a quantum spin Hall insulator for the first time[35]. This experimental

breakthrough was followed by further theoretical work that expanded the band inversion principle to 3D materials with strong spin-orbit coupling, and predicted that the analogous effect could be seen in a $Bi_{1-x}Sb_x$ alloy[29]. The angle resolved photo emission spectroscopy (ARPES) measurements that followed showed five band crossings in the Brillouin zone, indicating that $Bi_{1-x}Sb_x$ was a 3D TI, the first of its kind[36]. In follow up work by Fu and Kane from 2008, band structure for $Bi_{1-x}Sb_x$ calculations corroborating and extending the conclusions drawn from the experimental observations were published[37].

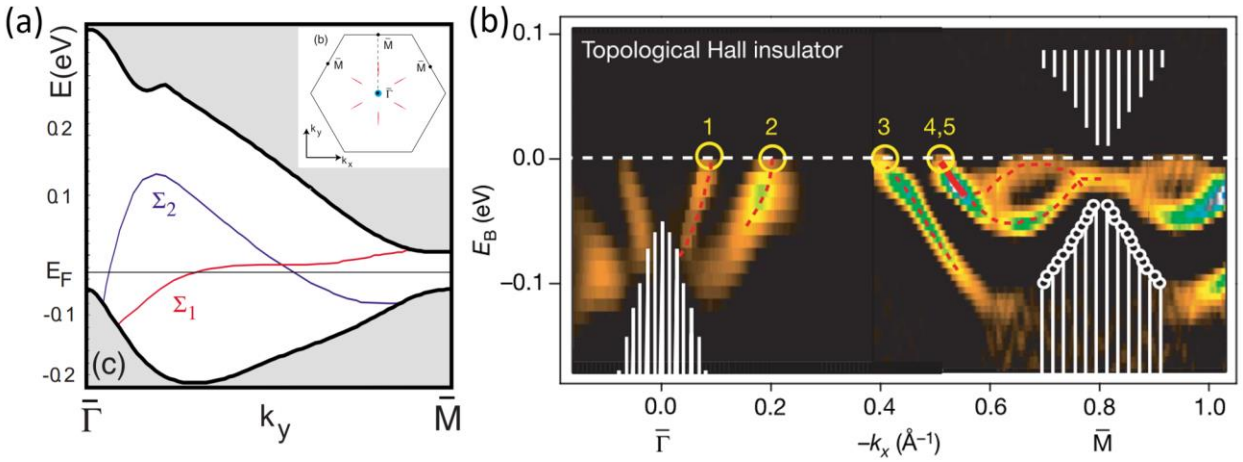

Figure 2.4 Calculated[37] (a) and measured[36] (b) band structures of $Bi_{1-x}Sb_x$, the first 3-D topological insulator discovered. The calculation in (a) shows three surface state Fermi energy crossings, evidence for a topologically protected conducting channel. The data in (b) is the second derivative of the surface band dispersion of $Bi_{0.9}Sb_{0.1}$ and shows five total crossings. The Fermi energy crossings are shown with yellow circles including the doubly degenerate 4/5 circle shown. The red lines are used as a guide, and the data could be reproduced[36] by an in-plane rotation of 60º. The authors of the calculation attribute the discrepancy to their lack of use of self-consistency on the surface potential, which could lead to an additional Kramer's pair-crossing[37].

2.3 The Next generation of 3D Topological Insulators

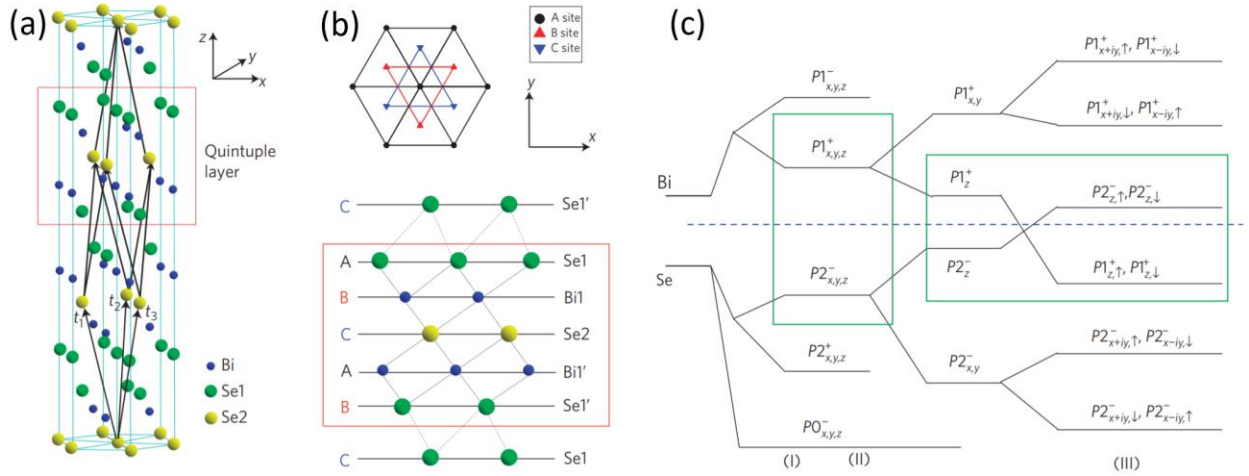

Figure 2.5 Bi_2Se_3 crystal structure and band structure calculations. A 3-D rendering of the Bi_2Se_3 crystal structure (a), highlighting the two selenium atom sites, and the quintuple layer (QL) structure that the material is built from. Top view of the crystal structure (b) showing the alignment of the different sites within the QL as well as a side projection of the layering with a single QL highlighted. c) Evolution of the p-orbital energies in Bi and Se with inclusion of incrementally more components of the Hamiltonian. Region I includes chemical bonding, II includes crystal field splitting, and III includes spin-orbit coupling. With the inclusion of all the effects, two of the levels invert across the Fermi energy, making it a topological insulator[31].

After the initial realization of 3D TIs in BiSb, the community pushed to find materials that were better suited to growth optimization, and easier to measure. Again, the group led by Shou Cheng Zhang blazed the way forward by calculating[31] the band structure of Bi2Te3, Bi_2Se_3, Sb2Te3, and Sb2Se3. These four materials are stoichiometric combinations of elements that reduce the possibility of disorder due to inhomogeneity in the materials, as seen in $Bi_{1-x}Sb_x$. The base unit cell of these materials is a quintuple layer (QL) made up of alternating types of atoms, as shown in Figure 2.5. For each of the four materials, the authors examined the electronic structure to determine if they hosted topologically protected surface states. By looking at the parity the of the lowest unoccupied band at the high symmetry points and the total product parity of the bands in each material, they predicted that Sb_2Se_3 did not have a surface state, while the other three materials considered would exhibit topologically protected surface states due to the parity of their

band structure. The band structure density functional theory calculations they present confirm that the three materials with odd parity[31] have gapless surface states that bridge the bulk band gap as can be seen in Figure 2.6.

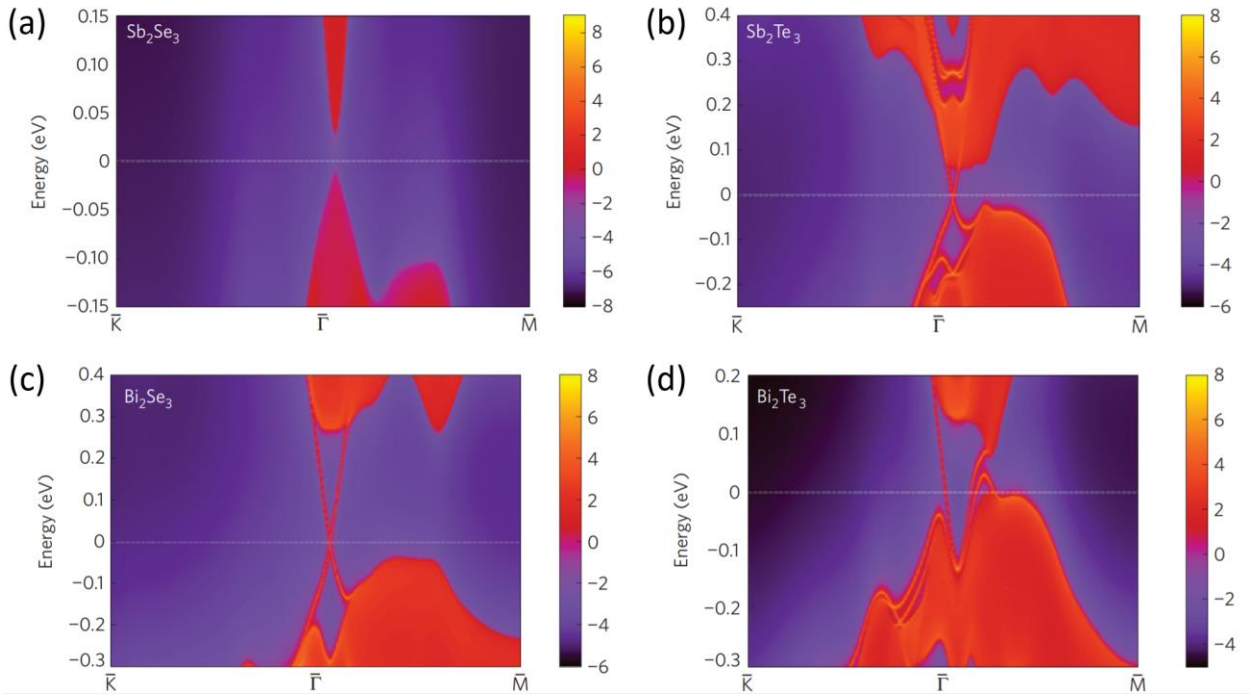

Figure 2.6 Band structure of 4 second generation stoichiometric topological insulator candidates. The band structure of Sb_2Se_3 (a) shows a clear energy gap but does not show any surface states bridging the two bands. Sb_2Te_3 (b) exhibits a small band gap with linear dispersing surface states that bridge the bulk bands. In the case of the Bi_2Se_3 band structure calculation (c), there is a large semiconducting gap with clear surface states connecting the valance band to the conduction band. In Bi_2Te_3 there is a small semiconducting gap with linearly dispersing surface states. In this case, the Dirac point falls below the bulk bands and, as a result is not in the gap[31].

Of the three materials with topologically protected surface states they considered, Bi_2Se_3 has several technical advantages that make it an attractive material to work with. According to Hassan and Kane, the 0.3 eV bulk band gap and the single Dirac cone with near ideal dispersion are the two most prevalent reasons why Bi_2Se_3 provides a good platform to explore the physics of TIs. The relatively large bulk band gap, an order of magnitude larger than room temperature energy scales, enables the possibility of seeing topological physics at room temperature. The near ideal dispersion as observed in experiment and predicted by theory enable more straightforward

future work on the material[14]. In addition to these technical reasons, the experimental tests that demonstrate the properties of a TI have been well established on Bi_2Se_3, including spin-momentum locking of the surface state, the Berry phase of π, susceptibility to magnetic disorder, and robustness to nonmagnetic dopants on the surface[38].

2.4 Bi_2Se_3 Thin Films grown by Molecular Beam Epitaxy

One challenge that Bi_2Se_3 presents is separating surface state conduction from the bulk conduction which occurs due to Se vacancy n-doping and interface induced disorder[39]. Increasing the ratio of surface to bulk conduction with thin films and p-doping with Ca are strategies being implemented to highlight surface effects. Among the groups developing thin films of Bi_2Se_3, Seongshik Oh's group at Rutgers has led the way in terms of producing low carrier concentration and high mobility films. Over the last 10 years they have iteratively improved the material quality of their molecular beam epitaxially grown films by reducing interface induced disorder. The first successful process was developed in 2011 and involved a growth process consisting of two temperature steps on a Si (111) surface[40]. These films were the first example of atomically sharp films grown on Si (111) without the use of a Bi reconstructed surface to achieve[41] a clean interface between Si and the Bi_2Se_3. The next step along the path to better films was to use c plane sapphire substrates, which have a better lattice matching to Bi_2Se_3 than the Si (111) surface. This adjustment was shown to produce films that had constant resistance per square for films from 4 to 250 QL thick[42]. These films exhibited a weak anti-localization peak in magneto-resistance that was consistent with a two-carrier model, accounting for the topologically protected surface state and a normal 2-dimensional electron EG) resulting from band bending at the TI surface.

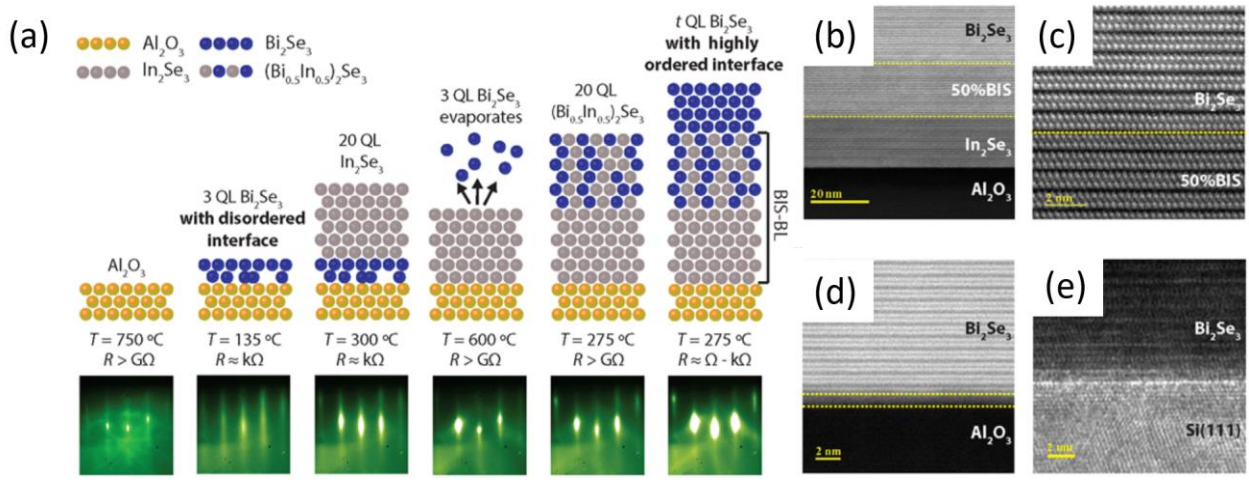

Figure 2.7 The process of growing high quality buffered Bi_2Se_3 (a) thin films via molecular beam epitaxy (MBE) requires a nontrivial process. A thin Bi_2Se_3 layer is grown at low temperature to act as a seed for 20 quintuple layers (QL) of In_2Se_3. This layer will be the foundation of the entire film. The initial Bi_2Se_3 layer is evaporated with a high temperature anneal before growing a BiInSe layer. The BiInSe layer provides clean atomic interfaces with both the InSe grown before and the Bi_2Se_3 film that will be grown on top. The last step is to grow a Bi_2Se_3 film of the desired thickness on top of the BIS buffer. Displayed below each step are the resistance and the reflective high energy electron diffraction pattern (RHEED) used to track film quality during growth. Transmission electron microscope images of the atomically sharp BIS-BS (b) and BiSe-BIS (c) buffer layer in these films. The low bulk carrier concentration is attributed to the clean interface between the BiSe and the BIS buffer layer shown in (c). Two other common BiSe growth platforms that do not exhibit atomically sharp interfaces are BS-AlO (d), and BS-Si (e) thin films[39].

To continue the progress of improving film quality by reducing the carrier concentration, an insulating BiInSe buffer layer to go between the Bi_2Se_3 and the Al_2O_3 was developed[39]. This had the effect of reducing the carrier concentration by another order of magnitude compared with the Al_2O_3 grown films. In Figure 2.7 the carrier concentration and mobility are compared, showing the improvement of these characterization values for the buffered films over the Al_2O_3 grown films. ARPES measurements were also conducted, showing a Dirac point that is a factor of 2 closer to the Fermi energy when compared to the samples grown on Si. The reduction in the energy of the Dirac point is critically below the bottom of the bulk conduction band that confound transport signatures. These films provide a high-quality TI for exploring the properties of TIs in an experimentally useful package.

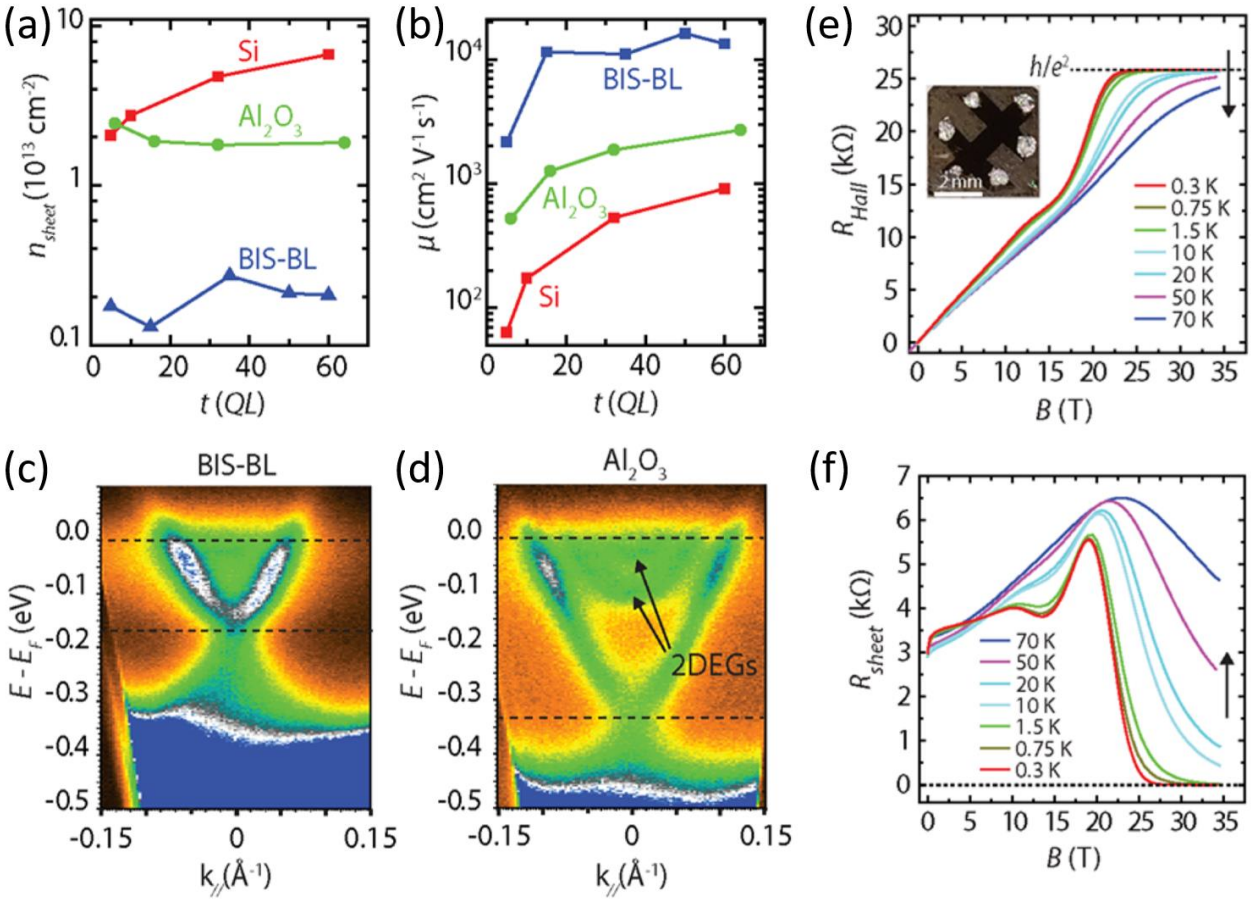

Figure 2.8 High quality films of Bi_2Se_3 grown on BIS buffer layers at Rutgers display lower carrier concentrations (a) and higher mobilities (b) than Bi_2Se_3 grown on other common substrates. The quality of the films is compared via angle resolved photo emission spectroscopy (ARPES) results with Bi_2Se_3 grown on Al_2O_3 substrates. Measurements of the Hall resistance (e) and the sheet resistance (f) at high field show quantization of the conductance, evidence for extremely high mobility surface states in these films.

3. Superconductivity

3.1 Transport at Superconductor-Normal Metal Interfaces

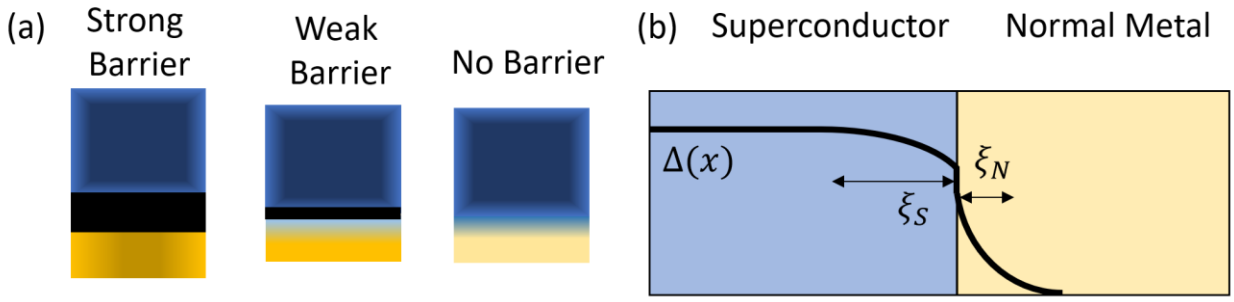

Figure 3.1 When a superconductor is placed in contact with a normal metal, the properties at the interface blend the properties of the two. An insulating barrier between the two will weaken the blending (a), reducing the superconducting correlations in the normal metal. Near the interface, the superconducting gap changes over a length scale dictated by the material (b). With an interfacial barrier, the gap strength has a discontinuity that depends on the barrier strength shown at the interface between the superconductor and the normal metal.

Of all the fascinating aspects of superconductivity (SC), the focus of this research is in its ability to engineer exotic physics by inducing its most exotic properties in a material it is contacting. A simple example of this can be seen near the interface of a superconductor with a normal metal. The practical electronic transport in this region is described by Eilenberger's work[43] where he takes the limiting case of Gorkov's[12] equations near the Fermi energy. He also includes averaging over impurity positions resulting in a simplified description of transport in the proximity region. For the case of diffusive metals, where the coherence length is shorter than the mean free path in the metal, Usadel applied Eilenberger's result to the case of a dirty superconductor[44]. The Usadel equations express the microscopic transport of electrons in the a regime where transport processes are dominated by effects dictated by the diffusion constant in the metal, the diffusive regime. In this regime, the transport in a metal near the interface of the normal metal and a superconductor exhibits properties of both materials on a length scale determined by scattering in the normal metal. The work in this thesis seeks to test the boundary

of engineering exotic superconducting states by harnessing the proximity. The system of interest is a normal s-wave superconductor in contact with the surface states of a TI, a system that has been predicted to host exotic superconducting correlations. To understand what signatures of exotic phenomena will look like, a review of transport across superconductor-normal metal interfaces will be presented before addressing the current state of SC-TI interface transport.

3.1.1 Theory of Tunneling by Blonder–Tinkham–Klapwijk (BTK)

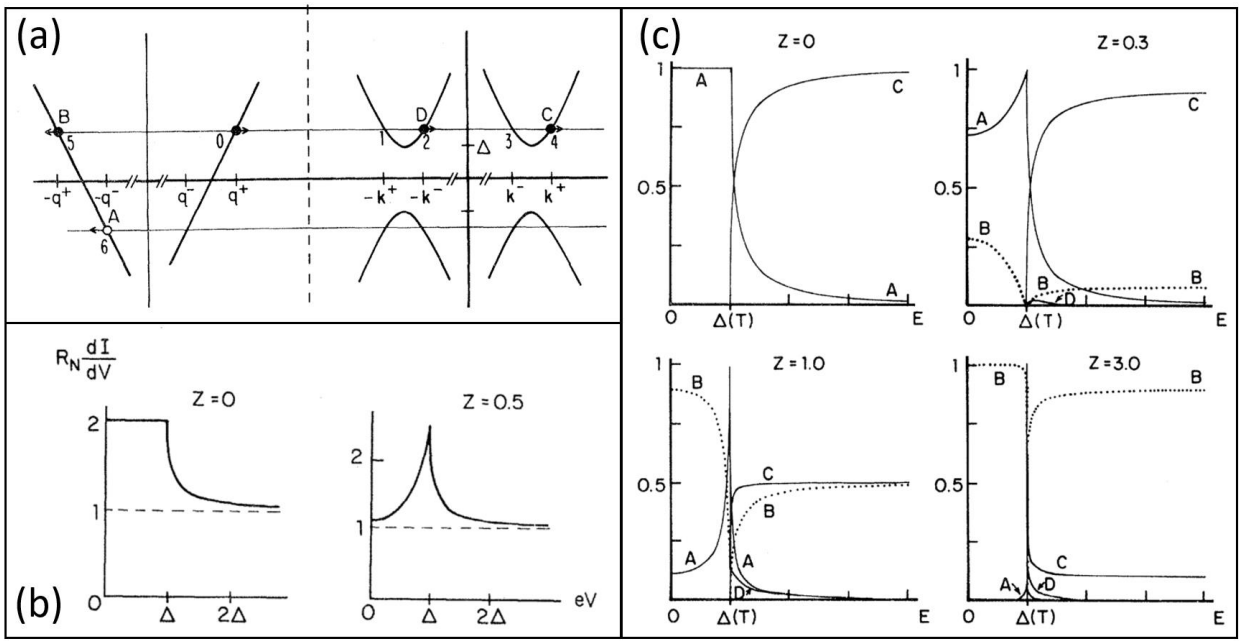

Figure 3.2 Blonder-Tinkham-Klapwijk's theory of superconducting-normal metal tunneling provides a description of the possible outcomes of an incident electron (a). It can reflect as a hole with opposite momentum in channel A, as an electron with opposite momentum in channel B, or enter the superconductor as a quasiparticle above the superconducting gap with or without a branch crossing in channels D and C respectively. For a given superconductor and temperature, the probabilities of each outcome depend on the strength of the interfacial barrier. Two examples (b) of the differential resistance at barrier strength Z = 0 and z= 0.5 versus bias voltage show that for a higher barrier the zero bias conductance is reduced. The probabilities of each outcome are calculated for four different interface strengths. At low Z, Andreev reflection (A) where the electron creates a Cooper pair and retro reflects a hole dominates the conductance. In the opposite extreme of high Z, a sub-gap electron is most likely to be reflected as a counter propagating electron back into the lead (B). The intermediate barrier strengths show a crossover between the two limits with either Andreev reflection or backscattering dominating.

The transport across the interface of a SC-normal metal interface is described with the theory developed by BTK in in 1982. They consider an incident electron from the normal metal side of a normal metal-superconductor junction[45]. The incident particle could reflect a hole in the process of creating a Cooper pair that is added to the condensate, a process known as Andreev reflection. Normal reflection is the second case, where it is reflected with opposite momentum back into the normal metal. With enough energy, the electron can also pass into the superconductor as a quasiparticle. The quasiparticle trajectory can either be on the same side of the Fermi surface, without a branch crossing, or it can transfer across the interface with branch crossing, ending up on the opposite side of the Fermi surface. To obey particle conservation, the probabilities of each of the paths must add up to unity. The unique aspect of BTK theory is its inclusion of an interface barrier parameter, Z. The probabilities of each of the channels is shown in Figure 3.2c. In tuning the interface parameter, BTK theory can describe a wide variety of transport behavior at normal metal superconductor interfaces. For low Z transport, Figure 3.2c shows that Andreev reflection (A) dominates over the other possible trajectories. Above the gap, the incident electrons are transferred into the superconductor as quasiparticles without branch crossing for the low barrier case. Figure 3.2b shows the differential conductance for low barrier strength junctions showing an enhancement of the conductance from the sub-gap Andreev reflection.

3.1.2 Local Transport in Topological Insulator-Superconductor Devices

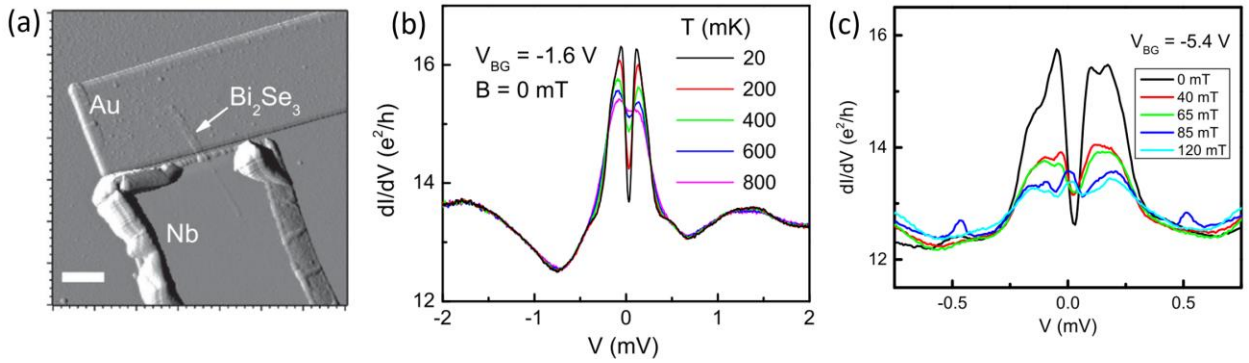

Figure 3.3 Previous work[46] by A. Finck *et al.* on superconductor-topological insulator devices investigated small devices with gold counter electrodes (a). The scale bar in (a) is 1 μm with the Nb-Au separation being reported as 230 nm measured with a scanning electron microscope. The temperature (b) and magnetic field (b) dependence of the device conductance shows an enhancement at low finite bias voltage that is interpreted as evidence for proximity-induced superconductivity in the Bi_2Se_3 wire. The suppression of conductance near zero bias is representative of reentrant resistance suppressing the superconducting correlations in the Bi_2Se_3 that are also suppressed with temperature and magnetic field.

TI-SC devices have been shown to exhibit transport consistent with BTK theory in the low barrier regime[46]. Using exfoliated Bi_2Se_3 and evaporated Au, junctions were made with a TI section 100-250 nm long as shown in Figure 3.3a. At low temperature, the authors report a zero-bias suppression of the conductance that is flanked on either side by an enhancement. The conductance dip is attributed to reentrant resistance at energies below the Thouless energy, an effect that scales inversely with the dimension of the proximity region squared. The enhancement of conductance at zero bias is attributed to Andreev reflection, which can be suppressed by thermal fluctuations in temperature, and pair-breaking by a magnetic field. The authors include a top gate in their device and focus their study on their ability to tune the chemical potential in the device, adjusting the Fermi wavelength of the electrons. They explore the changes in universal conductance fluctuations as a function of field and gate voltage, showing that there is a doubling of the frequency from outside the SC gap energy to inside it.

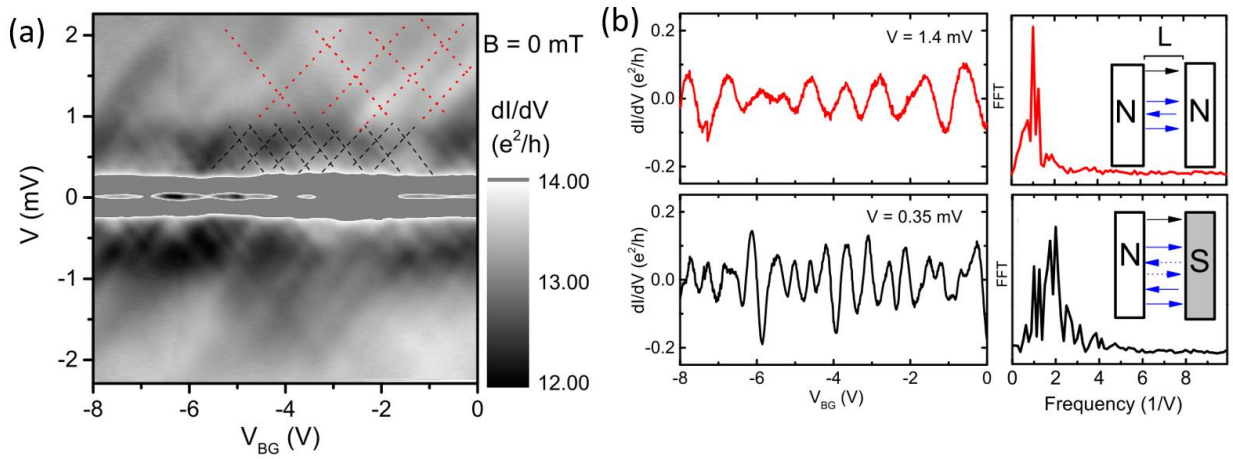

Figure 3.4 The gate dependence of the conductance in Nb-Bi_2Se_3 devices was shown to exhibit a doubling in frequency of oscillations. The full 2D sweep (a) of device conductance as a function of bias voltage and back gate voltage show two regimes. The red and black lines are guides to the eye showing the normal and superconducting regimes. Taking the Fourier transform of high (red) and low(black) gate sweeps shows a significant increase in the second harmonic. The authors argue that the doubling is a result of Andreev resonances when the bias is inside the gap. At high bias, the incident electrons become quasiparticles inside the superconductor[46].

3.1.3 Nonlocal Transport in Superconducting Systems

For devices with a second lead contacting the SC a short distance away, two more processes are possible that are a result of the nonlocal nature of the Cooper pairs[47]. The first process is crossed Andreev reflection (CAR), whereby an incident electron creates a Cooper pair with an electron in the other lead, Andreev reflecting a hole into that lead with opposite momentum of the second electron. This process has been proposed as a platform for creating entangled electron pairs for quantum computation. In an alternative to CAR, the incident electron can quantum mechanically tunnel from the incident lead into the opposite lead via elastic co-tunneling. These two processes can be experimentally differentiated by the sign of the current in the opposite lead. In BCS theory, the size of the Cooper pair is approximated by the coherence length[4], so for these processes to occur, the two leads must be separated by a distance comparable to the coherence

length[47]. The ability of currents in one lead to induce a voltage in the other lead is captured by the conductance matrix

$$\begin{pmatrix} G_{aa} & G_{ab} \\ G_{ba} & G_{bb} \end{pmatrix} \begin{pmatrix} V_a \\ V_b \end{pmatrix} = \begin{pmatrix} I_a \\ I_b \end{pmatrix}, \tag{3.1}$$

with diagonal terms capturing local transport and off diagonal elements describing cross conductance between the leads. The total conductance is a sum of each of the possible electron trajectories in the device[48].

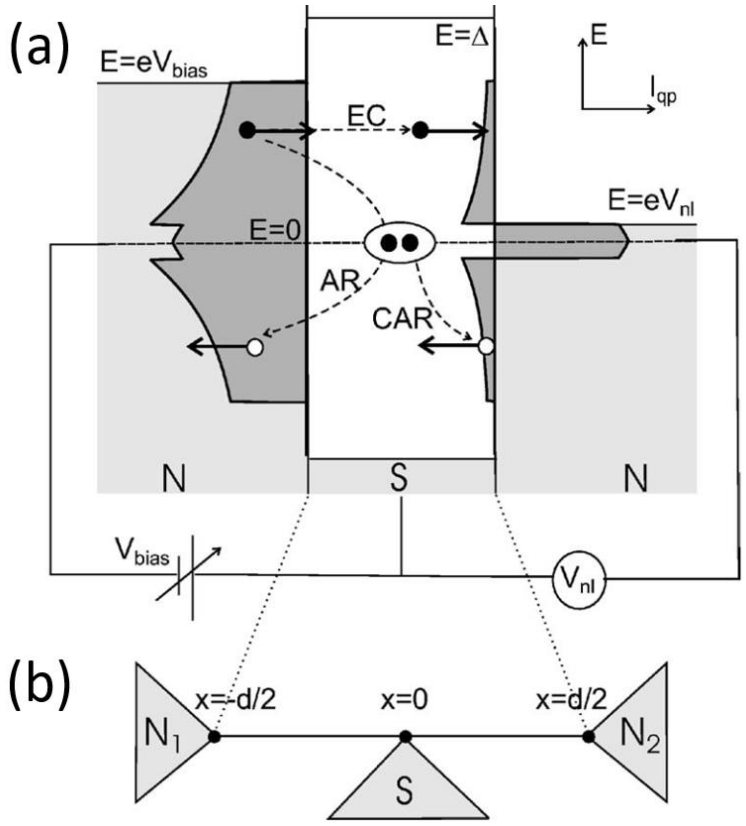

Figure 3.5 Brinkman and Goulubov[47] calculated transport for three terminal normal metal-superconductor-normal metal devices in the quasiclassical limit. They showed that two new outcomes are present for an incident electron. An electron can tunnel across to the second normal lead via elastic co-tunneling (EC). The other new process is to have the incident electron create a Cooper pair with an electron in the other lead which retro reflects a hole into the second normal lead. This process is called crossed Andreev reflection (CAR). Both new processes decay with normal lead separation exponentially on the length scale of the coherence length of the superconductor.

3.1.4 Asymmetrical Signals in Nonlocal Transport

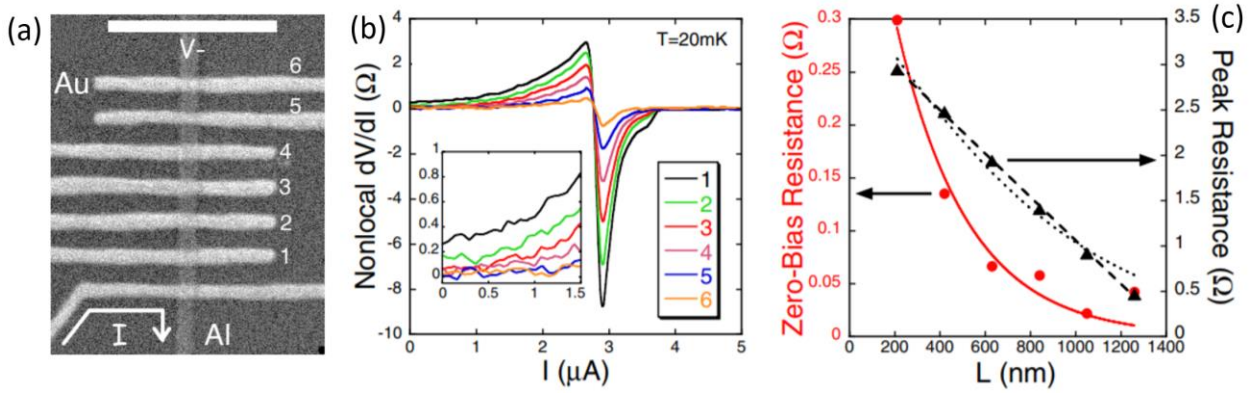

Figure 3.6 Cadden-Zimansky measured[49] the length dependence of the non-local transport in Au-Al devices (a). The scale bar in (a) is 1 μm showing the short length scale of the devices. The non-local signal measured on each of the leads as a function of bias current (b) shows that there is a zero bias nonlocal signal. The nonlocal resistance increases before a sharp drop and a return to zero above the Al gap. The authors analyzed both the zero-bias resistance and the peak resistance (c), showing that the decay length of the peak resistance is much longer than the decay length of the zero bias nonlocal resistance.

In addition to the nonlocal and the charge imbalance signals observed in three terminal devices, asymmetrical signals in the nonlocal transport have been observed in devices with spin active interfaces[50], [51]. Wolf *et al.* measure the local and nonlocal transport in SFS devices and observe an asymmetrical nonlocal signal at the gap edge[50]. The spin dependent transport can be contrasted with the charge imbalance behavior by applying a magnetic field. After separating out the two effects, they report seeing long distance spin imbalance signals in their aluminum superconducting devices. They present a model that is odd in the polarization of the contact, and in the spin imbalance. The spin active interface is sensitive to the spin imbalance signal and the charge imbalance signal. On the other hand, the normal metal is only sensitive to the charge imbalance, which is used to remove the spin imbalance signal from the spin sensitive data.

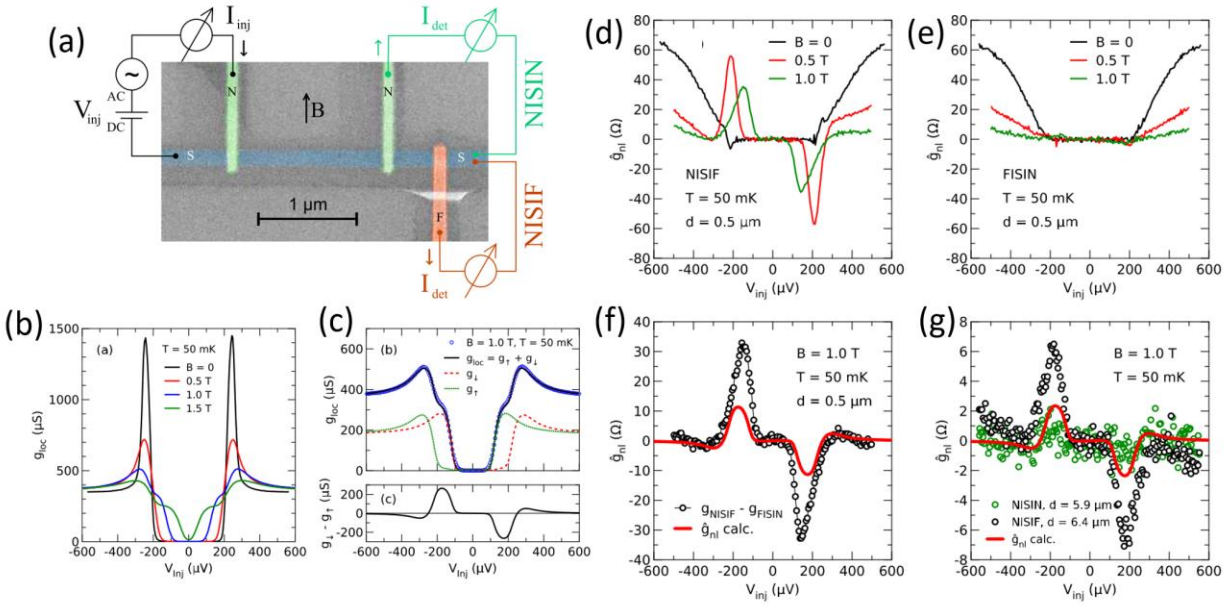

Figure 3.7 M. Wolf *f* studied[50] the charge and spin imbalance in an aluminum wire using a device with a normal metal and a ferromagnetic contact (a). The local resistance shows a clean tunneling gap (b) with field dependent features that are interpreted as splitting of the spin states in energy (c). Using a normal metal as an injector and a ferromagnet as a detector (d) shows the spin physics combined with the charge imbalance physics. With the roles reversed, the detector is not spin sensitive, and only the charge imbalance signatures are present (e). The difference between the two at 1T isolates the spin physics and shows that there is a peak of spin imbalance near the gap edge (f). Using a normal contact 6 um away as an injector, (g) shows the comparison of the NISIN (charge imbalance sensitive) device and the NISIF (spin and charge imbalance sensitive) device at 1T. The charge imbalance signal has completely decayed while the spin signature is still present despite the large separation of the injector and the detector.

An alternative source of the asymmetry in nonlocal transport is due to resistive heating measured and modeled by Kolenda et al[52]. In Cu-Al tunneling junctions as shown in Figure 3.8, the authors used the fits to the local resistance to measure the effective temperature of the device as a function of the bias in the opposite contact. This heating results in an asymmetrical that is the same order of magnitude as the nonlocal signal in their measurements. When the bias currents in the two leads are opposite signs, the resulting heating signal resembles the Cooper pair splitting mechanism, although its origin is distinctly different. When interpreting asymmetrical nonlocal signals from spin polarized currents, it is important to keep possible alternative sources of asymmetry in mind.

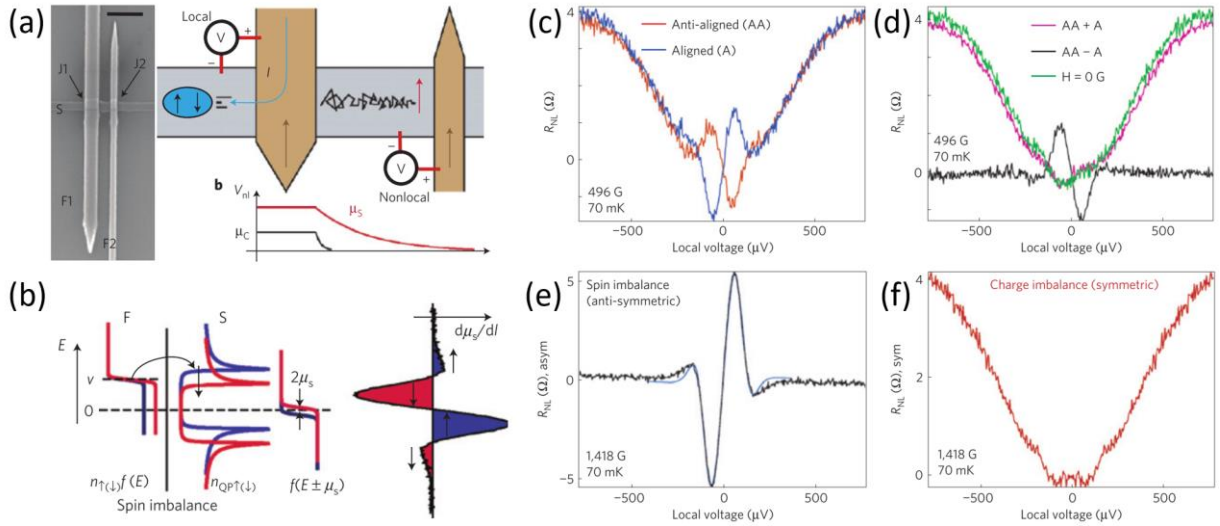

Figure 3.8 In 2013 C. H. L. Quay et al. measured[51] the charge relaxation and the spin relaxation in mesoscopic superconducting wires utilizing the Zeeman effect. Using a device geometry (a) with one large ferromagnetic lead and one narrow ferromagnetic lead, they studied the conductance with the contacts polarized parallel to each other, and anti-parallel. The combined spin and charge effects are shown in (c) for the two polarization cases. By combining the two contact polarizations, the charge imbalance and spin imbalance signals can be isolated and compared to the zero-field case (d). The charge imbalance signal and the spin imbalance signal at 140 mT are shown in (e) and (f) respectively.

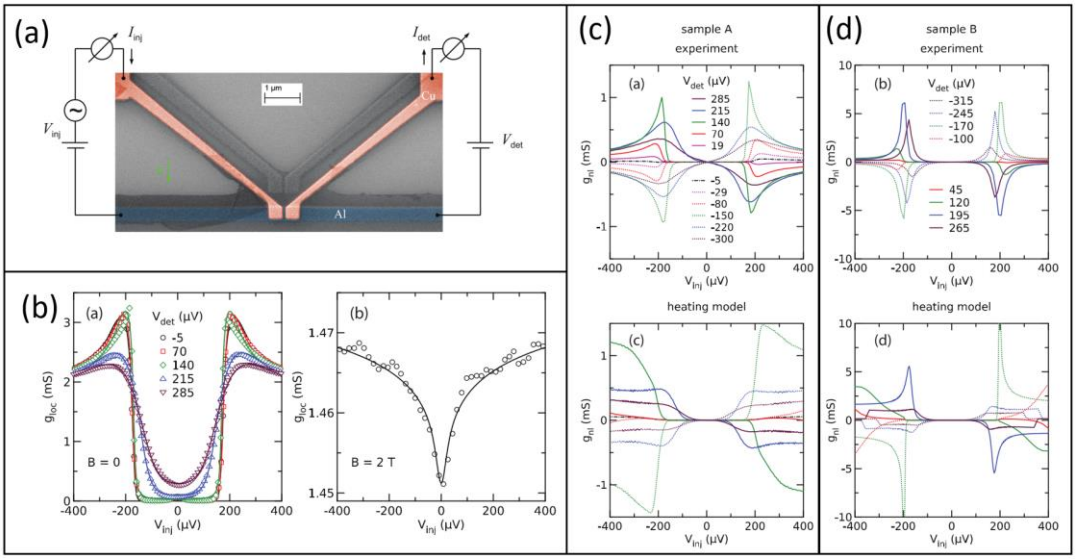

Figure 3.9 S. Kolenda *et al.* measured[52] superconductor-normal metal devices under dual bias conditions showing that heating can cause similar features to the spin dependent features of other spin and charge imbalance focused studies. With a clear superconducting gap (b), the detector bias causes the gap to round out, effectively increasing the temperature. Samples A (c) and sample B (d) shows features near the gap edge that are asymmetric with bias current in the device. Simulations of the heating are included by the authors to show how the heating model would behave for different sample parameters.

Local and nonlocal transport will be used in this thesis to explore the spin properties of the proximity induced superconductivity at Nb-Bi_2Se_3 interfaces. The surface states in Bi_2Se_3 are spin momentum locked, causing the bias currents in the TI contacts to also serve as current dependent spin injectors. By measuring the transport in the other 2 leads of the three terminal devices, the spin dependent transport at the SC-TI interface should influence the resulting current flow. Understanding how the induced currents differ from the conventional case is a key point to understand and determine properties of the unconventional superconductivity engineered in this system.

3.2 Josephson Interferometry

Harnessing the power of quantum interference to explore the pairing symmetry of unconventional SC is at the heart of the powerful technique of Josephson interferometry. After a short introduction to Josephson physics, I will present on some examples where Josephson interferometry has shed light on the nature of unconventional superconducting order parameters.

A Josephson junction is formed when a region of weak superconductivity connects two bulk superconductors, forming a junction that can carry supper currents up to a maximum critical current[53]. The region of weak SC can be composed of two overlapping proximity regions or a narrow superconducting micro bridge. The wave function of the weak region of SC can be described as a superposition of the spatially decaying wave function from each of the bulk superconductors

$$\psi_{Tot}(x) = |\psi_0|e^{i\phi_1}\, e^{-(x+a)/\xi} + |\psi_0|e^{i\phi_2}\, e^{(x-a)/\xi}. \tag{3.2}$$

where ψ_0 is a spatially uniform amplitude of the wave function, ϕ is an arbitrary quantum mechanical phase for each of the wave functions, and ξ is the characteristic decay length scale of the SC in the barrier region. In 1965, Brian Josephson showed[53] that this results in two

fascinating properties of weak superconducting links. The first is that the weak link carries a supercurrent that depends on a junction specific critical current and the phase difference between the two superconductors as shown in equation 2.

$$I_S\,(\varphi_1 - \varphi_2) = \; I_C \sin(\varphi_1 - \varphi_2) \tag{3.3}$$

where I_C is the maximum junction critical current, I_s is the supercurrent carried across the junction for a given phase drop across the junction, and $\varphi_1 - \varphi_2$ is the difference in quantum mechanical phase between the wave functions in the two superconductors. When the bias current in the junction is higher than the critical current, Josephson showed that the phase difference across the junction winds at a rate that is directly proportional to the voltage across the junction according to

$$\frac{d}{dt}(\varphi_1 - \varphi_2) = \frac{2eV}{\hbar}. \tag{3.4}$$

Here e is the charge on the electron, V is the voltage across the junction, and ħ is the reduced Planck's constant. These are known as the Josephson relations, and have been supported by decades of experimental evidence[13], [54]–[56]. They have also provided insight leading to a broad array of applications of SC[57].

3.2.1 Josephson Physics in the Presence of Magnetic Fields

In the presence of magnetic fields, the Josephson relations hold if the coupling of the charged superfluid to the vector potential is considered[4], [13]. The vector potential advances the phase of the superconducting order parameter along a path traced out between two points. This advancement is accounted for with a transforming to the gauge invariant phase

$$\Phi = \varphi_2 - \varphi_1 - \frac{2\pi}{\Phi_0}\int A \cdot ds \tag{3.5}$$

with Φ_0 being the magnetic flux quantum, A being the vector potential, and s being a path traced out between two points, 1 and 2. This translates into a phase gradient along a junction that is threaded by a perpendicular magnetic field. As the phase difference along the junction winds, the

local supercurrent will vary according to equation 2. In some regions of the junction, the supercurrent will be in the direction that the positive direction while in others the current will be opposite that. As the field increases, the junction critical current will decrease initially until there is exactly one magnetic flux quantum in the junction. At that point the super current induced across the junction from the winding of the phase is equal in the positive and negative directions. After this, the junction critical current will increase with field to a second maximum. The functional form of the modulation of the critical current is of the form[4]

$$I_C(\Phi) = I_C \frac{\sin(\pi\Phi/\Phi_0)}{\pi\Phi/\Phi_0} \tag{3.6}$$

with I_C being a junction specific maximum critical current, Φ_0 is the magnetic flux quantum, and Φ is the total flux applied to the junction. The similarity of this phenomena to the optical interference from apertures has led the community to refer to the it as a Fraunhofer pattern. For more complicated geometries and more complicated functional forms, the critical current is often referred to as the diffraction pattern of the junction.

3.2.2 Superconducting Quantum Interference Devices (SQuIDs)

When the SC leads from two Josephson junctions are connected, forming a loop, they become a superconducting quantum interference device, or a SQuID for short. The critical current from one side of the loop to the other in zero field is the sum of the two-individual junction critical currents. The self-field effects of the SQuID are governed by the unitless parameter

$$\beta_L = 2LI_C/\Phi_0 \tag{3.7}$$

where L is the SQuID loop inductance, I_C is the SQuID critical current, Φ_0 is the magnetic flux quantum. The constraint to be non-hysteretic due to self-field effects is to have $\beta_L \leq 1$, which is where a circulating critical current could completely screen out half a flux quantum from the junction[13]. To satisfy this condition, the loop inductance should be small as should the critical

currents of the junctions. For junctions with small but finite self-field effects, the location in field of the maximum of the critical current can be extrapolated to the zero-bias value. This is done by measuring the field dependence of the voltage or critical current at several bias currents or voltages respectively. The excess contribution to the field in the SQuID from the self-field effects are linear in current, so a linear fit to the critical current maximum will point to the filed with the maximum critical current at zero bias. This analysis is important in the Josephson interferometry measurements conducted on unconventional superconductors that will be presented in the next section.

3.2.3 Applied Josephson Interferometry

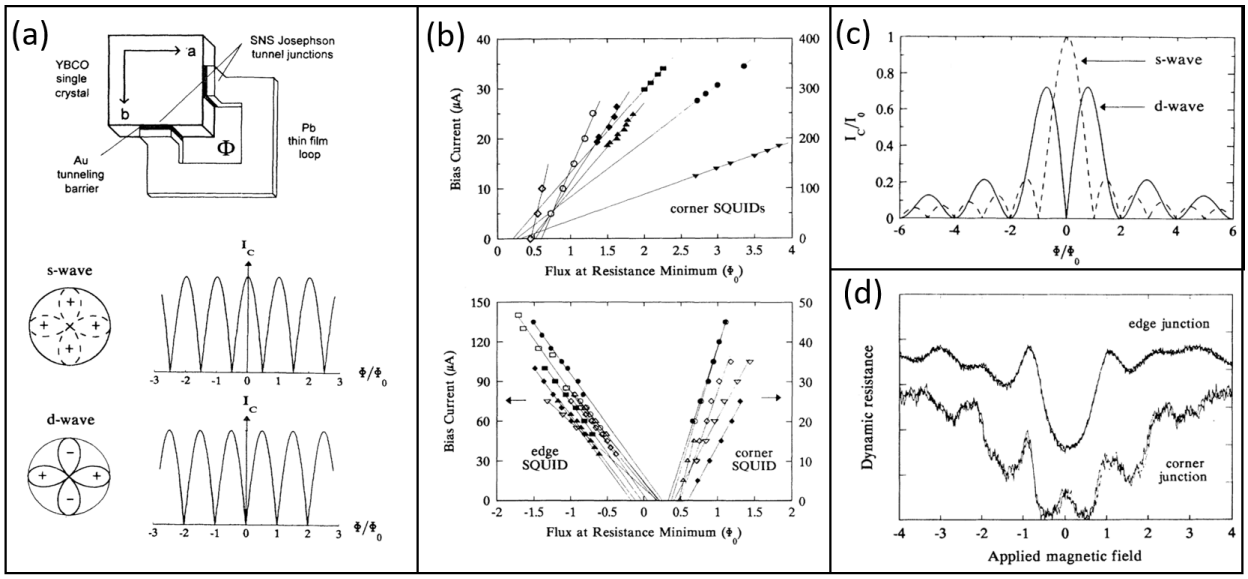

Figure 3.10 Wollman *et al.* identified[58] the pairing symmetry of Josephson junctions on corners and edges of YBCO crystals in 1993. Measurements of corner junctions could differentiate between the anisotropic s-wave model and the d-wave model (a) because of the momentum dependence of the phase of the Cooper pairs. In the SQuID data (b), devices with a junction on perpendicular faces showed a zero bias resistance minimum at 0.5 Φ_0 while edge junctions extrapolated to 0 Φ_0. Single junction simulations (c) show the clear difference between s-wave and d-wave based Josephson junctions that span a corner. The experimental results (d) show that junctions that span a corner exhibit a critical current maximum at zero field, while junctions on a single edge show a resistance minimum.

In exotic SC systems, the unconventional nature of the superconducting order parameter can alter the phase distribution, changing the form of the diffraction pattern. Understanding how the nature of the order parameter changes the diffraction has provided key insight into the pairing symmetry in several unconventional superconducting systems. The first case was in the cuprate superconductors, where corner and edge junctions showed qualitative different behavior when one of the leads was YBCO[59]. For odd pairing systems, Josephson interferometry was used to show that the anisotropic nature of the superconducting order parameter in UPt_3 and evidence for the complex nature of the order parameter[60]. Josephson measurements on S_2RO_4 provided evidence for domains of alternating chirality[18] and later a test of the domain size by making junctions of varying sizes[19]. In all, this method has been applied to a wide variety of SC systems to provide information on the nature of the order parameter.

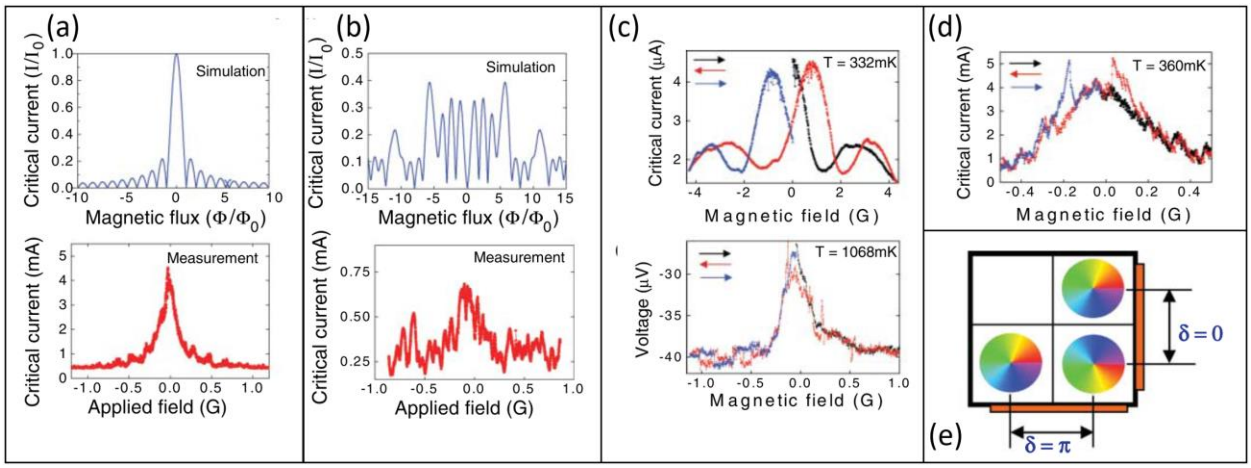

Figure 3.11 Kidwingira *et al.* reported[18] the observation of superconducting order parameter domains in Josephson interferometry measurements on Sr_2RuO_4 crystals. Simulation (a-top, b-top) and experimental data (a-bottom, b-bottom) show that on orthogonal faces with 10 chiral domains of random size can have significantly different diffraction patterns. At low temperature, significant magnetic field hysteresis is present showing evidence of chirality that depends on the field history of the measurement. The authors observed abrupt changes in critical current (d) and telegraph noise (c-bottom) in the junction critical current when individual domains switch chirality. A model of adjacent chiral domains exhibiting an intrinsic phase shift of π or 0 depending on which face a junction is on.

In 1993, Wollman *et al.* showed that Josephson junctions and SQuIDs that spanned a corner were consistently different than those entirely on an edge[58]. The goal of the work was to discern between anisotropic s-wave pairing and d-wave pairing that had a sign change in the order parameter from lobe to lobe. In the case of s-wave pairing, the diffraction pattern from the SQuIDs and Josephson junctions would behave the same as an edge junction, with a critical current maximum at zero field as shown in Figure 3.9. For the d-wave case, the sign change in the order parameter would add an intrinsic phase shift to the tunneling and result in a minimum in the critical current at zero field. Initial measurements were taken of the magnetic field dependence of the resistance of the junction just above the critical current. They showed that for edge junctions the resistance minimum extrapolated to zero magnetic field on several samples. For corner junctions, the resistance minimum extrapolated to half a flux quantum. Josephson junctions that bridge a corner eliminated the self-field effects present in the SQuIDs, unambiguously showing that the resistance minimum for edges was at zero field while there was a clear resistance peak at zero field for corner junctions. Josephson interferometry was provided strong evidence that the nature of the SC order parameter in cuprates was d-wave in nature rather than s-wave.

This technique was applied to the candidate p-wave superconductor Sr_2RuO_4 with a less straight forward interpretation of the results[18]. As shown in Figure 3.11, junctions fabricated on the side of a crystal of Sr_2RuO_4 did not provide as consistent a diffraction pattern as in the YBCO case. At times the diffraction patterns were Fraunhofer like, with a central maximum at zero field. Other times the junctions showed no clear peak, and the patterns were significantly disordered. In addition to that, a magnetic field sweep at low field yielded hysteresis and abrupt switching of the magnitude of the critical current. The authors argue that the data can be explained by a model of superconducting domains in the junction. Each of the domains is chiral, with the phase winding

around in one direction or the other. As shown in Figure 3.11, this domain structure can result in some regions having zero intrinsic phase shift, while others have a phase shift of π, or anything in between. The model also encompassed voltage fluctuations in the junctions at biases above the critical current in static fields. They were interpreted as the movement of domain walls in the junctions, causing there to be a change in the critical current. This model was corroborated by later work[19] on small Josephson junctions that looked for the characteristic junction size where there was only one domain in each junction. Although this model describes the Josephson interferometry results well, there remains a lack of consensus in the scientific community about the pairing symmetry of the material[61]–[63].

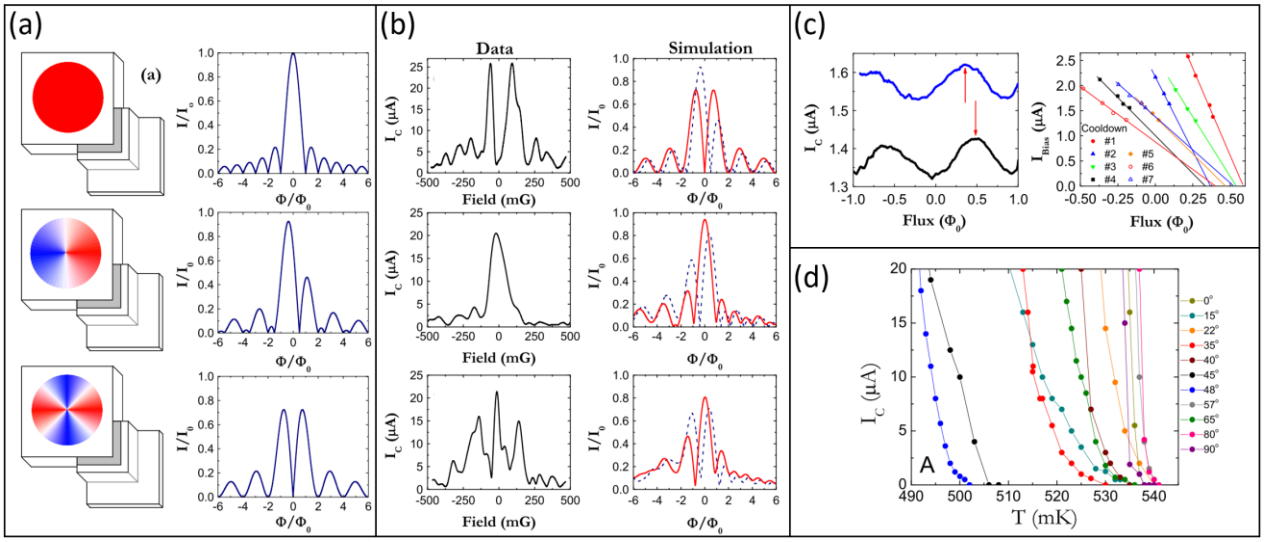

Figure 3.12 In the UPt_3 heavy Fermion system, J. Strand presented[60] Josephson interferometry measurements in his thesis. The 2-D projection of the order parameter into the a-b plane provided three possible order parameter symmetries with widely varying predicted diffraction patterns. The order parameter could be isotropic s-wave, exhibit E_{1g} symmetry or E_{2u} symmetry shown from top to bottom in (a). The resulting order parameters contain phase windings of 0, 2π, or 4π respectively for a complete rotation in momentum space. The Josephson junction measurements yielded 3 distinctive patterns (b) that did not provide definitive evidence for one of the three models. The simulation data shown in (b) include a vortex that is pinned at the vertex. Solid lines assume E_{2u} symmetry while dashed lines represent E_{1g} symmetry. When combined with SQuID measurements(c) and precise measurements of the onset of superconductivity as a function of tunneling direction (d) things became clearer. The authors conclude the order parameter symmetry is E_{2u} from the body of data presented.

The heavy Fermion superconductor UPt3 is another example of a material that Josephson interferometry illuminated the nature of its superconducting pairing[60], [64]. The authors frame the problem as needing to distinguish between two symmetries, E1g and E2u. E1g has a single complete phase winding in the a-b plane resembling p-wave pairing while E2u has two sign windings of the phase resembling d-wave pairing. Again, the results are not a clear cut as in the d-wave case but provide evidence that the pairing has a single sign change in the a-b plane. This is demonstrated by analyzing the three typical diffraction patterns that showed up as shown in Figure 3.12. They are analyzed with each of the two models, and in each case the model with a single sign change from 0 to π provides a better fit than the alternative. A corner Josephson junction was measured with the data presented similarly to Figure 3.10, and the maximum of the critical current extrapolates to 0.5 flux quantum in the junction. This provides evidence that there is an intrinsic angularly dependent contribution to the phase of the order parameter. Additionally, the asymmetry in the junction suggests that the symmetry of the order parameter is complex. To further support their case for the pairing symmetry, more measurements were conducted by the same group where they provide angle dependent critical current versus temperature measurements. When the junctions are at an angle of 45 degrees to the a-axis, there is a minimum in the onset temperature of the critical as shown in Figure 3.12d.

3.2.4 Josephson Junction Simulations

To provide a platform to test the interpretation of the data, I adapted a simulation of Josephson physics to MATLAB using the principles from previous simulations in the group. The simulation begins by dividing a junction up into discrete points along the junction that together form the whole junction. Each discrete point follows the Josephson relation for the local phase difference across the junction. Integrating each local contribution to the critical current gives the

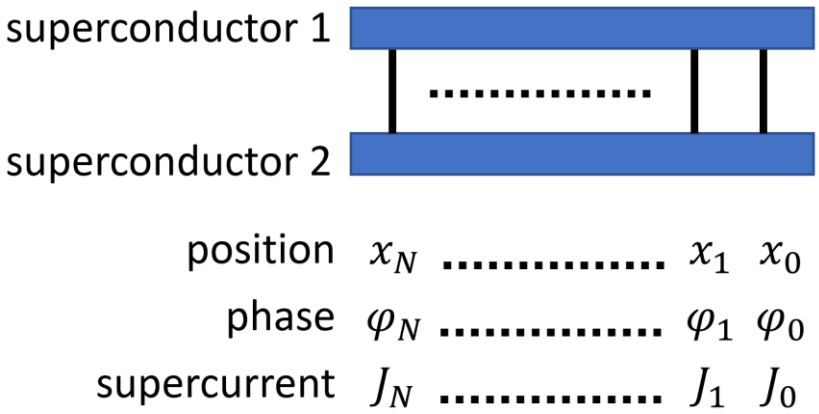

Figure 3.13 The underlying basis of the Josephson junction simulations breaks a junction up into *N* localized junctions along the length of the junction. The local phase difference across each localized junction dictates the amount of supercurrent J_i that is carried. The total critical current is maximized with respect to an arbitrary global phase. Adding a magnetic field induces a phase gradient along the junction, causing the local phase differences to wind along the junction. Other physics can be added including a localized step in phase as a SQuID loop and an intrinsic phase difference for parts of the junction. A more detailed explanation of the simulation is included in Appendix A.

total critical current for given initial conditions which include an arbitrary phase factor, φ_A, which the critical current is maximized with respect to. In the zero-field case, the critical current vs φ_A is a sine function with a maximum when the phase difference at the middle of the junction is $\pi/2$. Maximizing the critical current corresponds to minimizing the Josephson energy in the junction[4], [65]. For the case of short junctions, small SQuID loops, and small critical currents, this captures the important energetics in the problem. Treating the junction as many parallel junctions is a reasonable approximation for a junction in the diffusive limit, where the magnitude of the local critical current from any one place to any other place depends exponentially on the distance between the points. The simulation provides a tool to explore our understanding of the Josephson physics at play in the junctions. More details of the machinery of the simulation are included in Appendix A.

The regime of interest for this work is where the junction and SQuID loops are of comparable sizes. In this regime, there are subtle adjustments of the apparent characteristic area

of the junction. This comes about from the competition between the single junction and SQuID physics. Josephson Junctions show a minimum of the critical current with a single flux quantum in the junction. SQuIDs exhibit a critical current maximum when there is a single flux quantum threading its loop. This causes the first node to be increased to a higher field and can cause an almost entire suppression of the second single junction lobe because the SQuID node at the same field. This unintuitive behavior is shown in Figure 3.14 in the transition region from SQuID to single Junction physics determining most of the modulation in the diffraction pattern.

The pertinent physics for this investigation is distinguishing the effects of critical current asymmetry and critical current noise. These are two effects that can be added to the simulation to see how they influence the diffraction patterns of Josephson devices. Figure 3.14 shows the diffraction patterns from three different geometries in the ideal case without critical current disorder or asymmetry. The plots in Figure 3.15 show the same simulation with critical current asymmetry and with random point noise in the junction. The ideal case captures the physics of each case as expected, with the periods being either 1 flux quantum, or the in between value due to the competition between the single junction and SQuID behavior discussed above. In these cases, the nodes all go to zero because at exactly one flux quantum the positive and negative portions of the critical current cancel out. When there is junction asymmetry introduced, the nodes are lifted because of the excess current on one side when there is one flux quantum in the system. The lifting from the point disorder is much smaller in the plots because there are so many discrete points the junctions are broken up into. With many points, even a large amount of disorder will average out over some length scale. Disorder of this kind lifts all the nodes due to the randomness of the disorder.

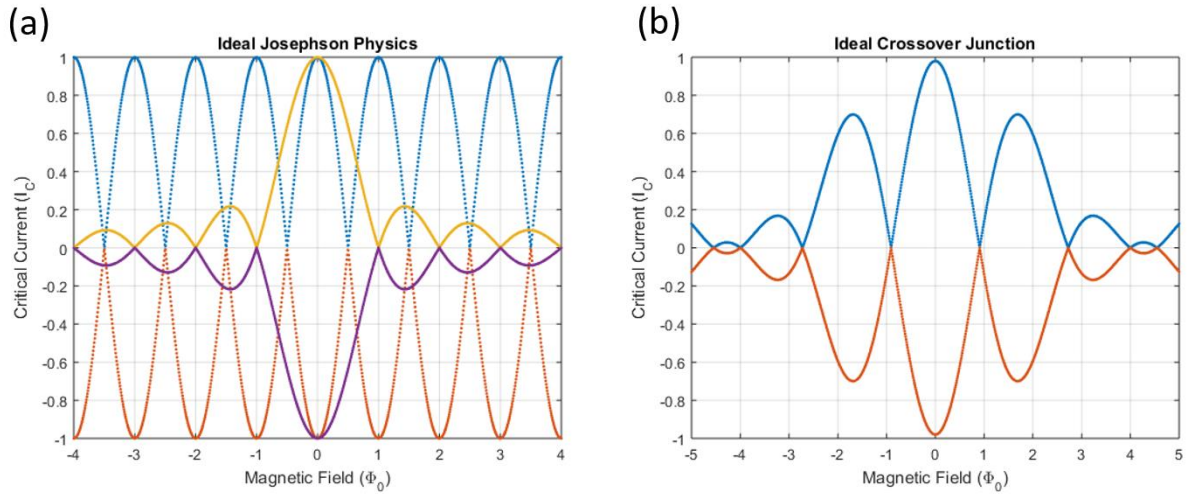

Figure 3.14 The Josephson junction simulation captures the pertinent physics for both the SQuID (a-blue/brown) and single junction (a-yellow/purple) plots shown. This highlights the competition between the single junction node and the SQuID peak with 1 flux quantum in the characteristic area of each device. When both of those areas are comparable sizes in crossover regime SQuIDs, unintuitive squid modulation periods result (b). Without knowledge of the junction area, it is tempting to say that the second node of the diffraction pattern in (b) is missing. However, this is since the junctions have areas of 0.5 and the loop area is 0.6 for this simulation. SQuIDs with similar ratios to these are outlined in Chapter 6. More details on the implementation of the simulation can be found in the appendix.

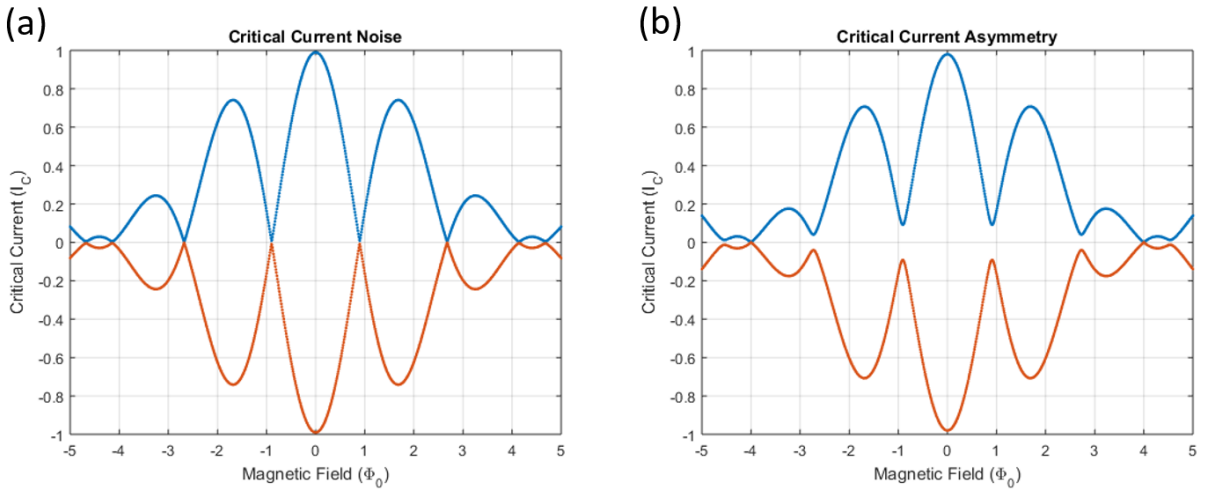

Figure 3.15 The effect of critical current noise (a) and critical current asymmetry (b) show significant differences based on how many domains there are in the junction. The critical current noise in fabricated junctions comes about from lithography variations on the order of 50 nm in length scale for the devices in this work. For a junction with 1 um arms, that translates to 20 domains with random critical current noise in them. The plot in (a) includes 2 junctions with 20 domains each. The random variation in critical current tis 10% of the total critical current. Asymmetry is the equivalent to having 2 domains and is shown in (b). The critical currents are adjusted by 5% each to yield the node lifting seen here.

4. Experimental Methods

4.1 Introduction

In this chapter, I will outline the fundamental techniques needed for this thesis with more detailed explanations of the unique technical challenges that need to be overcome in each area. The technical aspects of the work fall into three distinct categories: fabricating devices, improving thermalization, and addressing measurement circuit challenges. Making and measuring the devices in this thesis required a well-developed understanding of all three areas. This work was done in the Frederick Seitz Materials Research Laboratory (MRL) using a combination of user facility and Van Harlingen group-maintained equipment.

The specific lithographic techniques I used were dictated by the geometric and alignment constraints set by the physics under investigation. I used conventional electron beam lithography to achieve the length scale and alignment of multiple layers that were needed for these devices. Developing the recipe for these samples required me to find a way to decrease charging of the insulating substrates and solve issues related to contacting Bi_2Se_3. In the end, solutions to each of these challenges were iteratively solved over the course of many lithography runs to fabricate devices that could be cooled down and measured.

In parallel to developing fabrication recipes for devices, I also worked on developing a series of cold fingers for measuring devices at low temperatures. The sensitive nature of the proximity effect makes measuring at the lowest temperatures possible necessary in these devices. With the available refrigerators in our group, this means measuring in Triton dilution refrigerators (DR) made by Oxford Instruments. The data I present here was taken in three different DRs, each with their own custom cryogenic cold finger and magnetic field capabilities. Although not unique

to my thesis, I will discuss the considerations for ensuring well thermalized cold fingers as well as superconducting magnets for phase-sensitive measurements presented here.

Once the devices are fabricated and the cold finger is assembled, setting up the measurement circuit often proved to be a formidable test of patience and sanity. I will describe the measurement circuits that were used for measuring the two different types of devices presented here. After describing their design, I will discuss grounding procedures I used to reduce noise in the circuit and the initialization procedure used before each measurement.

4.2 Device Fabrication

Fabricating the devices in this thesis required the ability to align up to 5 layers containing features smaller than 1um within 50 nm of each other. A typical run of lithography steps is outlined in table 3.1. To accomplish this, I utilized the Raith electron beam (e-beam) lithography instrument at the MRL along with the suite of thin film deposition instruments located at the MRL. For e-beam lithography, I used 2 layers of PMMA 950 A5 resist for patterning the device leads along with a layer of AquaSAVE which I will discuss in more detail below. To minimize the size of the devices, I used the largest allowable energies in the system, mostly 30 kV, and performed dose tests every few months. For material deposition, the workhorse system I used was the Van Harlingen group maintained sputtering system known as the Tri-Layer system. This system provided a steady stream of conformal Au and Nb coatings deposited with an in-situ dry etch that enabled clean electrical contact between layers. The Au deposits at 3 nm/s with 150 W (450 V, 0.3 A) in a 3 mTorr argon atmosphere at 150 W (450V, 0.3A). The MRL Micro Fab facilities E-beam 4 evaporator was used for Ti/Au layers that did not need in situ milling or conformal coating. Having a Ti sticking layer under the Au for bonding pads ensured more consistent electrical contact with the wedge bonder.

Step #	Fabrication step	E-beam Step	Process Step	Process System	Film Thickness
1	Alignment Marks	30 kV	Evap. Ti/Au	Ebeam 4	5 nm/50 nm
2	Small Trenches Large Trenches	30 kV 10 kV	Ion Milling	Tri-layer System	2 x 40sec
3	Normal Metal Pads Small Au Leads	30 kV 10 kV	Evap. Ti/Au	Ebeam 4	5 nm/50 nm
4	Normal Metal Connecting Leads	30 kV	Ion Mill/ Sputtered Au	Tri-layer System	3 sec/ 60 nm
5	Superconducting Leads	30 kV	Ion Mill/ Sputtered Nb	Tri-layer System	3 sec/ 100 nm

Table 4.1 Table of normal processing steps that were used to fabricate order parameter symmetry devices. The fine features of each step needed to be aligned to within tens of nanometers of each other. There also needed to be clean interfaces between the Bi_2Se_3film, the normal metal leads, and the superconducting leads to have electrical contact at low temperatures.

4.2.1 E-beam Lithography on Insulating Substrates

One unique aspect of the lithography techniques in this project was that I performed e-beam lithography on the insulating sapphire substrates that the MBE films were grown on. The difficulty with doing e-beam lithography on insulating substrates is that the substrate charges up from the incident electrons. This charging creates fields that interact with the beam and make alignment and tuning impossible. To solve this issue, I used a layer of spun on conducting polymer called "Sulfonated PolyAniline Varnish for E-beam lithography", or AquaSAVE for short, and is shown in Figure 4.1**Error! Reference source not found.**a. Using this extra resist layer reduces the effect of charging when using both high and low currents on the chip to a point that features of 20 nm can regularly be resolved and beam positions do not drift with increased exposure time. Application of AquaSAVE is as simple as another spin coating layer. After the e-beam exposure, the AquaSAVE can easily be washed away with a 10 second deionized water rinse that precedes normal development of the PMMA. The conducting polymer is made to order by Mitsubishi Chemical Corporation and as a result is expensive (~$6000 to $8000 per liter) with a considerable lead time (~3 months). With proper care and use, very little AquaSAVE is needed for each

lithography step. For reference, the last bottle of AquaSAVE in the Raith prep room was shared by several research groups and lasted between 6 and 8 years. In addition to the high price, contact with the substance is not healthy for humans, and should exclusively be used in the flow benches with the spinner in it. All trash contaminated with it should be disposed of in the vented trash container below the spinner flow bench.

Although expensive, using AquaSAVE saves an enormous amount of time and energy compared to depositing a thin layer of metal on top of the resist structure. Without AquaSAVE, a thin 2 nm to 5 nm layer of a conducting metal (Al for instance) on top of the final resist layer is enough to eliminate charging. The largest barrier to entry for depositing a thin conducting layer on the resist is the time and scheduling coordination needed to reserve a deposition instrument in the MRL. For aluminum, this would require finding time in the e-beam evaporator schedule that coincides with when the Raith session is set up for. Once the pattern has been exposed, a short etch step with 917 developer can be used to remove the Al layer before developing the e-beam resist layers that were patterned. The metal etch can be done by eye as the e-beam resists are not sensitive to photoresist developers. There are other spin-on conducting resists including AR-PC 5090 that I recently became aware of thanks to Carolyn Can and have little experience with. They may be easier to acquire and work with while maintaining similar functionality to AquaSAVE. Using AquaSAVE to reduce the effects of charging in doing e-beam lithography was a key part of making the devices in this thesis.

4.2.2 Contacting the Bi_2Se_3 Film Edge

In developing the lithography recipe, eliminating baked on resist and ensuring contact across trenches were issues that needed to be addressed for reliable device fabrication. To counteract the baking on of PMMA residue, two precautions were taken. The first consideration

was in designing the lithography patterns. A path from the smallest features being milled to large areas of Bi_2Se_3 were left open without trenches cutting them off. Whenever trenches completely enclosed an area on the micron scale, there was residual PMMA that would not lift off, even after considerable soaking in solvents and bursts of sonication. With paths leading to large areas, the resist that did not wash away could be removed with a short 30 sec sonication step in solvent. A review of the literature shows that at room temperature, the thermal conductivity of AlO2 (15 Wm-1K-1)[66] is an order of magnitude higher than that of Bi_2Se_3 (2 Wm-1K-1)[67], which in turn is an order of magnitude larger than that of PMMA (0.2 Wm-1K-1)[68]. This clearly shows that heat transfer to large unexposed areas on the chip cannot be the explanation. None the less, the empirical evidence points to a connection between small scale islands in the exposure and residual PMMA in those sample areas. Reducing hardened on resist for small Bi_2Se_3 features was a vital processing step to developing reproducible low resistance contacts.

The other process consideration found to reduce the amount of residual PMMA left after trench milling was minimizing hardening while milling. This was done by breaking up long milling times with shutter closed breaks and reducing the overall amount of time of milling to the minimum needed. The MBE films come from Rutgers and cover the entire substrate, so some trench areas need to be milled to electrically isolate the devices from the rest of the chip and prevent bonding inconsistency after device fabrication is completed. Prior group members had developed a recipe for milling trenches in Bi_2Se_3 films at a rate of 2 nm/sec at 400 volts and 20 mA in the Tri-layer system. In the end, reducing the incremental milling time to 20 seconds with 40 seconds of rest between increments worked well. Then the short milling steps should be repeated until the device area is electrically isolated, or the film has been milled to the substrate to provide a foundation for reliable bonding pad deposition.

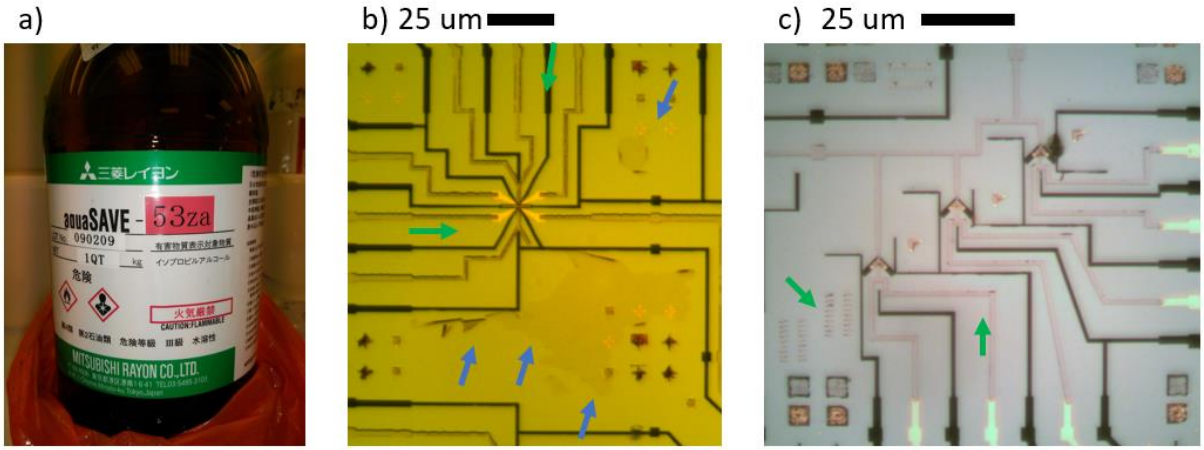

Figure 4.1 The only financially feasible method for acquiring a bottle of AquaSAVE (a) for doing e-beam lithography on insulating substrates was to share it between a handful of groups due to its high price. The above bottle lasted more than 8 years with conservative use. Residual resist residue proved to be a formidable blocking obstacle for this research. In (b) the blue arrows denote regions with residual resist. After several iterations, device geometries eliminated small trench isolated patches. A representative sample is shown in (c) where the green arrows show areas that previously would have resulted in residual resist.

Another reoccurring issue with making contacts to the devices was bridging the gap between the floor of the trenches and the top of the Bi_2Se_3 films. After milling away the trenches, there is a step on the order of 80 nm that needs to be bridged to connect bonding pads on the substrate to leads on the Bi_2Se_3 surface. Several iterations of devices were made with evaporated films that were not thick enough to bridge the gap. Two solutions were considered for solving this problem. The first was to deposit bonding pad material to the point that it would bridge the gap between the trench and the film surface, up to 100 nm of material. Although this is not an unheard-of amount of material to deposit, it would be expensive in the long run. The solution I ultimately settled on was to use sputtered metals as contacts to bridge the gap from the substrate to the film surface. Sputtering is a (relatively) high-pressure process, which could conformally coat the cliff with conducting material. This would solve the problem without needing to deposit large amounts of material in shared systems. Unfortunately, large areas of sputtered Au have large amounts of

intrinsic stress and peel off without a sticking layer. In the end, sputtered Nb was the best solution for connecting the bonding pads on the substrate to the leads on the surface of the film, whereas small sputtered Au leads worked well for contacting the 3 terminal devices.

4.3 Refrigerator Selection and Cold Finger Design

Oxford Instruments dry dilution refrigerators proved to be the best systems to measure data for these experiments because of their low base temperature, ease of use, and availability in our lab. Dilution refrigerators (DR) are refrigerators that use the quantum properties of a mixture of He3 and He4 to cool samples to milli-kelvin temperatures. While in graduate school, I have had the chance to see three DRs installed and help with design and construction of the initial cold fingers and upgrades for each of them. In addition to cold finger design, developing a robust sample holder and wiring scheme that could consistently connect 24 pins from the sample to the measurement electronics with low-temperature filtering proved to be a formidable foe.

4.3.1 Cold Finger Design Considerations

For good thermalization, it is important to ensure that there is a path from the sample to the mixing chamber plate that minimizes thermal resistance through material choice and cold finger design. The material of choice for sample and filter mounting is oxygen free high conductivity (OFHC) copper for its lack of superconducting transition temperature, its lack of magnetic properties, and its high thermal conductivity even after phonon thermal transport has been frozen out at cryogenic temperatures. The cold fingers I designed were built out of 1/8" to ¼" OFHC copper bars with holes machined into them. Whenever feasible, the pieces were made from a single piece of OFHC Cu. For complicated parts, multiple pieces could be machined from Cu and then brazed together with silver solder in the machine shop. In cases where parts needed to be disassembled, through holes with either brass hardware or nonmagnetic stainless steel were the

connections of choice compared to tapped holes in the Cu itself. A thin layer of Apiezon thermal N grease can provide some extra surface area for long-term Cu on Cu through-hole connections. For small parts that do not have much copper below them in the thermal chain, threaded holes can be used to hold the part on. In practice, this was only used for the RC filter boards and for mounting the printed circuit boards the sample is mounted on. Even in this case, the best solution is to have a screw come from the back side through a threaded hole to hold it in place. Then have a nut come down from the top of the sample holder to clamp the sample against the cold finger.

To prevent radiation from the higher temperature shields from shining on the sample, the entire sample space is enclosed in shields that are anchored to the mixing chamber. The design specifics for the shields depend on the magnetic fields that will be applied in each DR. For the DR without a magnet, known as Mr. Freeze, the shielding is made up of an OFHC liner with a separate CRYOPERM 10 shield on the outside to suppress residual fields. For the vector magnet DR, known as Magneto, the Cu shield has a slit down the side with the intention of reducing eddy current heating while ramping the magnet during field scans. After consulting with Oxford DR designers, for the 5T solenoid known as Elsa, the thermal shields are made from brass, which has decent thermal conductivity at cryogenic temperatures. Using brass over OFHC copper has the added benefit of an increased resistivity that reduces eddy current heating while sweeping the magnetic field. Providing a resistance-free thermal path from the sample to the mixing chamber is a key step in designing DR cold fingers for low-temperature measurements.

4.3.2 Magnet Design Considerations

A key part of the phase-sensitive measurements that are presented in this thesis is having a magnet that is suitable for the device geometries of interest. For the single flux quantum sensitive devices measured, a custom machined and wound magnet was made with the suitable

field range and stability needed to measure order parameter symmetry devices in the range from 1um2 to 10 um2. Each cold finger is made up of 4 parts: the shield, the cold finger, the magnet, and the wiring.

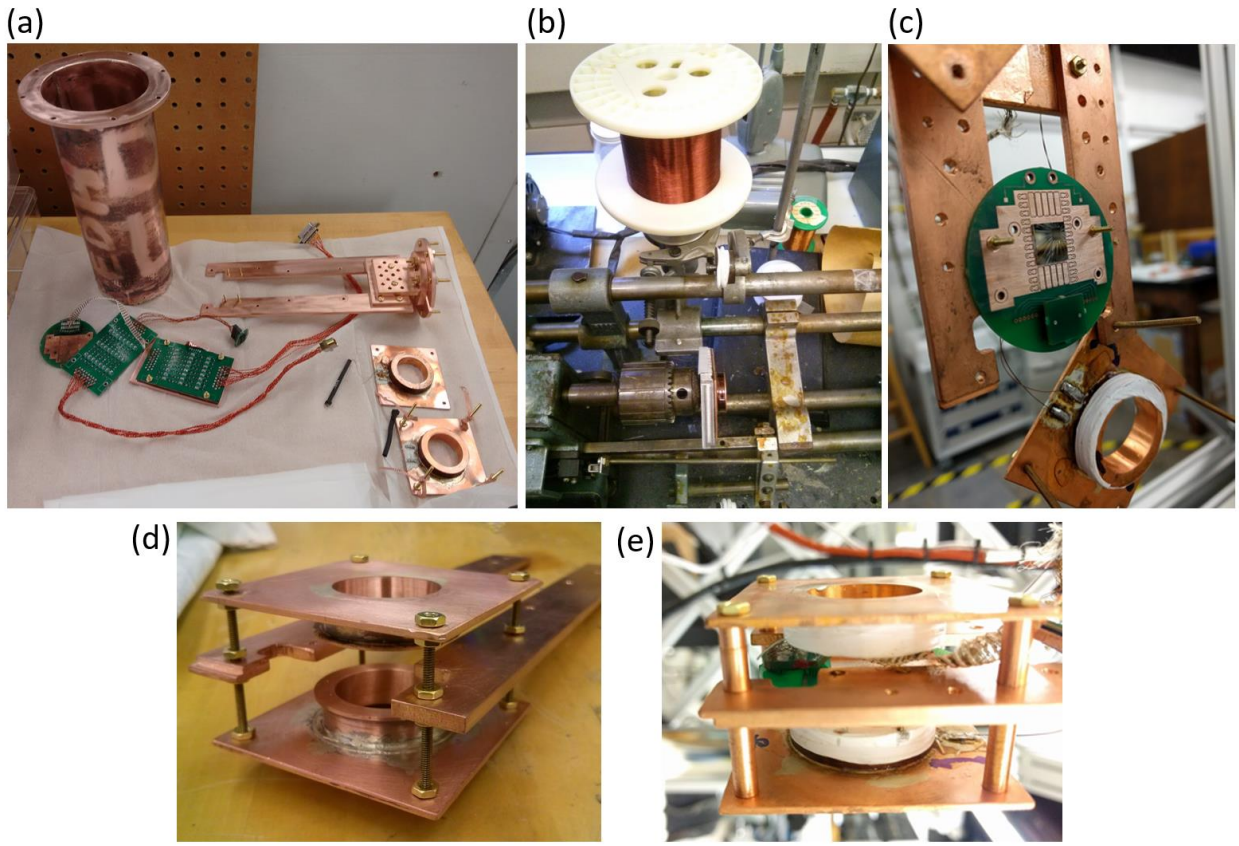

Figure 4.2 Making phase-sensitive measurements requires a specially designed cold finger with good electrical filtering, thermal contact, a low field magnet, and magnetic shielding. The final machined cold finger and shield (a) includes a sample holder, filtering and a Helmholtz coil for applying field. Each half of the magnet was separately machined and then wound on the coil winder (b) to have a 1" coil diameter, 1000 windings per half, and produce 0.1 mT/mA of current. Two-part G1 epoxy was applied while winding the coils to thermally anchor the coils to the support structure and protect them from being broken. Strong thermal contact between the cold finger and the sample was achieved with custom printed circuit boards mounted to the oxygen free high conductivity copper bars (OFHC). The Helmholtz coil is held together with brass threaded rods (d) to align the coils and hold them apart. In the final construction (e), OFHC copper standoffs were machined to provide enhanced cooling and more consistent assembly of the magnet.

Designing and machining the magnet was the most technical part of constructing the cold finger. With a target of 0.1 mT/mA applied to the magnet coils and the number of coils limited by the amount of space there is on the cold finger, the radius needed to be smaller than the diameter

of the 24 pin sample boards the rest of the cold finger was designed around. To accommodate the smaller diameter, a design where the coils hang in front of the sample was adopted. After machining the parts as can be seen in Figure 4.2, NbTi wire was wound around the magnet support structure and epoxied in with G1 epoxy. This provided robust support for the windings with good thermal conductivity while ensuring mechanical stability of the system. To ensure thermal contact with the cold finger to the magnet support plates, OFHC Cu tubes were machined as standoffs that the magnet support plates were clamped against. This design enables consistent alignment, separation, and thermal contact with each assembly. The hardware used to hold the cold finger together is made entirely from nonmagnetic materials that do not distort the applied fields. With these design considerations, I was able to measure the phase-sensitive behavior of samples with dimensions in the vicinity of 1 um^2.

With phase-sensitive measurements, magnetic shielding is another important aspect of cold finger design. Any residual field in the sample could become trapped flux, which would confound any conclusions that you are trying to make. To eliminate this as a possibility, CRYOPERM 10 shields were designed and ordered that fit around the outside of the Cu thermal shields. In designing the cold finger, one of the limiting factors on the diameter of the Cu shields was the ability of the CRYOPERM shield to suppress earth's magnetic fields in the devices. Our rule of thumb was to have the depth of the can be more than 2 diameters in length. With one layer of CRYOPERM, the zero-field offset was below the field zero resolution of the devices we used. For devices that need lower levels of residual field due to their large area, a second layer of CRYOPERM can be combined with a lead bag that suppresses the field even further. Using these magnetic shields, the possibility of trapped flux from earth's magnetic field can be reasonably eliminated.

4.4 Measurement Setup Configuration

Two similar measurement circuits with the same fundamental pieces are used for measuring the two types of devices that are presented. The foundation of the measurement circuit is the low noise current source that is made from an electrically isolated voltage sum box and a large bias resistor. The sum boxes bring in two voltage signals, send them through AD622 instrumentation amplifiers before summing them in an A+B/100 ratio with an OP177 operational amplifier. The resulting voltage is applied to a resistor that is two orders of magnitude larger in resistance than any other resistance in the circuit to convert it to the device bias current. The signal that is fed into B is from an SR 830 lock-in amplifier running at either 83 Hz or 87 Hz. Integrated into the cold finger wiring is an RC filter with cold resistors to thermalize the leads and filter out any high-frequency signals that would wash out the low-frequency voltages we are interested in. Between the device and ground is a 1 kOhm current sensing resistor, with an AD 1211 voltage preamp to amplify the signal for the computer-aided data acquisition system. The voltage across the device is also amplified with an AD 1211 and fed into the computer. The preamplifiers are DC coupled with between 102 and 104 gain and a 300 Hz roll off low pass filter. Additionally, the outputs of the preamplifiers are sent to the lock-in inputs to measure the differential signals. The AC biases used are generally between 5 nA and 500 nA depending on the scan range and device resistances being measured.

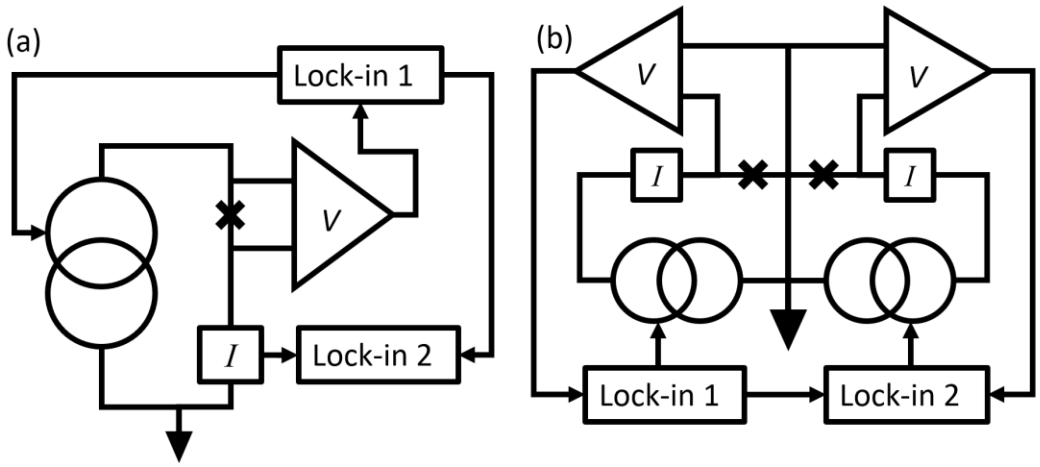

Figure 4.3 The transport measurements in this thesis were taken with one of two wiring setups to measure the *DC* electrical response along with the *AC* response referred to as the differential resistance. The first circuit (a) is a 4 terminal measurement where V_{DC}, I_{DC}, V_{AC}, *and* I_{AC} are all explicitly measured. In this setup, the current measurement is intentionally placed between the device and ground to make shorts to ground obvious. It is used to characterize each device that is cooled down before connecting the 6-terminal measurement (b) used for nonlocal transport measurements. The sign convention in this setup is that all voltages are measured positive relative to the grounded middle contact. The current sources are composed of a computer controlled and electrically isolated home-built voltage follower and a large resistor, generally 100kohms or 1Mohm, that converts the voltage to a current. The amp meters denoted by *"I"* are made up of a small resistor and a variable gain preamplifier that is identical to the ones used for measuring the voltage across the device. The outputs of each preamp are sent to a respective lock-in amplifier to measure the *AC* component of each signal at a low frequency, generally 73 Hz.

This basic unit is used for measuring in the 4-point configuration in phase-sensitive measurements and diagnostics of 3 terminal devices. In this configuration, the DC voltage and current are measured as well as the AC components of each. This enables calculation of the differential resistance without making assumptions about the dependence, or lack thereof, that the AC current bias has on the DC current bias. For most of the devices in this thesis, the *AC* current bias had a negligible dependence on the DC current bias in the circuit. In the 6-point measurement, two copies of the base circuit are combined as shown in Figure 4.3, with a common ground. This addition complicates the measurement sign convention if not aware of the convention used in the field. This convention is to have all currents going into the superconductor be positive, and all local resistance be positive. This means that a current passing from the left lead into the right lead

will change signs, even though no change of direction would have occurred. In measuring the 3 terminal devices, first one side is biased with an AC current, and both AC voltages were measured. Then the other side is biased while recording the voltages across the same parts of the circuit. This results in measuring the entire resistance matrix of the 3-terminal device. For both measurement circuits, DC bias currents were limited to 30 μA due to the amount of heating by the cold resistors and the cooling power of the DR.

4.4.1 Considerations for Grounding

Low noise electrical measurements are susceptible to grounding problems that will cause low-frequency drift, high-frequency noise, and overall smearing of the measurement if not done thoughtfully. Unfortunately, this is a topic of considerable debate, with each experimenter having their own voodoo that lowers the level of noise in their measurements. In my experience, the most important thing is to make sure that none of the connections to ground have resistance in their path to the common ground in the measurement circuit. I accomplished this by using stranded copper wire to connect each piece of electronics on the measurement circuit ground together. I found that connecting each piece of electronics to the rack was not enough. The ground wire from each piece of electronics should be connected with a screw into the electronics rack so that there is a low resistance copper path between each of them and a common grounding point. Importantly, the electronics rack's chain of grounds should be connected to the refrigerator, which, for systems with a magnet, is connected to a clean ground through the magnet supply. For systems without a magnet, the large electrical mass of the refrigerator provides a stable grounded mass that everything else in the measurement circuit can be referenced to. The second most important aspect of grounding, from my experience, is to isolate any digital instruments from the clean analog only

measurement circuit using instrumentation amplifiers, isolated BNCs, and separate electronics racks that are not electrically connected.

4.4.2 Initialization of Measurement Setup

In our measurements, we are interested in the changes in DC resistance of the devices under investigation. We take several measurements to ensure that what we are reporting is, in fact, the change in resistance of the device. Prior to measurement, the complete measurement setup is initialized using a resistor of a known resistance. This calibration includes zeroing the bias current, preamp gain and offset calibration, and the lock-in amplifier's phase offset. Once the calibrations are completed, the measurement circuit is connected across the device of interest and the calibrations are verified to ensure there are no unexpected shorts to ground in the circuit. This calibration is particularly important in the 6-point measurement as the phase of the sign of the signal in the lead with DC bias only is of interest. Since the devices are mostly resistive in nature, the phase of the lock-in signal is close to zero after substituting the device for the calibration resistor. This extra capacitive phase offset is likely due to the capacitance in the RC filters on the mixing chamber plate. In testing the circuit, a lock-in phase away from zero is often a symptom of a bad connection in wire bonding or device fabrication.

5. Low Temperature Transport Measurements

In this chapter I will present the results of the low temperature, three terminal transport measurements and the Josephson interferometry measurements conducted on Nb-Bi_2Se_3 bilayers. The main drive of this work is to probe the physics at superconductor-topological insulator interfaces in bilayers using low temperature transport and Josephson interferometry, two methods that have made foundational contributions to the fundamental understanding of unconventional superconductivity (SC). The goal is to test to what extent unconventional SC can be engineered by blending material properties with the superconducting proximity effect.

The first measurement that will be presented is from three terminal transport measurements on Bi_2Se_3-Nb-Bi_2Se_3 devices. The goal of this experiment is to investigate the properties of the proximity-induced SC with temperature, field, and bias sweeps of local and nonlocal resistance. Original data from 3 devices will be reported, with the first being a representative device and the other 2 highlighting specific device resistance regimes of interest. A phenomenological model of the system will be introduced based on the experimental data. After that, a comparison to examples from Ch 3 will be discussed to gain a better understanding of possible emergent physics in the bilayer system.

5.1 Three Terminal Device Local Resistance

The three terminal devices were measured to explore the effect of spin injection on the local and non-local resistance in proximitized Bi_2Se_3 in contact with Nb. These devices consist of a Bi_2Se_3 strip with a narrow Nb lead crossing it. Au leads contact the Bi_2Se_3 strip to pass current and measure voltage on the Bi_2Se_3 strip. The Bi_2Se_3 MBE thin films are grown by our collaborators in Prof. Seongshik Oh's group at Rutgers on buffered Al_2O_3 substrates as discussed in section 2.4. Then they are patterned in several e-beam lithography steps to define alignment

marks, electrical isolation trenches, Au contacts, and a thin Nb wire. After fabrication, the devices are wired up, mounted to the mixing chamber of at Triton 200 DR, and cooled to cryogenic temperatures. Temperature and field sweeps were conducted to probe the properties of the proximity-induced SC in the devices.

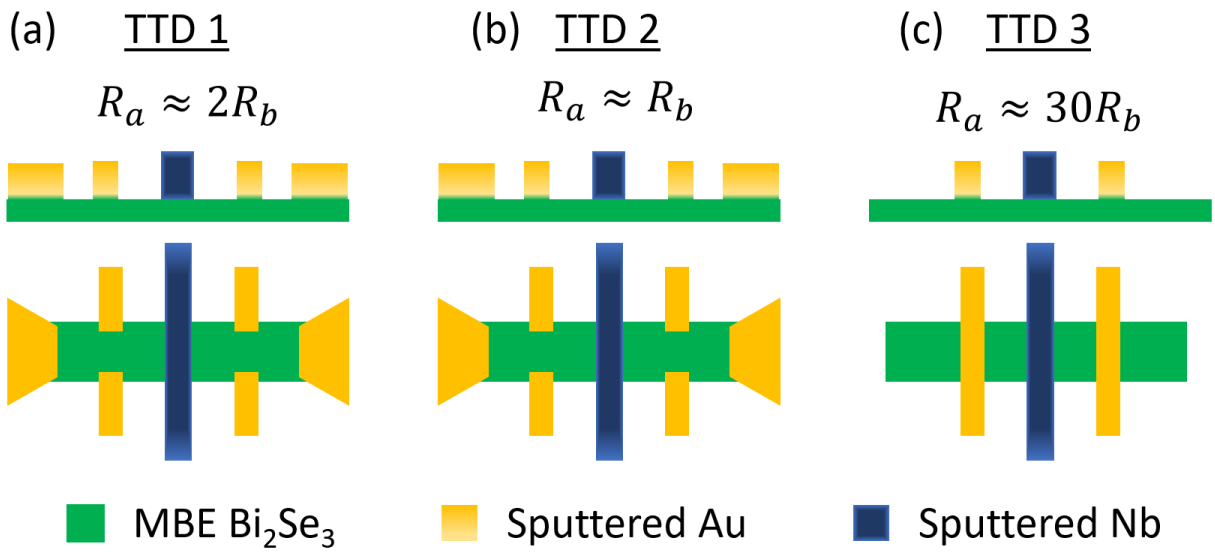

Figure 5.1 The three terminal devices (TTD) measured in this chapter are made up of a topological insulator strip that is contacted on the right and the left side with Au leads. There is a central grounded superconducting lead that crosses the topological insulator strip, splitting the wire into a right and a left half. The geometry of each device is shown, with the corresponding half device resistances. In TTD1 (a) the two halves of the device are different in resistance by a factor of two. TTD2 (b) has symmetrical resistances while TTD3 has a highly asymmetrical resistance. The data from these devices are representative of the data from all the samples measured in this work

Measurements from 3 of the in total 6-three terminal devices measured in the course of this thesis work will be presented, focusing on a representative sample before highlighting unique features from the other three devices. To start with, data from three-terminal device 1 (TTD 1) will serve as a demonstration of the representative of the behavior of these devices. The local resistance provides information on the strength of the induced SC through the temperature and field dependence of features. After presenting the representative data from TTD 1, then other data

will be used to show other cases that were measured including near symmetric device (TTD 2), an asymmetric device (TTD 3).

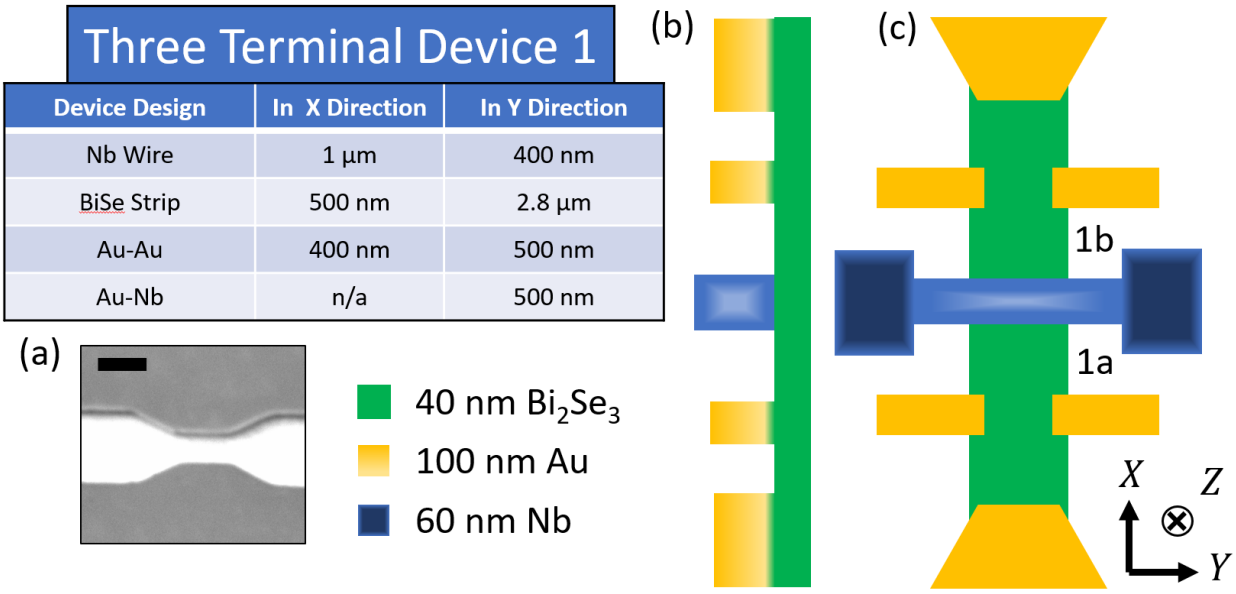

Figure 5.2 Three terminal device 1 (TTD1) is representative of the response of the system when the two sides are different by a factor of 2. The device geometry can be seen in the side cut (b) and top view (c) where the Au and Nb leads contact the strip. The coordinate system for the top view (c) is referenced in the table and holds for the applied magnetic-field directions in later discussion of the device behavior.

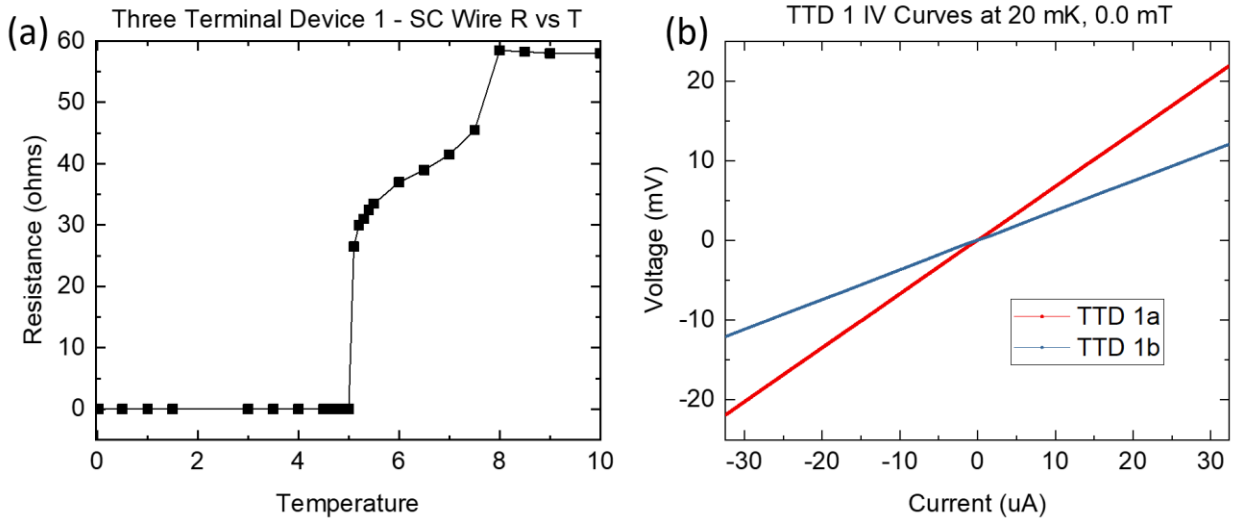

Figure 5.3 The initial characterization of three terminal device 1 (TTD1) is shown here. The Nb wire exhibits a two-stage transition to a superconducting state when cooled (a). The two halves of the device show resistive behavior (b) with a difference of a factor of two in their resistance.

5.1.1 Three Terminal Device 1 Characterization

The device geometry for TTD1 is designed to balance limits set by the physics of interest with fabrication and measurement technical challenges. The specific device geometry can be seen in Figure 5.2. Once the fridge is buttoned up and cooled down, the first thing to check is the SC in the Nb wire and the continuity of each contact. After initial characterization, the local resistance will be used to build a working model of the device.

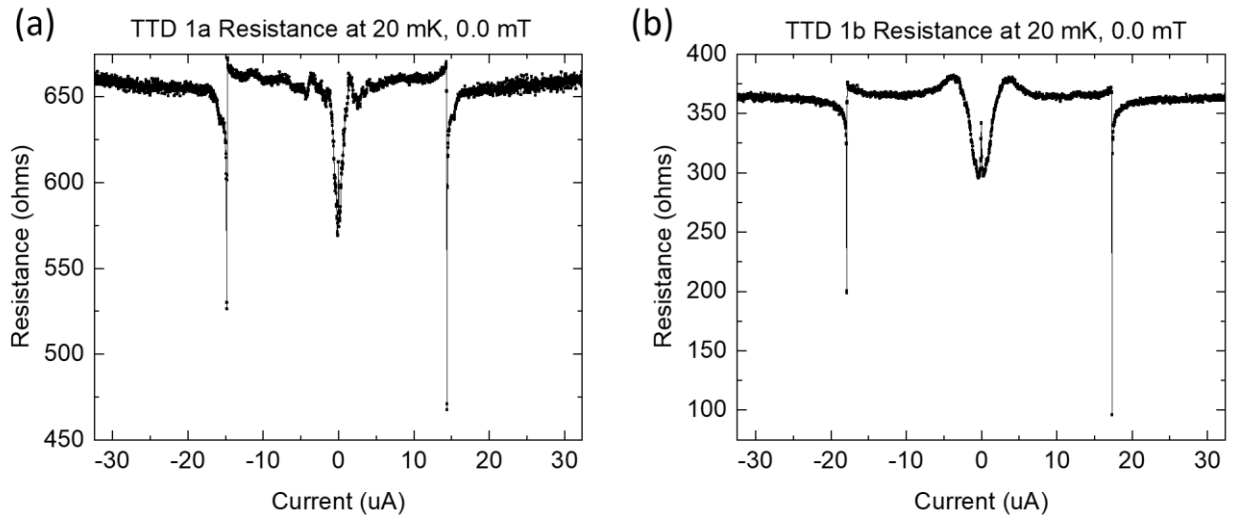

Figure 5.4 Three terminal device 1 (TTD1) differential resistance as a function of *DC* bias for each half of TTD1 as labeled in Figure 5.2. These measurements show that despite the smooth voltage-current plots in Figure 5.3, there is bias dependence to the resistance. The large background resistance compared with the current dependent structure indicates that a majority of the resistance is in the Bi_2Se_3 wire rather than the Nb-Bi_2Se_3 interface. The origin of the features of this plot is the focus of the investigation outlined in this section.

For TTD 1, the Nb wire is made up of a 1 um long x 400 nm wide constriction in an 8.5 um long x 1 um wide wire that is zero resistance at a base temperature of 25 mK. The resistance vs temperature behavior shows a twostep transition as plotted in Figure 5.3. This is likely due to the two regions of the wire having different thicknesses of Nb as verified by AFM for similar narrow sputtered Nb leads. Thin films of niobium have been shown to have suppressed critical temperatures due to niobium surface oxidation and granularity of the sputtered films. The wide lead Tc is between 7.6 Kelvin and 8.0 Kelvin while the suppressed Tc of the constriction is between

5.1 kelvin and 5.2 Kelvin. From the zero-bias resistance vs temperature plot, it is clear that the Nb wire goes through a superconducting transition. This is a good thing to be sure of before trying to study the proximitized SC in the TI strip in contact with it.

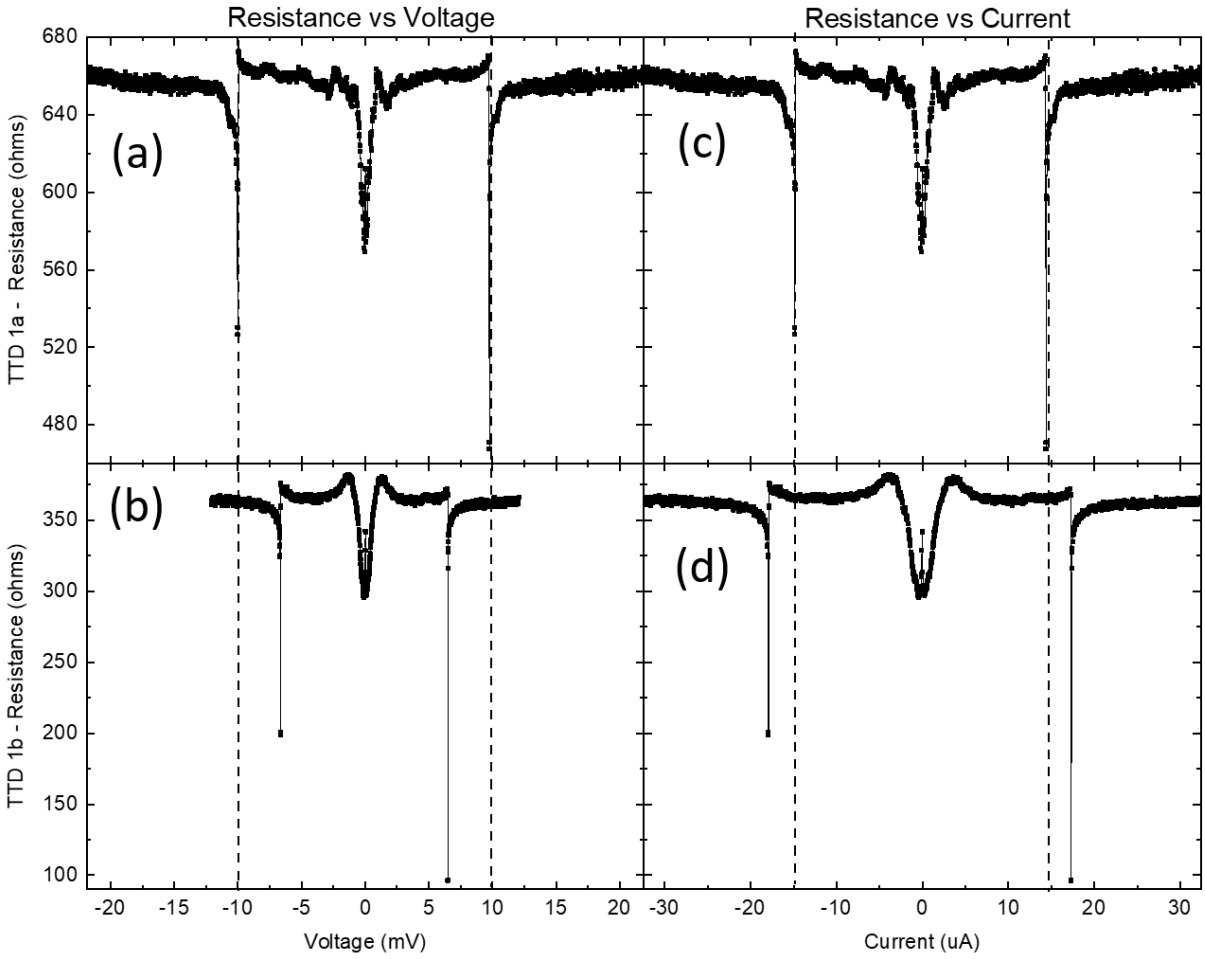

Figure 5.5 Comparing the voltage (a, b) and current (c, d) that the high bias features are located at provides insight into their origin. If the high bias dips were due to a critical current in the Nb wire, then they will be located at the same current in both TTD1a and TTD1b. The high bias dips are also not at the same voltage, showing that they do not arise from a tunnel junction. This hints that they are due to some combination of strong proximitized region with a rescaled energy due to the device resistance that could be causing local heating.

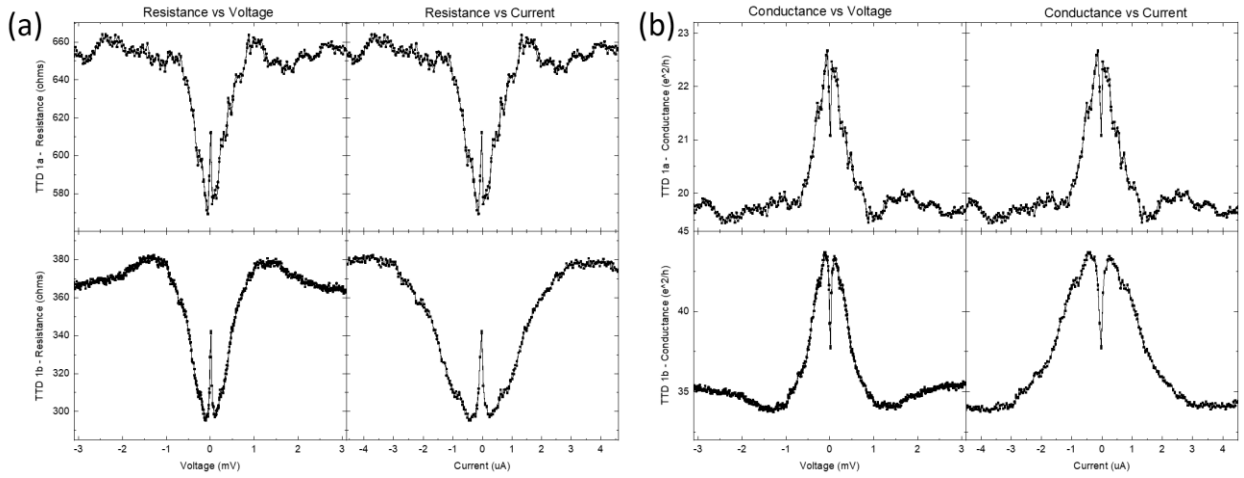

Figure 5.6 The resistance (a) and conductance (b) in the low bias regime of TTD1 as a function of both current and voltage. In this regime, the two halves of the device have similar width features in voltage, not in current. The magnitude of the change in conductance is 10 conductance quanta in the low resistance device, and 3 conductance quanta in the high resistance device. Both devices show a zero bias resistance peak centered on zero energy. Both conductance and resistance are plotted here to show how the features in the resistance translate to conductance.

In the plots in Figure 5.4, the resistance is plotted against current as opposed to the conductance vs voltage as is common in the literature. This data is collected in a current biased configuration common to low resistance measurements that lends itself to plotting resistance versus current rather than conductance versus voltage. The large background resistance means that there is a linear conversion from current to voltage that will result in qualitative features plotted versus current being scaled but not altered significantly when converting to voltage. Calculating the conductance from a current biased measurement is trivial for local resistance measurements but becomes less trivial when more complex measurement schemes such as nonlocal transport in three terminal devices. For comparison, all 4 plots are plotted (voltage/current, resistance/conductance) for each contact with high and low bias ranges in Figures 5.5 and 5.6 respectively. Going forward, the resistance will be plotted as the data was taken in a current biased configuration. It is important to remember that in plotting resistance rather than conductance, the

linearity of the IV implies that the qualitative features in the AC measurement will be scaled but not affected significantly other than that.

5.1.2 Three Terminal Device 1 Bias, Temperature and Field Dependence

To rule out possible alternative explanations we need to show the temperature and field dependence of the features in resistance to conclude that they are a result of the SC in the system. Some resistance features are present in both contacts; notably, they both have broad resistance dips near zero bias, a sharp zero-bias resistance peak, and large resistance dips at high bias. TTD 1a has small but clear oscillations with bias while TTD 1b has oscillations that are much subtler in comparison. The striking feature in TTD 1b that is not present in 1a is the prominent resistance peaks at the edge of the small gap. These features are highlighted in Figures 5.7 and 5.8.

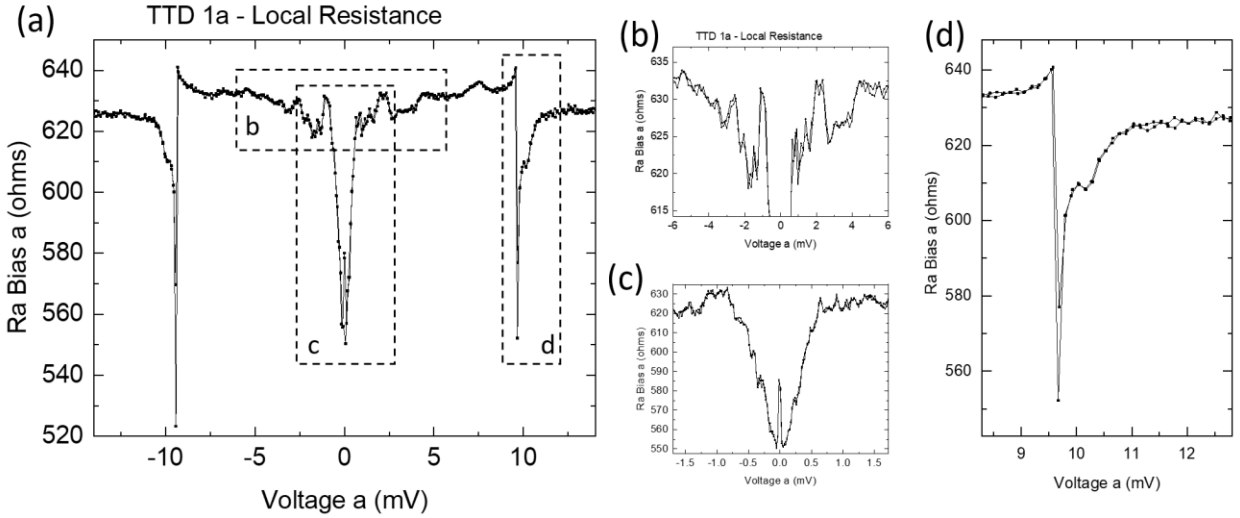

Figure 5.7 Looking at the resistance as a function of voltage (a) in TTD1a shows three characteristic features. There are erratic medium bias resistance fluctuations (b). The low bias region (c) shows a broad resistance dip with a sharp resistance peak at zero bias. At high bias (d) there are small resistance increases followed by sharp resistance dips that have a double peak. All plots are bipolar trace and retrace of the voltage sweep.

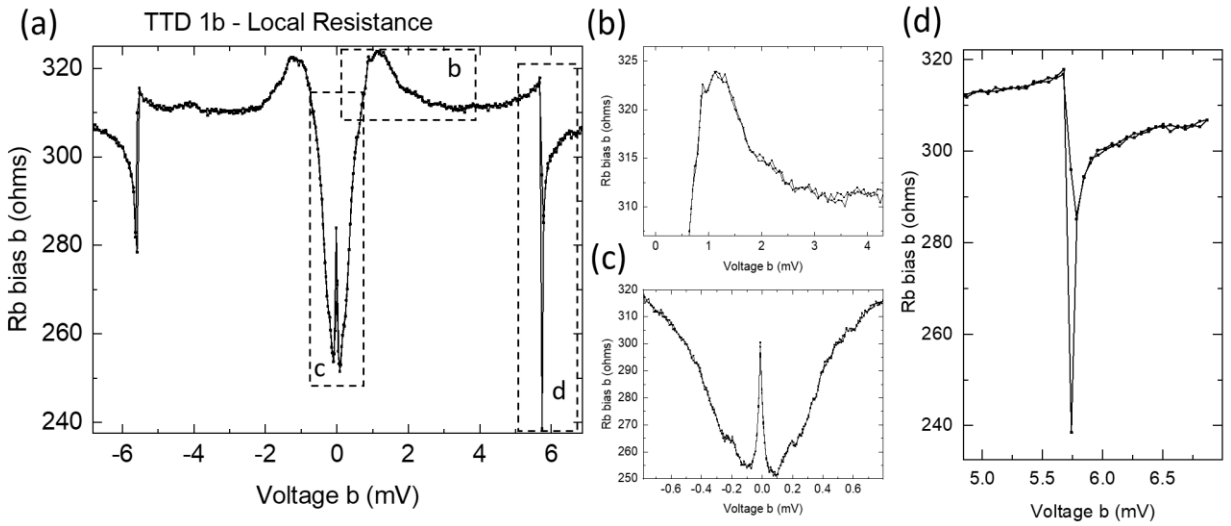

Figure 5.8 A plot of resistance vs voltage for TTD1b (a) shows three characteristic features. There are medium bias resistance peaks with small fluctuations on top of them(b). The low bias region (c) shows a broad resistance dip with a sharp resistance peak at zero bias. At high bias (d) there are small resistance increases followed by sharp resistance dips that change dramatically. All plots are bipolar trace and retrace of the voltage sweep.

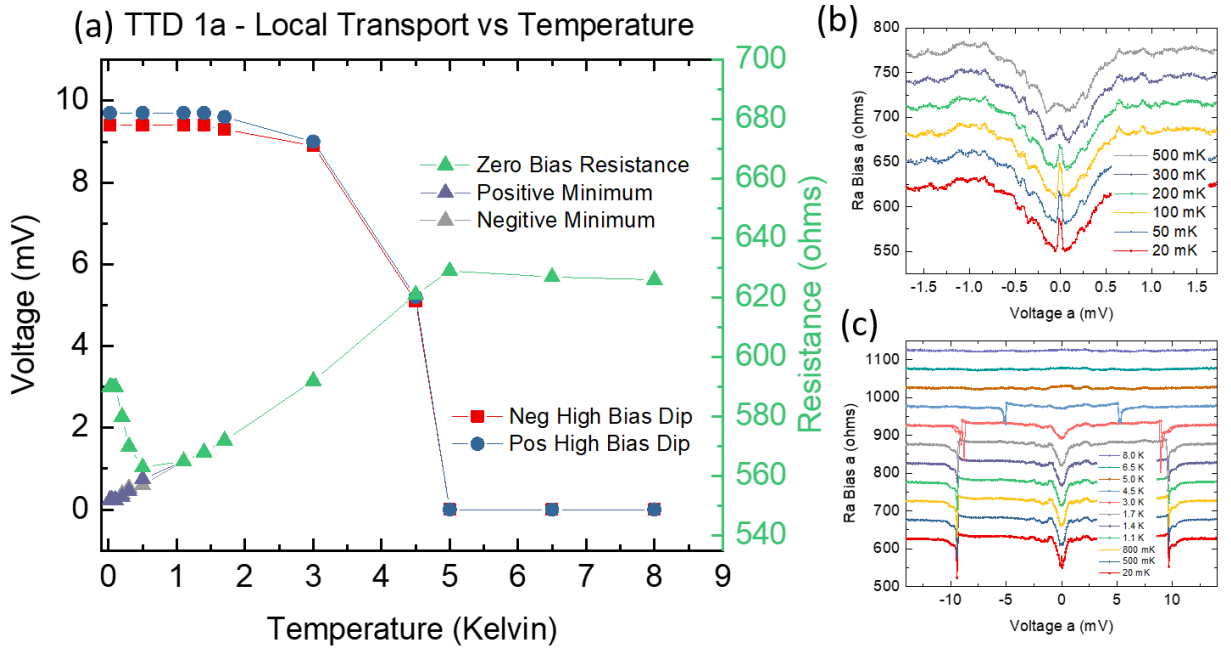

Figure 5.9 Plotting the temperature dependence of the resistance features from TTD 1a shows three regimes of behavior. At the lowest temperature, the zero bias resistance peak decays as temperature is increased (b). The medium temperature regime from 500 mK to 5K shows a steady increase of the zero-bias resistance as the dip fills in (c). The voltage of the high bias resistance dips shows a BCS like decay where there is little change at low temperature before a sharp drop off near the transition temperature. In (b) and (c) the plots are offset for clarity.

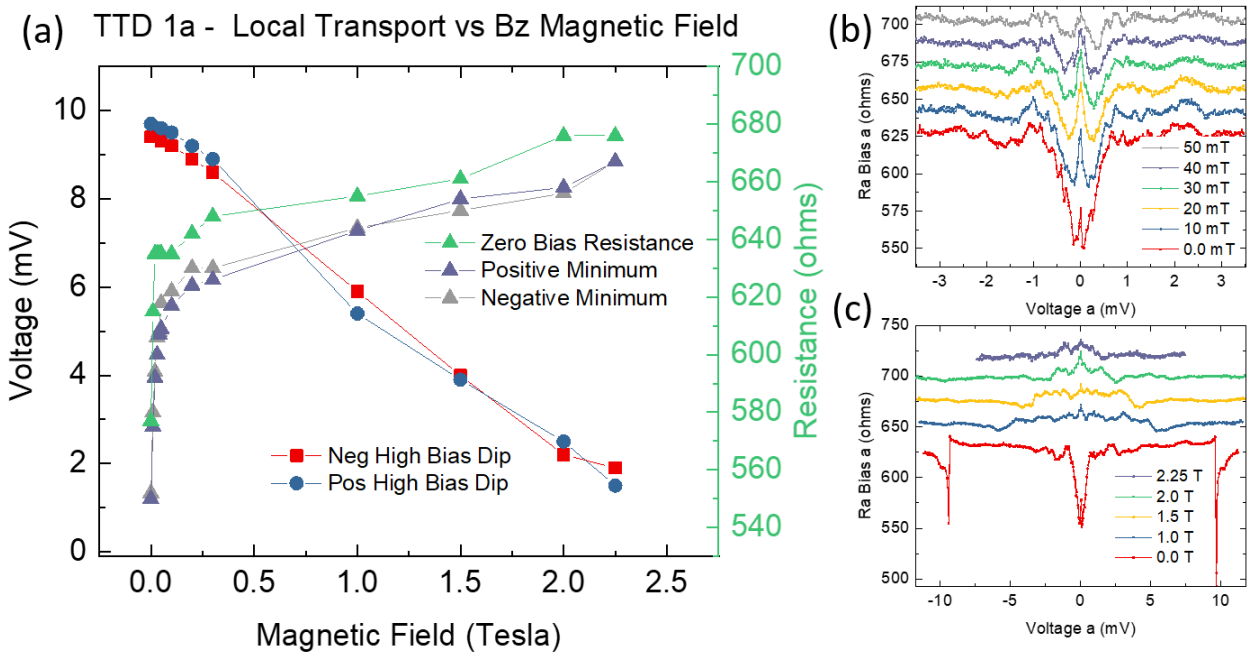

Figure 5.10 Tracking the three-terminal device (TTD) 1a resistance feature behavior with perpendicular magnetic field provides insight into the underlying physics at play. As seen in the summary plot (a), the high bias resistance dips lower in energy as field is increased. The zero-bias resistance rapidly increases initially before slowly increasing to the highest fields measured. The detailed plots of the low bias regime (b) show that the broad resistance dip fills in with little change in the zero bias resistance peak. The high bias features shown over a wide field range (c) show a broadening of the dips as they linearly move towards zero energy with increased magnetic field. In (b) and (c) the plots are offset for clarity.

The key to understanding the physics behind the structure in the bias dependent resistance is finding how the features track in energy with field and temperature. First the temperature and field dependence of TTD 1a will be presented before moving on to TTD 1b and comparing the two to build a working model of the nature of the structure. As shown in Figure 5.9, the zero-bias resistance in TTD 1a has an abrupt drop to a minimum resistance before uniformly rising to the normal state resistance of the device at 5.2 Kelvin. The voltage of the large resistance dip slowly declines at low temperature before abruptly dropping with there being no evidence of resistance dips above 5 Kelvin. In looking at the low bias resistance vs voltage plots in Figure 5.9c the initial drop in resistance is due to the disappearance of the zero-bias resistance peak monotonically to 500 mK. As the temperature continues to rise above 500 mK, the bottom of the broad zero bias

resistance dip slowly fills in with temperature without losing width. When looking at the temperature dependence of the large resistance dips at high bias, it is important to note that the height of the peak spreads out, but they are still extremely sharp, even at 4.5 Kelvin when they are just over half the energy of low temperatures. The oscillations in resistance with bias show no shifting in position with temperature, just a smooth decrease in the amplitude over the entire range of temperatures swept.

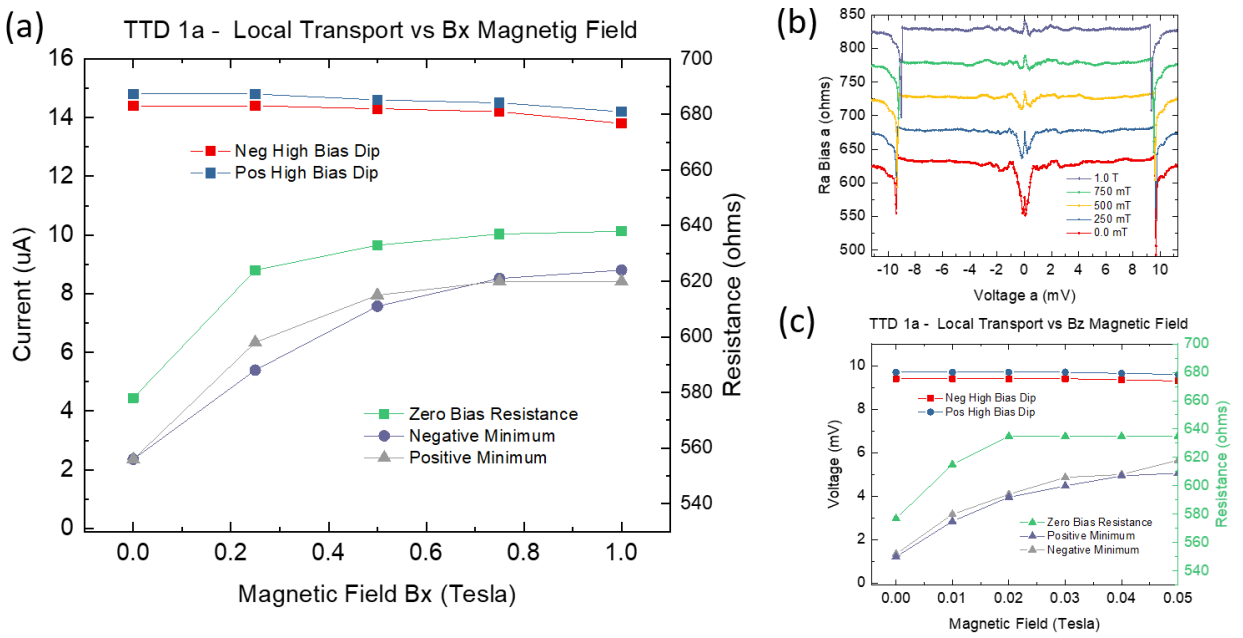

Figure 5.11 The B_x in plane magnetic field dependence of the resistance features (a) shows that there is a weak dependence of the zero-bias resistance on field. The high bias features show very little dependence on the in plane magnetic field. The individual plots of the resistance for different fields shows how the low bias resistance dip fills in with little effect on the zero bias resistance peak. There is also little change in the high bias features up to 1.0 Tesla. For comparison, the low field regime of the B_z field is shown on a range 20 times smaller than the B_x field dependence. In (b) the plots are offset for clarity. The in-plain field is applied parallel to the topological insulator, and perpendicular to the Nb wire in TTD1.

The structure in resistance changes dramatically differently with magnetic field applied perpendicularly (B_z) and in parallel (B_x) to the TI strip. The broad resistance dip at zero bias begins by quickly rising from 0 mT to 50 mT in field where it switches over to a field regime of slower increase where the voltage that the dip starts down at gets narrower with field. The resistance

fluctuations at medium bias show a field dependence, even with fields as low as 10 mT. Although the oscillations move with field, they are clearly still present even at the highest fields measured, 2.25 T. In contrast to the temperature dependence, the high bias resistance features are breaded with field as they move towards 0 mV. Surprisingly the zero-bias resistance peak persists at all fields that were measured.

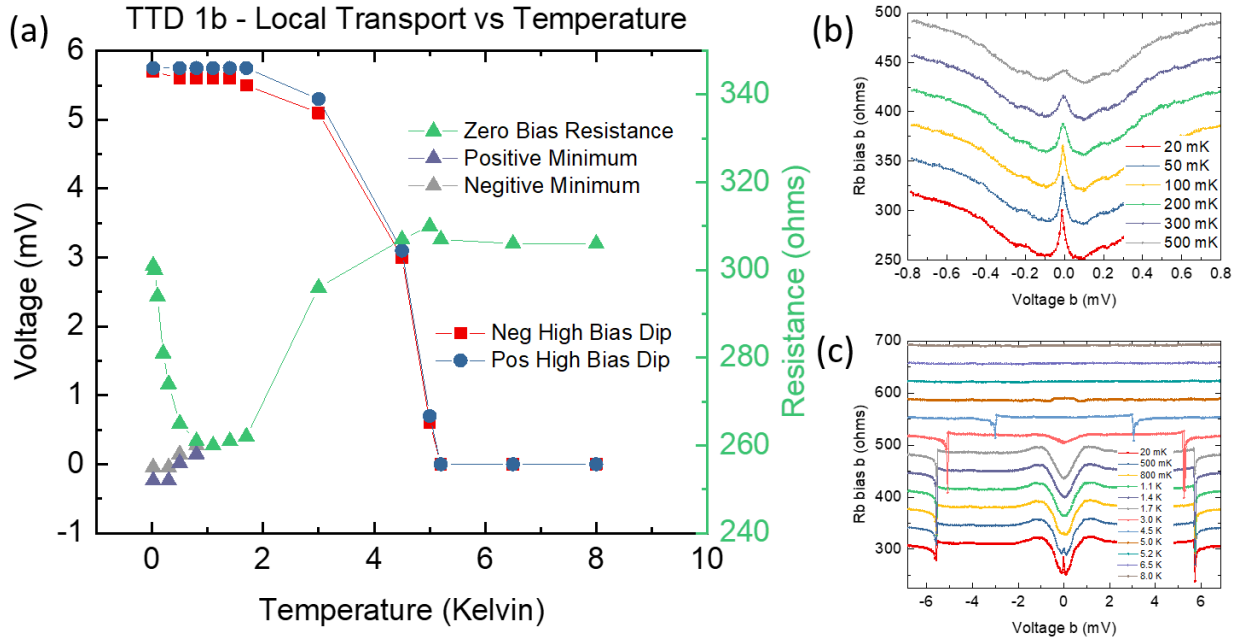

Figure 5.12 The three-terminal device (TTD) 1b temperature dependence of the resistance features (a) show similar behavior to TTD1a. The zero bias resistance peak drops precipitously up to 1 Kelvin (b). Then the resistance monotonically increases to its maximum value at 5 Kelvin as the low bias resistance dip fills in. The high bias resistance dips stay at their low temperature energy up to 3 Kelvin before moving in and broadening with temperature. A similar plot for TTD1a is shown in Figure 5.9. In (b) and (c) the plots are offset for clarity.

Applying an in-plane field provides more insight into the underlying physics of what is causing the bias dependent features in contact TTD 1a. The broad zero bias resistance dip is filled in with very little loss of voltage width as the field is increased from 0 T to 1.0 T parallel to the TI current flow. The minima of resistance follow a similar increase as the zero-bias resistance, indicating that the two effects may not be linked. Like with the B_z, when a magnetic field B_x is applied, the oscillations in resistance fluctuate, although they change much less over a larger

magnetic field range. The large resistance dips at high bias are slightly suppressed in energy, although do not lose the sharpness of their features like in the B_z sweep.

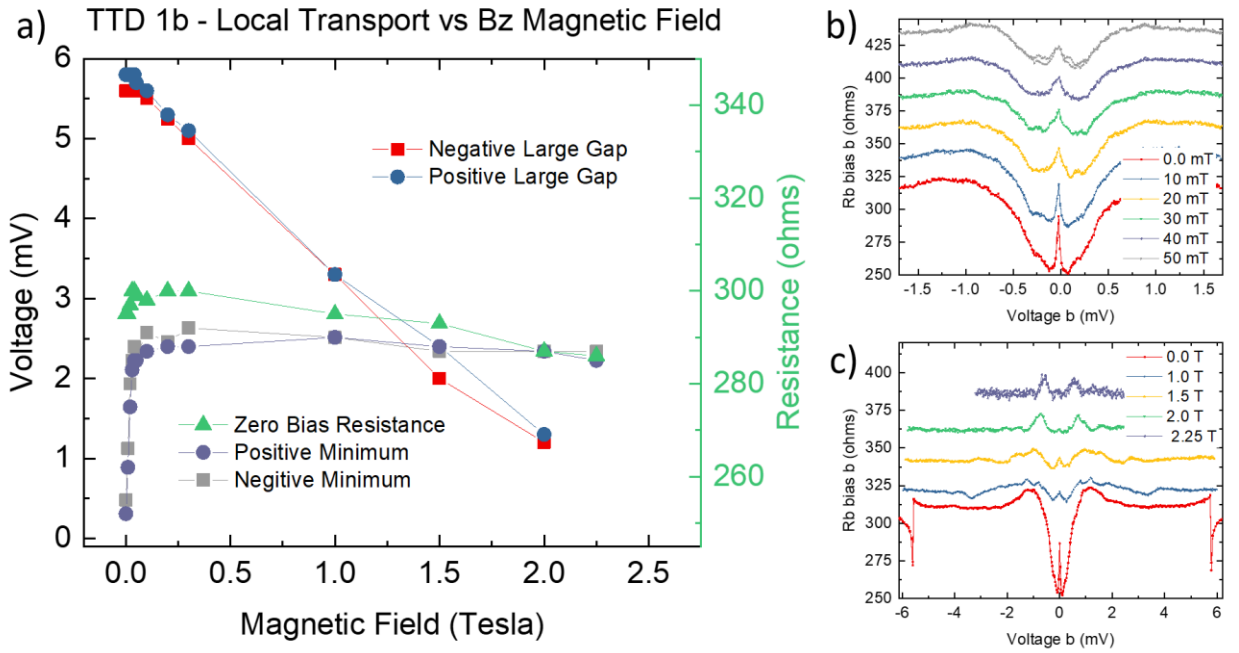

Figure 5.13 The three-terminal device (TTD) 1b B_z field dependence (a) also shows similar behavior to TTD1a. Applying a small field quickly fills in the low bias resistance dip (b). At large fields, the zero bias resistance shows little dependence on field while the energy of the high bias resistance minima decays linearly with field to the highest fields measured. The resistance peaks at the edge of the low bias resistance dip show little dependence on magnetic field and are still present at the highest fields measured as seen in (c). In (b) and (c) the plots are offset for clarity.

One of the powerful things about the three-terminal geometry is that the same superconducting region can be investigated from two different sides to confirm the behavior of the proximity region. Three terminal device 1b exhibits the same behavior with as TTD 1a with some minor differences. The large resistance features at high bias follow the same behavior as in TTD 1a with slow change at low field before dropping to zero at 5 Kelvin. The zero-bias resistance peak drops from almost exactly the normal state resistance at zero bias to a minimum at 800 mK before slowly rising like the zero-bias resistance did in TTD 1a. The broad resistance dip at zero bias fills in with temperature without any noticeable decrease in the energy width of the feature.

Other than the height of the zero-bias resistance peak, the other feature that TTD 1b has that is not present in TTD 1a is the resistance peaks at the edge of the small resistance dip. Their magnitude does not change significantly until the large resistance dips move in energy at which point they lower in magnitude without moving in voltage.

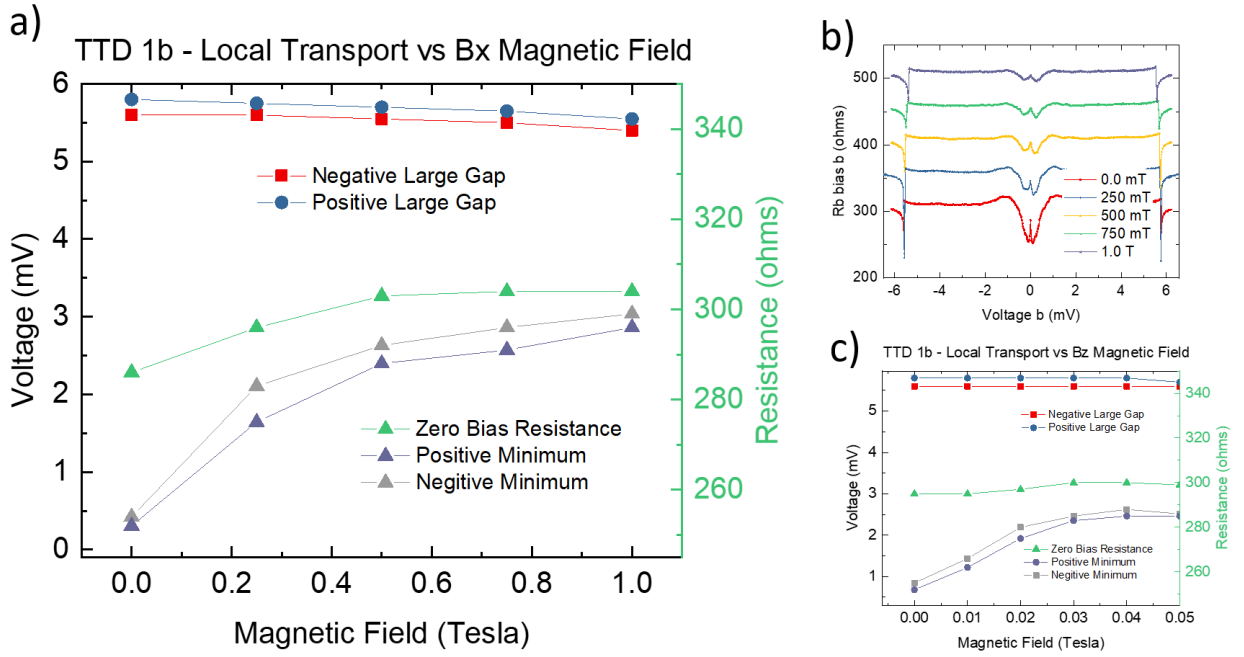

Figure 5.14 Three-terminal device 1b resistance feature dependence with in plane B_x field (a) shows a weak influence of the zero bias resistance and high bias dip location. The low bias resistance dip fills in rather than closing in energy as seen in the DC bias dependent resistance (b). For comparison, the low B_z field range of the resistance features (c) shows similar behavior to the in-plane field dependence up to 1 Tesla. The plots in (b) are offset for clarity.

The qualitative features from TTD 1a are replicated in the B_x and B_z magnetic field sweeps of TTD 1b. The zero-bias resistance quickly rises from the its minimum at zero field to the normal state resistance by 30 mT. As the depth of the broad resistance dip rises, there is little effect on the zero-bias resistance in comparison. The high bias resistance dips move linearly in energy with magnetic field, notably also broadening as they did in TTD 1a. The resistance peaks at the edge of the central feature show very little dependence on the movement of the low bias resistance dip or the high bias sharp resistance dips with magnetic field. The in-plane magnetic field changes

the high bias features little, even up to 1 Tesla in field. The broad zero bias resistance dip slowly and monotonically fills in with B_x from a minimum at 0.0 T to just below the normal state resistance at 1 Tesla. The subtle bias dependent resistance oscillations change with applied B_x and B_z magnetic field as happened in TTD 1a. These features provide evidence that the transport feature in TTD 1a and TTD 1b that are both probing the same physical region, are also probing the same physics.

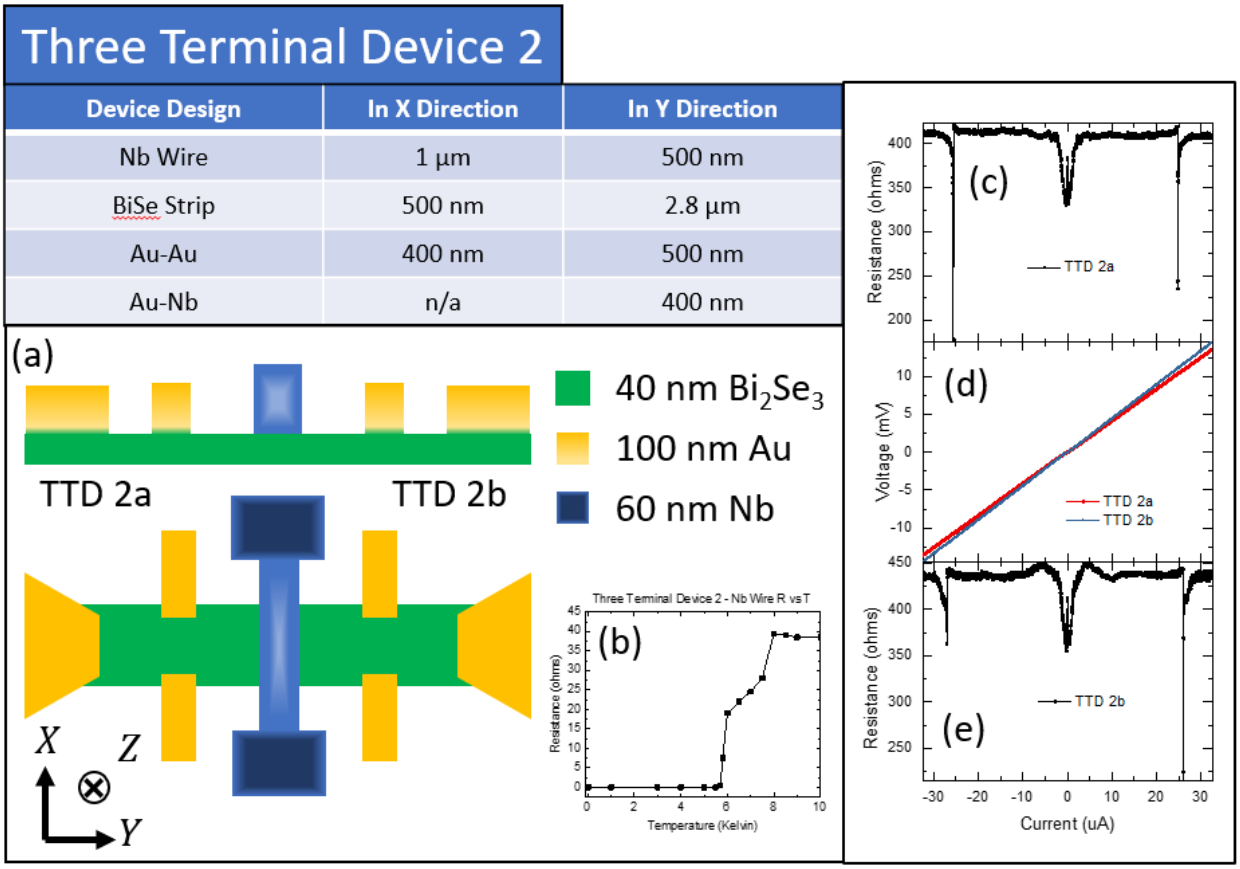

Figure 5.15 Three terminal device (TTD) 2 diagramed in (a) is a symmetrical device where the resistances of the two halves of the device are within 10 percent of each other. The superconducting wire shows a two-step transition (b) with resistance drops at 7.8 Kelvin and 5.75 Kelvin. The differential resistance as a function of each device (c, d) show the nonlinearity of the low bias resistance. The current dependence of the voltage (d) curves show that the two resistances are comparable. Device TTD2a shows a resistance drop near zero bias with a central resistance peak pinned at zero bias. Device TTD2b shows similar features to TTD1b including resistance peaks at the edge of the central resistance dip and a zero bias resistance feature pinned at zero bias.

5.1.3 Select Data from other Three Terminal Devices

Now that the broader picture has been introduced with TTD 1a and TTD 1b, TTD 2 and TTD 3a will be introduced. TTD 2 has two contacts of comparable resistances with a Nb wire that is wider than the Nb wire in TTD 1. It was fabricated on the same chip as TTD 1 with the same Nb and Au depositions. The other local resistance sample that will be presented is TTD 3, a device with a factor of 30 asymmetry in the contact resistances. This device has a higher resolution B_z sweep that includes fields up to 4 Tesla. Together these 3 samples will motivate the model of the system for nonlocal resistance measurements.

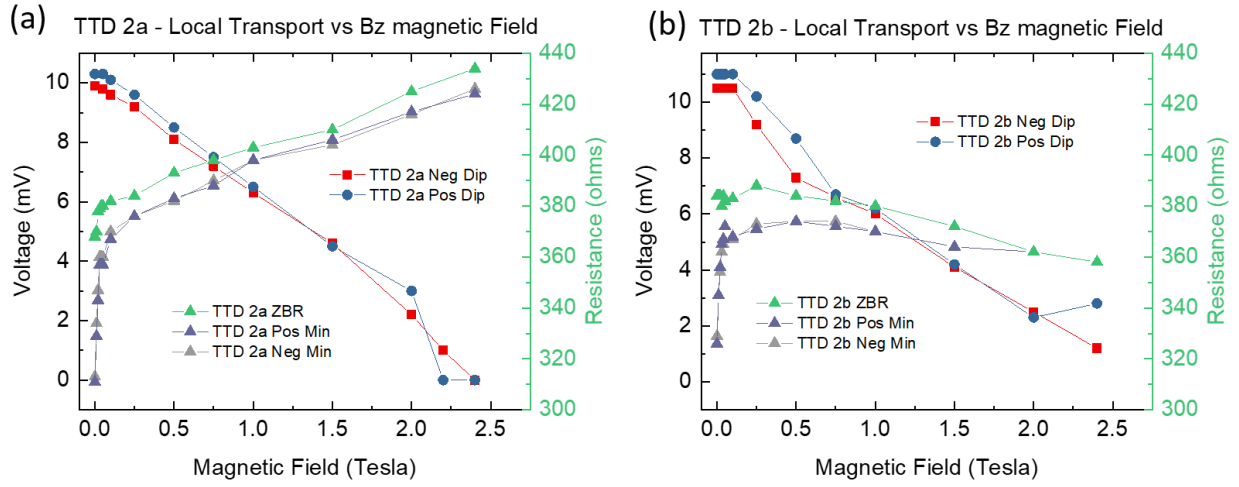

Figure 5.16 For three terminal device (TTD) 2a (a) and TTD2b (b), the perpendicular magnetic field B_z causes a rapid increase in resistance as the resistance dip fills in at low field. The bias voltage of the high bias dips is linear in magnetic field, just like in TTD1 shown in Figure 5.10. There is also a gentle monotonic change in the resistance with field in the high field regime that shows an opposite dependence in the two devices.

The two contacts in TTD 2 provide an example of symmetric contacts that probe a proximity region under the same Nb wire. Contact TTD 2a shows the same broad resistance dip in Figure 5.15 around zero bias as shown in TTD 1a. The device is nominally identical to TTD 1a except that it has a wider Nb wire. This is reflected in the higher microwire transition temperature of in the resistance vs temperature plot in the inset of Figure 5.15. The resistance of TTD 2a reflects many of the features in TTD 1a including the zero bias resistance peak, the broad zero bias

resistance dip, the medium bias resistance oscillations, and the high bias resistance dips. Likewise, TTD 2b reflects many of the features in TTD 1a including the medium bias resistance peaks.

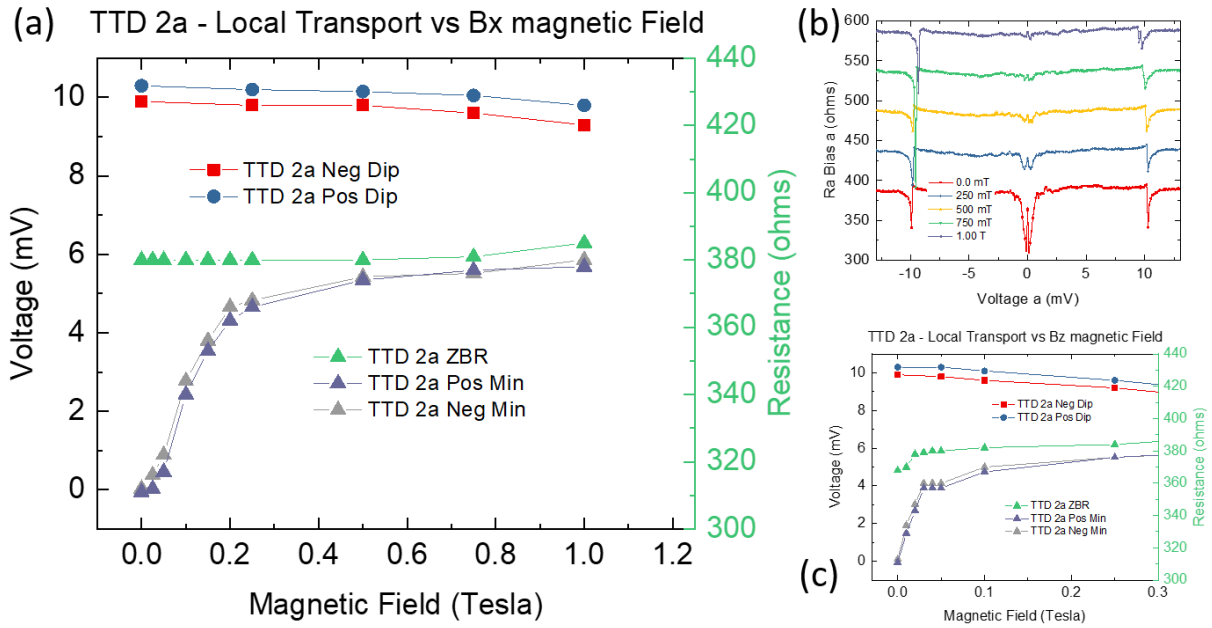

Figure 5.17 The in-plain magnetic field in three terminal device (TTD) 2 shows much weaker dependence on the field as compared to the perpendicular field (a). The zero bias resistance shows little change with field, but the resistance dip is suppressed by 500 mT as seen in (b). The low field regime of the perpendicular field is shown (c) for comparison. The in-plain field sensitivity in TTD2 is a factor of 3 weaker than the B_z sensitivity. For TTD1, the field sensitivity is a factor of 20 smaller for in-plain field as compared to B_z.as shown in Figure 5.14. The TTD1 B_x field is applied perpendicular to the Nb wire, where as in TTD2 B_x is applied parallel to the wire. The plots in (b) are offset for clarity.

The magnetic field dependence for TTD 2 is plotted in Figure 5.16 and Figure 5.17 with behavior that is qualitatively similar to TTD 1. The high bias resistance dips move linearly in energy with their energy going to zero above 2.5 T. The broad zero bias resistance dip is quickly suppressed with B_z before slowly climbing in TTD 2a and slowly lowering in TTD 2b. The zero-bias resistance peak in TTD 2a initially declines in height as the resistance dip fills in before remaining a consistent height up to the highest field measured. In TTD 2b, the zero-bias resistance slowly increases a small amount before declining slowly to 2.4 T. The zero-bias resistance peak initially declines in height as in TTD 2a and then stays constant up to 1.5 T before diapering into

the oscillations by 2.0 T. The resistance increase in TTD 2a is a factor of 3 larger than the resistance decreases in TTD 2b. The B_x dependence of the zero-bias resistance peak is notably weaker than in TTD 1a, and the suppression of the broad resistance dip at zero bias is surpassed with 200 mT rather than 1.0 T like in TTD 1a. This is only a factor of 4 weaker than the B_z field where as the B_z field was 20 times stronger for TTD 1a. The large resistance dips in TTD 2a do not change significantly with in plane field, which is also consistent with the behavior of TTD 1a. The magnetic field dependence in TTD 2 shows the same qualitative behavior as TTD 1 and shows the local transport for a three-terminal device with symmetrical contact resistances on either side.

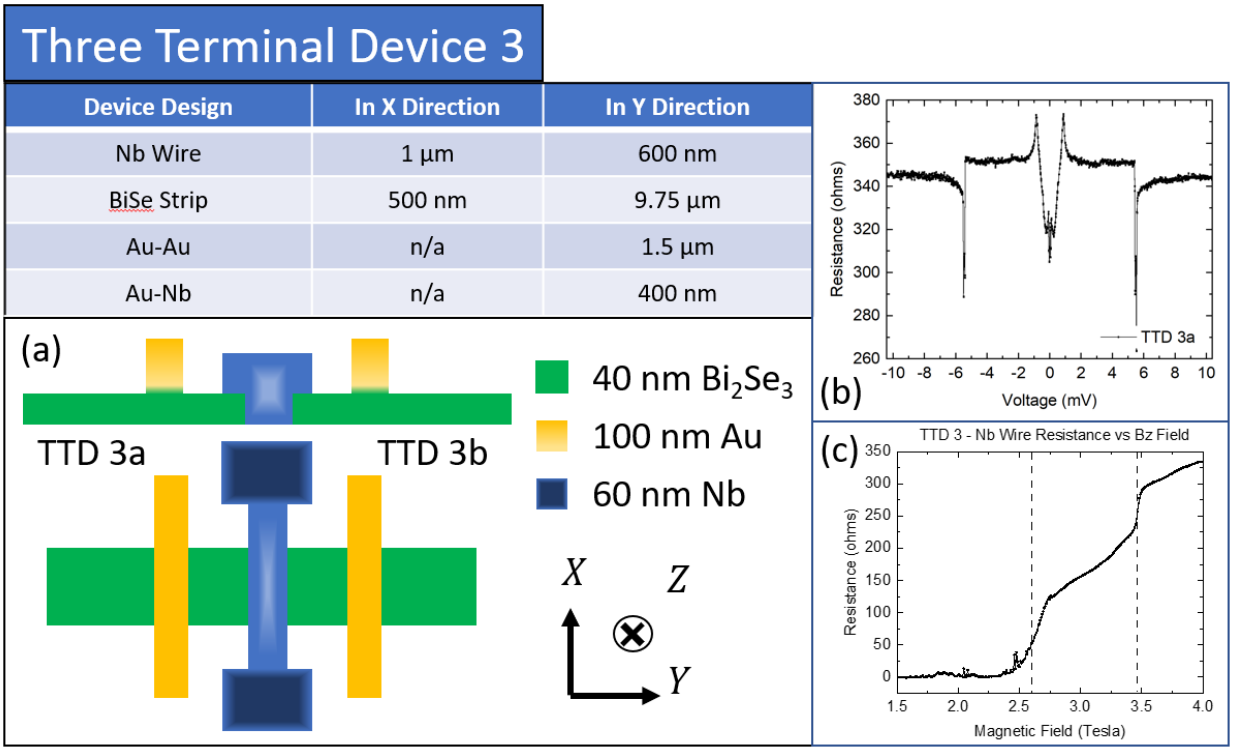

Figure 5.18 Three terminal device (TTD) 3 demonstrates the high B_z field behavior of the effects exhibited in TTD 1 and TTD 2. Its geometry is shown in (a). The device resistance (b) shows high bias resistance dips, sharp peaks at the edge of a broad resistance dip with another resistance dip located at the bottom of it. There is a small resistance peak located at the bottom of the smaller dip that makes it hard to see the small resistance dip. At high bias there are sharp resistance dips as seen in TTD1b and TTD2b. The field dependence (c) of the Nb wire resistance shows a two-step transition with one step at 3.5 Tesla and the other just above 2.5 Tesla. Another feature of this device is that the topological insulator leads on each side are separated by a trench that was milled the same time as the device isolation trenches on the chip.

Three terminal device 3 (TTD 3) has a slightly different geometry and was measured up to 4.0 T in B_z. The Nb wire is the same width as in TTD 1, but it has a trench milled under the Nb strip isolating the two contacts on either side of the device. The Au strips do not contact the sides of the strip, rather they pass all the way across from one side to the other. The local transport of TTD 3a shows two separate resistance dips centered on zero bias, one of which has resistance peaks at its edge. Centered on zero bias there is a zero-bias resistance peak that rises from the bottom of the smaller resistance dip up to the top of it. At high bias there are resistance dips that are qualitatively the same as in TTD 1 and TTD 2. The high resistance side, TTD 3b, shows a central zero bias resistance peak with no features on it. After initialization of the lock in amplifier, the contact was still showed a resistive signal despite its high resistance.

The magnetic field dependence of TTD 3 shows a two-step transition in the resistance of the Nb wire, and multiple transitions in the energy evolution of the high bias resistance dip energy. The two transitions in resistance of the Nb wire at 20 mK are at 2.46 T and 3.6 T, which correspond to features in the field dependent energy of the high bias resistance dips. The field dependent energy of the high bias resistance dips shows three distinct regions with kinks between them. The lowest field range is similar to the field behavior of the contacts in TTD 1 and TTD 2 with a linear decrease in voltage as a function of field to 1.5 T. From 1.5 T to 2.5 T, the graph changes to a flatter slope before changing to an even lower slope at 3.6 T. As in TTD 1 and TTD 2, the zero-bias resistance dip is quickly destroyed with magnetic field before a slow and steady increase in resistance up to the normal state resistance after the lower of the two transitions in the Nb wire. Even at high field there is still evidence for a zero-bias resistance peak. Most surprisingly, the resistance dips at the edge of the larger broad zero bias resistance dip appear to still be present at 4.0 T.

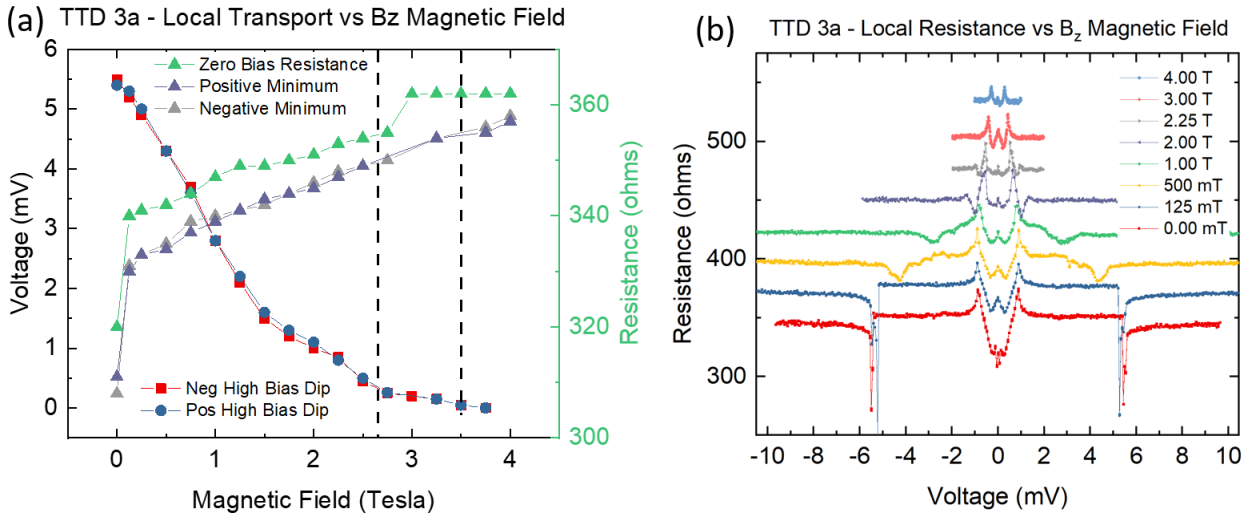

Figure 5.19 In three terminal device (TTD) 3, the low and mid field dependence of the resistance (a) mirrors that of TTD1 and TTD2. At high field, the zero bias resistance hits a plateau at 3 Tesla while the minima near zero bias continue to rise. The energy that the high bias resistance dips are located at shows a linear trend with an inflection point near 1.5 Tesla, and a slow decay above 2.5 Tesla when the resistance of the Nb wire has increased as shown in Figure 5.18 (c). The bias dependence of the resistance plotted at different fields (b) shows that the resistance peaks at the edge of the resistance dip persist to 4 Tesla, the highest field measured in these devices. The curves in (b) are offset for clarity.

5.2 Three Terminal Device Model System

At this point enough evidence has been presented that a reasonable model of the device physics can assembled to help guide interpretation of more complicated measurements. The model will include the resistance oscillations at medium bias, the broad resistance dip, the zero-bias resistance peak, and the high bias resistance dips.

The resistance oscillations at medium bias that are most pronounced in TTD 1a and TTD 2a exhibit many of the properties consistent with universal conductance fluctuations (UCF)[69]. These fluctuations in resistance result from counterpropagating electrons through disordered paths in the topological insulator (TI). The counterpropagating electrons interfere constructively and destructively with each other to modulate the resistance. At elevated temperature, UCF are well known to become smaller in magnitude without moving in voltage due to the increase in thermal fluctuations that result in dephasing[46]. The field dependence is also consistent with UCF where

the modulations change in phase as the enclosed magnetic field adds to the relative phase between the counter propagating electrons while maintaining amplitude of order one conductance quantum[69]. Similar resistance oscillations were also attributed to UCF in work by Finck *et al.* in Nb-Bi_2Se_3-Au junctions[46] as reviewed in Ch 3. They also observed some devices that exhibited more pronounced UCF than others. This is also consistent with the expected high mobility topological surface states in Bi_2Se_3.

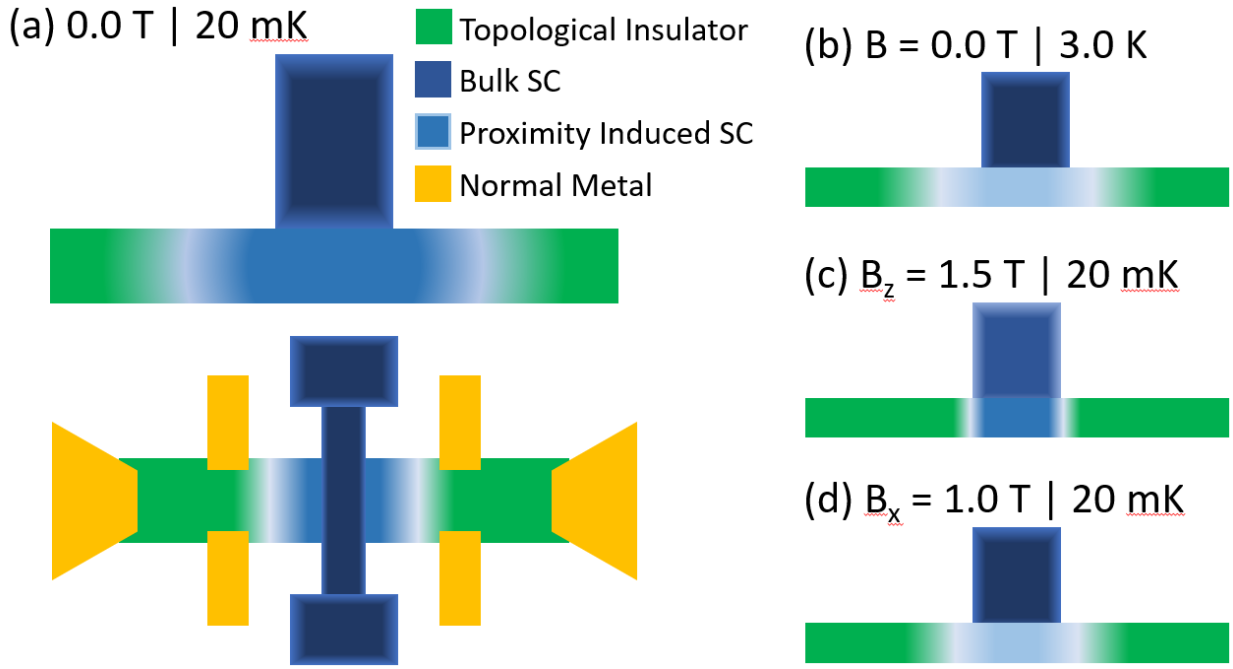

Figure 5.20 The model of a three terminal topological insulator (TI)-superconductor (SC) device at base temperature and in a 0.0 T magnetic field (a). The Nb wire is a bulk superconductor with a strong gap. The TI in contact with the wire is proximitized over a wide range with a smaller superconducting gap. The proximity effect extends in the TI wire beyond the edges of the Nb wire. As the temperature is increased to 3 Kelvin (b), the strength of the SC is minimally affected. The extent of the proximitized SC in the TI decreases, increasing the resistance of the contact without changing the size of the proximitized gap under the SC. In an applied B_z magnetic field (c), the extended proximity effect is quickly suppressed while the SC under the Nb wire is still present due to the screening of magnetic field by the SC lead on top of it. The effect of in-plane magnetic field (d) is much weaker than the perpendicular field as is predicted in G-L theory[4]. This model provides the foundation for the more complicated multi-terminal measurements in the next section.

The broad zero bias resistance dip is consistent with Andreev reflection at a clean interface of a proximity region[45]. In the TI strip, the portion closest to the Nb wire will be proximitized while the section father away will still be in the normal state. The clean interface between the normal and the proximitized region of the TI will form a BTK type junction with a clean interface. The interface will be clean because it is buried in the material, with no interface defects for the electrons to scatter from. In the data this is shown by the reduction of resistance below 1 mV. Using the 1 mV energy of the gaps is a misnomer because of the scaling of energy by the series resistance from the TI strip. This interpretation is similar to the interpretation of Zareapour *et al.* in BiSe-BSCCO junctions[70].

The temperature dependence of the zero-bias resistance peak is consistent with reentrant resistance, however the persistence of a small zero-bias peak at high magnetic fields does not fit with this picture. Below the Thouless energy in proximitized diffusive metals, the local transport increases, approaching the normal state resistance. In these materials the Thouless energy, $E_C = \hbar D/L^2$ where D is the diffusion constant, and L is the size of the proximitized system, is on the order of 100 μV. The width of the zero-bias resistance peak relative to the Andreev gap is consistent with other observations of zero bias resistance peaks attributed to reentrant effects[46] when the device size has been taken into account. A study of the Nb-Au separation should verify that the zero-bias resistance peak is due to a reentrance effect. No systematic study of the Nb-Au separation was done in this work.

There are also several systematic features of the measurements that do not fit into the model. The first is the resistance peaks at 1 mV in the TTD 1b, TTD 2b, and TTD 3a. In point contact spectroscopy literature, resistance peaks above the superconducting gap energy are often attributed to a proximitized region that has a finite critical current[71]. This case is characterized

by movement in bias (voltage) with temperature while the depth of the feature stays constant. Unfortunately, the peaks in this work do not move in energy with temperature or field. An alternative source of resistance peaks in tunneling spectra is when tunneling into an unconventional superconductor with exotic pairing[72]. If the resistance peaks at 1 mV were due to p-wave induced SC at the interface between the Nb and the Bi_2Se_3, then they should disappear as the SC in the Nb is suppressed. The resistance peak features move slightly in energy with perpendicular field, but they are not suppressed. In sample TTD 3a, they persisted above 4 Tesla, well above the critical field of Nb. The 1 mV resistance peaks are features that appear similar to signatures of heating and exotic SC, but their persistence to high fields does not fit with those pictures.

A second feature that persists to anomalously high fields is the small zero bias resistance peak in sample TTD 3a. The form of the high field resistance peak is significantly different from the low field peak attributed to reentrant resistance. The height of the peak is much smaller, it maintains its width in energy to high field, but does not drop off smoothly as the reentrant resistance peak does. It is washed out with temperature, just as the reentrance peak is, but is pinned to zero bias for both in plane and out of plane magnetic fields. It is tempting to attribute such an anomalous peak to Majorana modes as seen in other systems[73], [74], but that does not make sense at fields high enough to suppress the required SC in the Nb.

The instability in the resistance at high bias tracks the superconducting behavior of the Nb wire and is similar to features seen in nonlocal experiments in Al-Au devices. The temperature dependence of the dip energy follows a BCS like fit with a Tc of 5 K, the same temperature that the thin section of the Nb wire goes normal. In magnetic field, the energy of the dips moves linearly in field, similar to the critical current in micro wire strips. When considering heating, it is important to note that the plots above are trace and retrace. There is no evidence of hysteresis

as would be expected if a superconducting microwire were being driven normal. One alternative explanation that accounts for the lack of hysteresis is that the heating is occurring in the TI, a higher resistivity metal than the superconductor. At high bias, the heating in the TI increases the temperature of the Nb wire causing it to go normal. The underlying cause of the high bias resistance dips will be a focus of a later section.

Taking a broader look at the data presented up to this point shows a system with two superconducting regions, one of which is a bulk superconductor and the other being the proximity region in contact with it. We have demonstrated that the two contacts in the representative device are qualitatively the same and are consistent with a picture of a strong gapped bulk superconductor inducing SC in the TI. This working model informed by the local resistance of each contact will prove useful in the next step where non- local effects will be examined.

5.3 Three Terminal Device Nonlocal Effects

Now that there is a working model of the device it is time to explore the unique aspects of having two contacts that contact the same region, specifically the nonlocal resistance and the local resistance as a function of opposite DC bias. With three terminals, the resulting voltage from a bias current can be expanded from a scalar resistance to a matrix of resistances that capture the cross coupling between the two contacts

$$\begin{pmatrix} V_a \\ V_b \end{pmatrix} = \begin{pmatrix} R_{a\ Bias\ a} & R_{a\ Bias\ b} \\ R_{b\ Bias\ a} & R_{b\ Bias\ b} \end{pmatrix} \begin{pmatrix} I_a \\ I_b \end{pmatrix}. \tag{5.1}$$

Each component of the matrix can be measured with a small AC bias, requiring two measurements, one for each of AC “Bias a” or AC “Bias b”, to measure the entire resistance matrix. Combining this technique with a DC bias enables us to find the two-dimensional voltage dependence of the resistance matrix by measuring the differential resistance

$$\begin{pmatrix} dV_a \\ dV_b \end{pmatrix} = \begin{pmatrix} R_{a\ Bias\ a} & R_{a\ Bias\ b} \\ R_{b\ Bias\ a} & R_{b\ Bias\ b} \end{pmatrix} \begin{pmatrix} dI_a \\ dI_b \end{pmatrix}. \quad (5.2)$$

The diagonal terms in the resistance matrix capture the local component while off diagonal term correspond to a non-local resistance.

The focus of this next section will be to explore the bias dependence of the resistance matrix to see what physical insight it can provide into unique aspects of the proximity effect in a TI. For this section, the figures will be configured in such a way that each plot is the corresponding component of the resistance matrix, and all four plots will have the same x axis to help with understanding what is being presented. After introducing the resistance matrix dependence on each bias, IVs as a function of opposite bias will be used as a stepping stone to get to high resolution dual bias sweeps that show the smooth evolution of the resistance features as a function of opposite bias.

5.3.1 TTD 1 – Resistance Matrix as a Function of Bias

The plots in Figure 5.21 and Figure 5.22 show the dependence of the resistance matrix on each of the bias directions. In the plots of the resistance matrix versus bias a in Figure 5.21, some features are present at the same energy in all the plots, but there are distinct differences between the two contacts. The large resistance dips at high bias are present at the same energy in both Ra Bias a and Rb bias a. This suggests that they are due to a part of the device that is common for both leads, possibly the Nb-Bi_2Se_3 interface. As the same energies, the plots taken with an AC bias on contact b show distinct changes in without the resistance dips. The nonlocal resistance in contact a, Ra Bias b, shows zero resistance at energies lower than the energy the resistance dips are at.

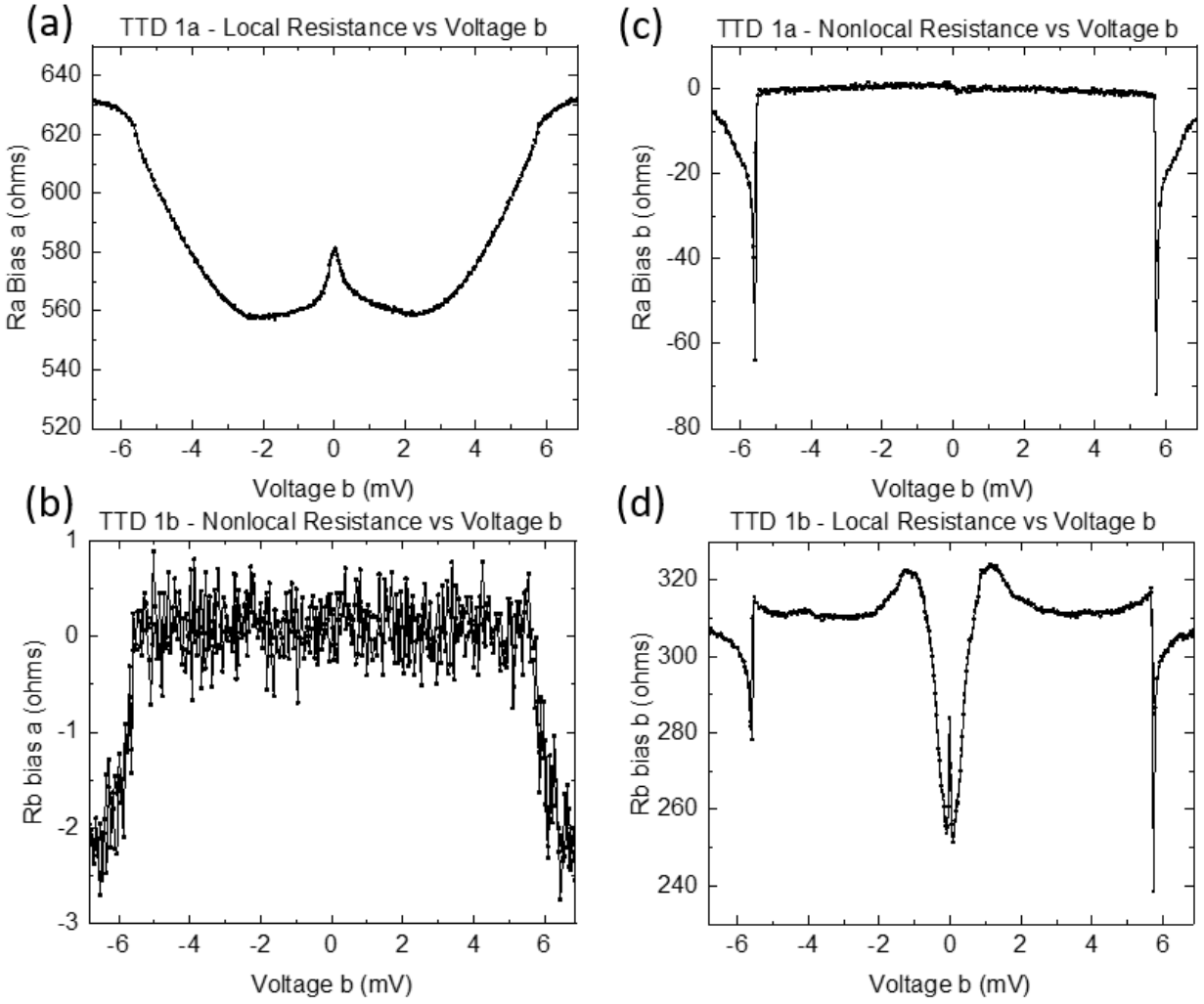

Figure 5.21 The resistance matrix shown here includes all of the couplings outlined in EQ 5.1. The diagonal plots (a, b) show the local resistance of each half of the device as a function of *DC* bias in contact three terminal device (TTD) 1b. The off diagonal plots (b, c) show the nonlocal resistance as a function of the *DC* bias in TTD1b. The bias label on the y axis is with respect to the *AC* bias that is passed through contact a in all of these plots.

Above the dip energy, the resistance drops to -3 ohms. In the Rb Bias b plot, the resistance above the resistance dip energy is flat with very little change. Below the resistance dip energy, there is a smooth drop to a minimum before rising to the zero-bias peak resistance. The resistance matrix versus a DC bias in contact b shows corresponding behavior with the features in contact a and contact b being switched.

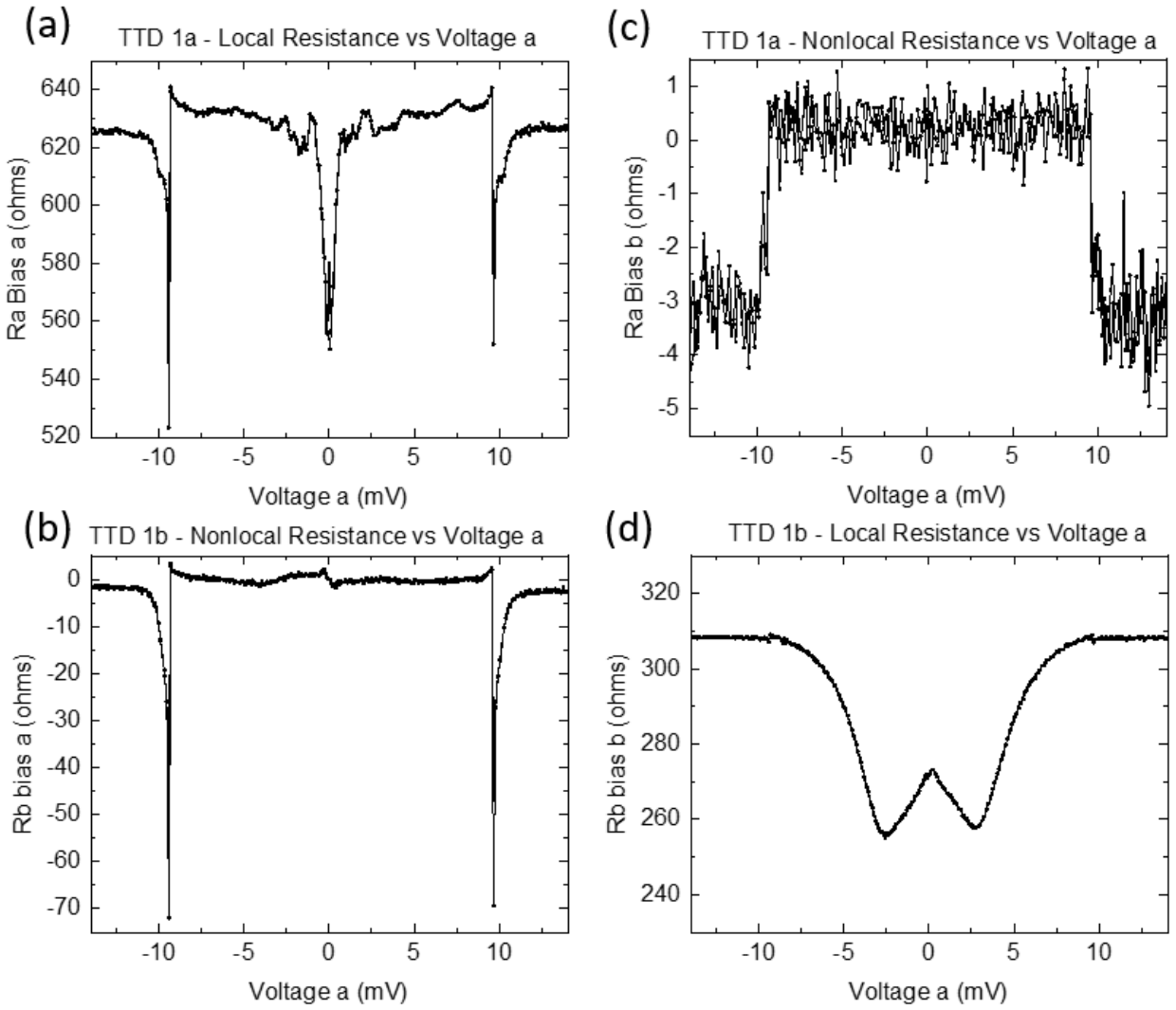

Figure 5.22 The resistance matrix shown here includes all of the couplings outlined in EQ 5.1. The diagonal plots (a, b) show the local resistance of each half of the device as a function of *DC* bias in contact three terminal device (TTD) 1a. The off diagonal plots (b, c) show the nonlocal resistance as a function of the *DC* bias in TTD1a. the bias label on the y axis is with respect to the *AC* bias that is passed through contact a in all of these plots.

With a clear influence of the bias in the opposite contact, exploring the resistance matrix as a function of both DC biases should provide insight into the underlying physics at play. Figure 5.23 shows the resistance matrix plotted as a function of the DC voltage in contact a for different currents in contact b. In the local resistance, the zero bias features are suppressed, and the high bias resistance dips lower in energy before disappearing. The high bias resistance dips become asymmetrical at 15 μA in the opposite side. This asymmetry does not show up in the contact b

resistance vs voltage in a. At medium bias in the non-local signal there is also a small asymmetric contribution to the nonlocal resistance of a few ohms. This dependence of the resistance matrix on both biases begs to be explored more.

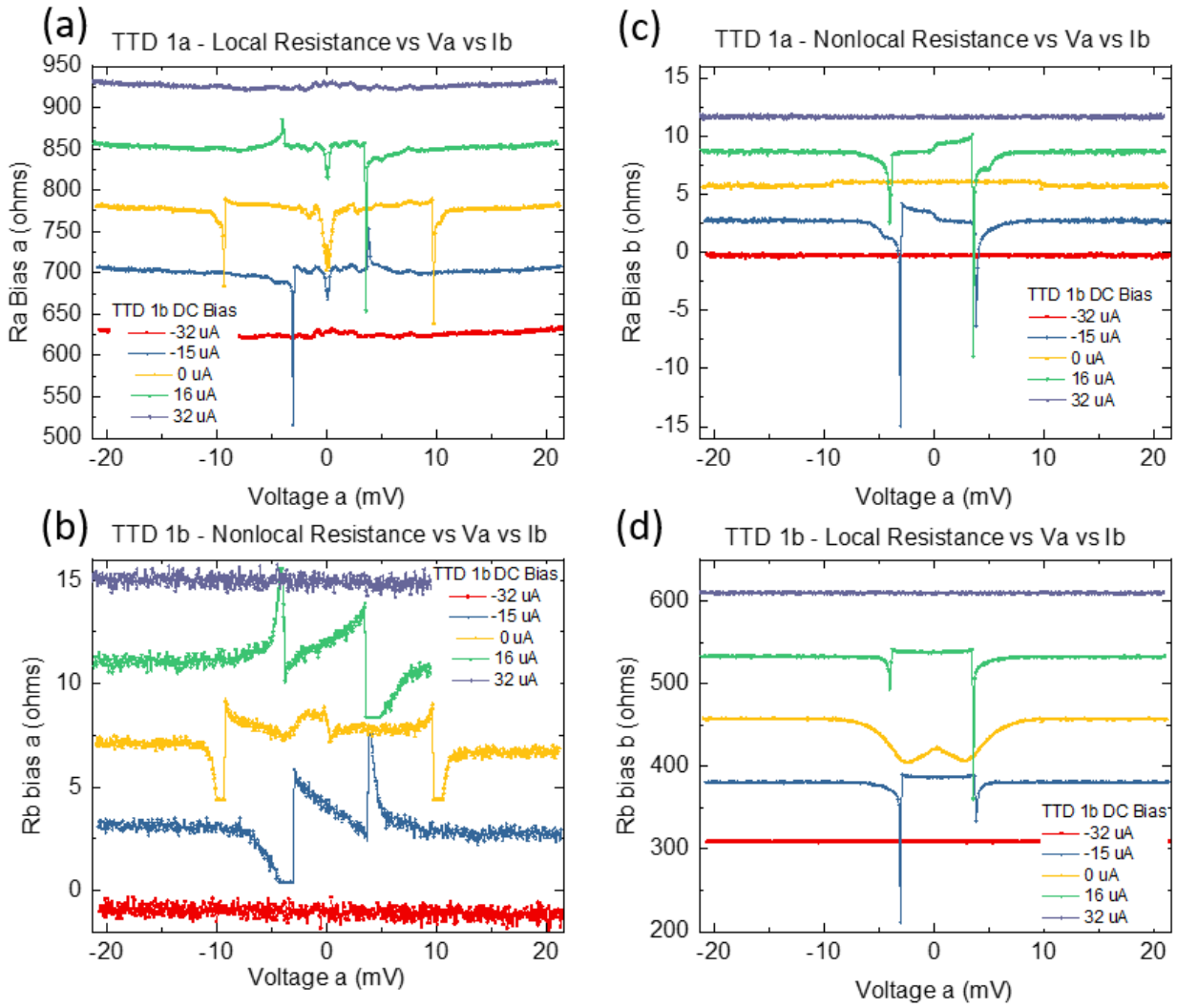

Figure 5.23 Three terminal devices (TTDs) can have dependence of the resistance matrix on the *DC* bias in the other half of the device. The local resistance where Ra(b) Bias a(b) is when the *AC* modulation is applied to the same side that the *AC* voltage response of the system is measured. Alternatively, Ra(b) bias b(a) is when the *AC* current modulation is applied to the opposite half of the device as where the *AC* voltage response is measured and is referred to as the nonlocal resistance. All four configurations show a dependence on both the measured *DC* voltage across device TTD1a, and on the *DC* bias current through device TTD1b. The *DC* bias curves are offset for clarity.

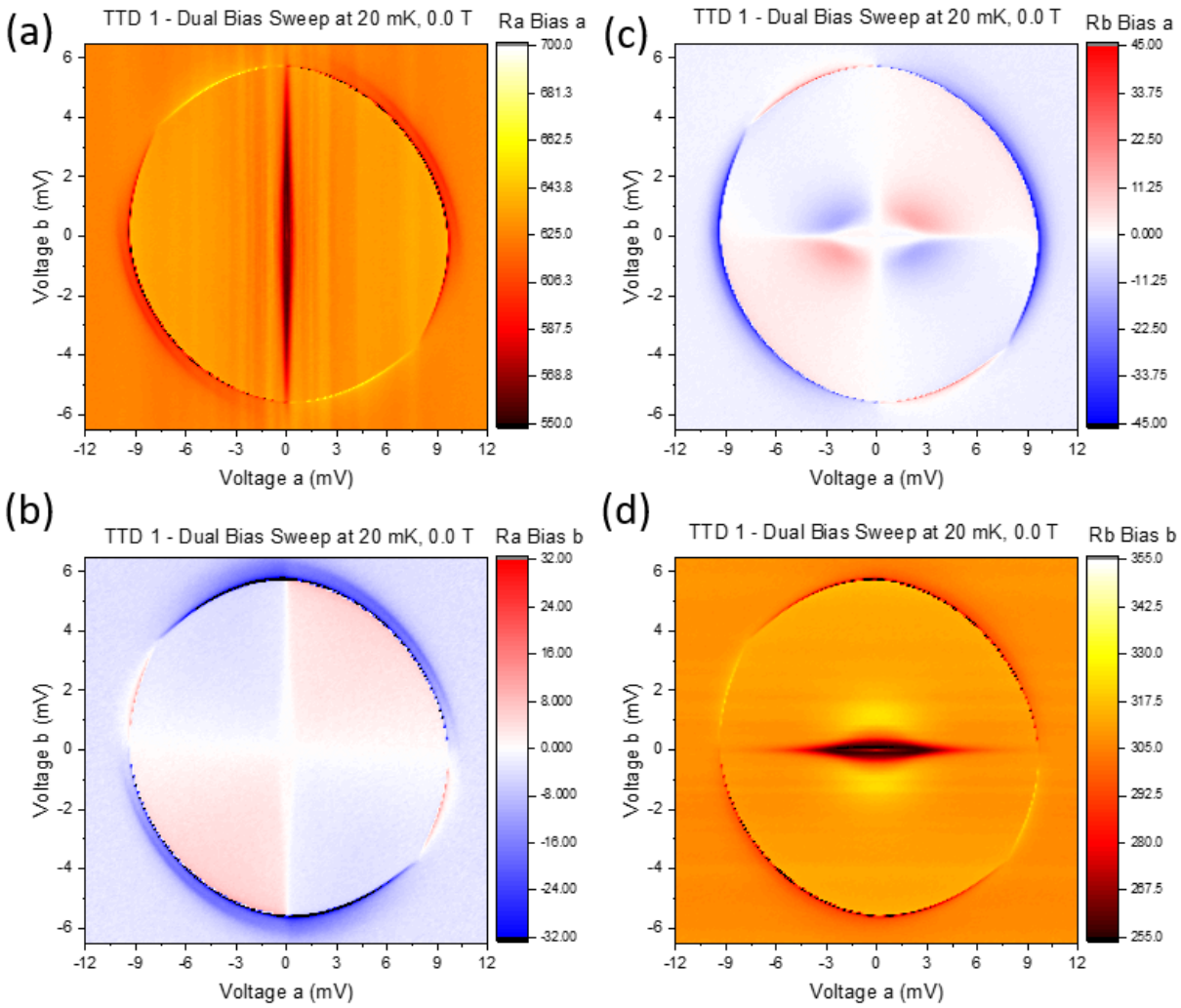

Figure 5.24 Three terminal device (TTD) 1 resistance matrix mapped out as a function of bias in each of the halves of the device. In (a) and (d) the local resistance modulations at medium bias show little dependence on the *DC* bias in the opposite half of the device. The high bias features show a dependence on the sum of the *DC* current squared into the device. The low bias features show a weak suppression with an increase in opposite *DC* bias. The nonlocal resistance shows a signal that is anti-symmetric in both bias currents as well as a low bias regime with zero response. The high bias features show the same dependence as the high bias features in the local resistance for that half of the device.

High resolution sweeps of each bias provide more insight into the nature of the features in the resistance matrix. Figure 5.24 shows the resistance matrix as a function of both biases with three distinct types of features. The medium bias resistance oscillations show no dependence on the opposite bias. The resistance peaks and the high bias resistance dips look like circles in the

dual bias sweep, suggesting that they are proportional to the current or voltage squared. The low bias features show a weak dependence on the opposite bias. In the off-diagonal elements of the resistance matrix, the high bias features are reproduced along with their dependence on the current squared. The low bias resistance asymmetry reflects the symmetry in the side that is being measured more than the side that is being biased.

5.3.2 TTD 1 – Dual Bias Sweep at Finite Field and Higher Temperature

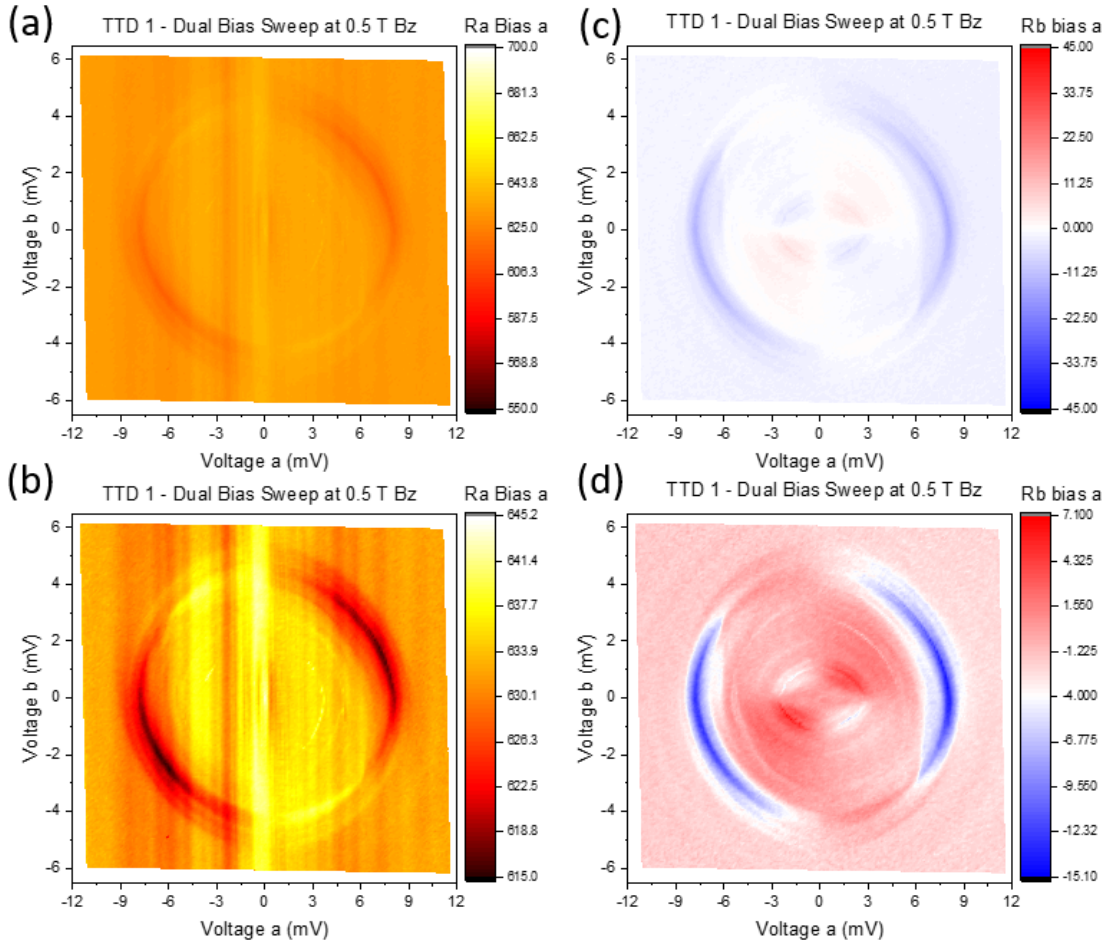

Figure 5.25 Three terminal device (TTD) 1a local resistance (a) and TTD 1b nonlocal resistance (b) mapped vs *DC* bias in both halves of the device at 0.5 Tesla B_z. Compared with Figure 5.24, the resistance dip is washed out at low bias, and the high bias features are not as sharp as at zero field. The medium *DC* bias stripes are still present but show different characteristics in (a) compared with Figure 5.24 (a). The data in (a) and (b) are plotted on the same color scale as in Figure 5.24 while the same data on an expanded range is plotted in (c) and (d) to highlight plot details.

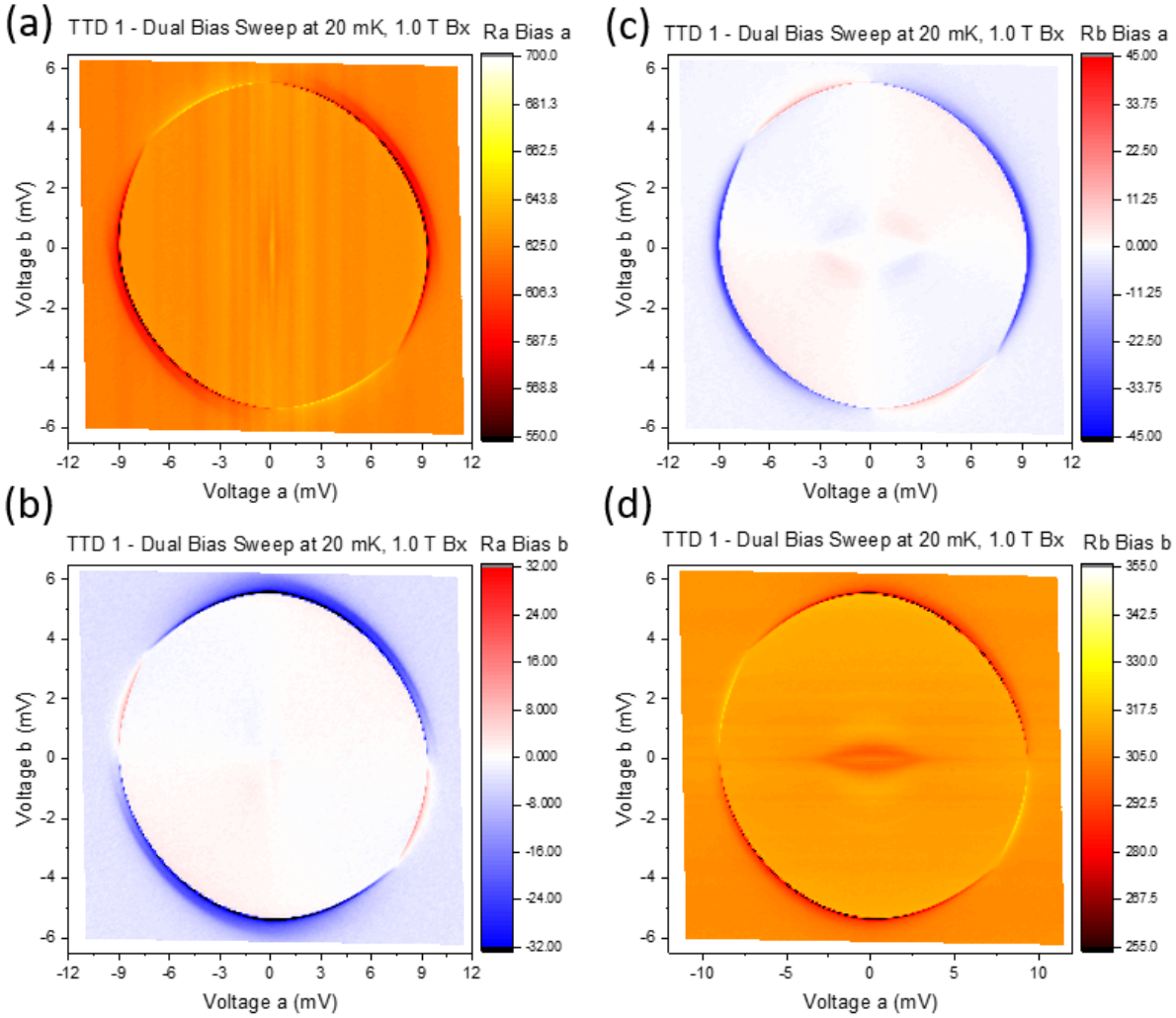

Figure 5.26 Three terminal device (TTD) 1 resistance matrix at an in-plain field of 1.0 Tesla. The plots of local resistance (a, d) show suppressed low bias features with little effect on the high bias resistance dips. The medium bias resistance oscillations show little change from the zero-field data shown in Figure 5.24. The nonlocal resistances (b, c) show large suppression of the low bias features, with little effect on the high bias features. In TTD1, the B_x is applied perpendicular to the superconducting wire.

The magnetic field dependence of the dual bias sweep reflects the features in the zero-field dual bias sweep with the energy dependence that is shown in the local resistance. With B_z, the high bias resistance dips are spread out and move to lower energy. The medium bias resistance oscillations remain the same magnitude as they evolve with field. The low bias features are suppressed in magnitude just as the broad resistance dip is suppressed quickly with an applied

perpendicular field. With the in-plane direction, the low bias features are all suppressed with field. The medium bias resistance oscillations evolve in field while staying the same magnitude. The high bias features show little evolution with in plane magnetic field. The asymmetry in the nonlocal resistances tracks the depth of the broad zero bias resistance dip in the local transport.

5.3.3 Other Three Terminal Devices – Dual Bias Sweep at Higher Temp and Field

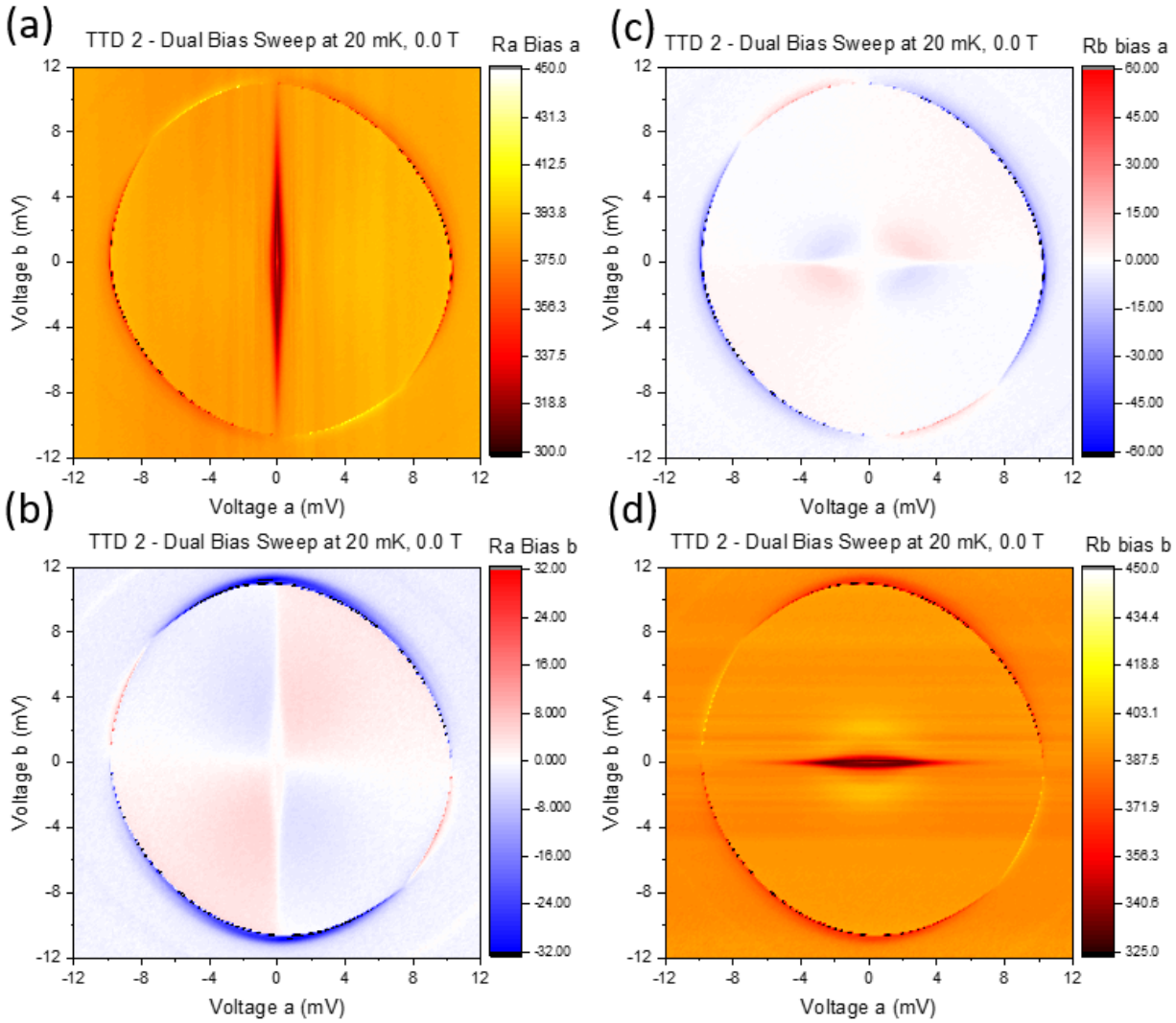

Figure 5.27 Three terminal device (TTD) 2 shows qualitatively the same features in the resistance as a function of biases in both halves of the device as TTD1. The low bias features in the local resistance (a, d) show a weak suppression with increased bias in the other half of the device. The high bias features are circular in both the local and nonlocal resistance, suggesting a dependence on a sum of the squares of the applied bias currents. The mid bias resistance oscillations show little dependence on the bias in the opposite half of the device.

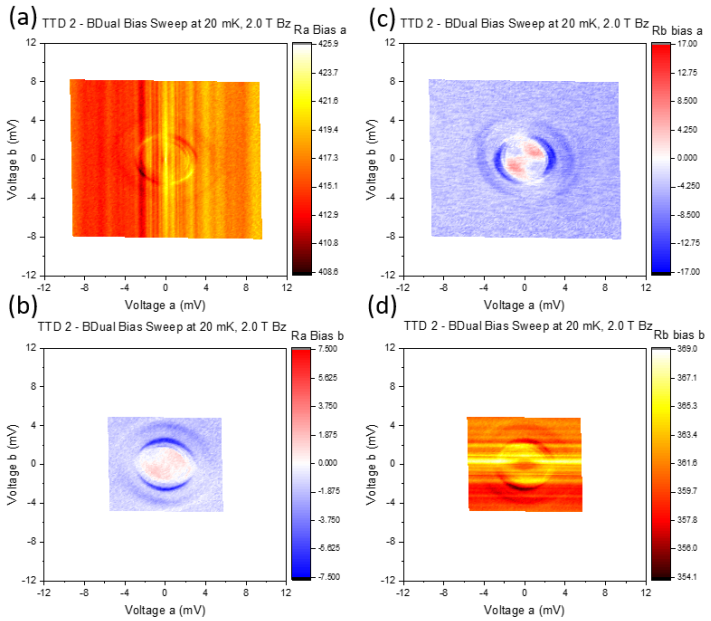

Figure 5.28 The resistance matrix from three terminal device (TTD) 2 measured at a B_z of 2.0 Tesla and 20 mK shows a suppression of the energy at which the high bias features are present. The low bias resistance dip has been filled in. The *DC* bias ranges are the same as in Figure 5.27 for easier comparison. The resistance ranges have been rescaled to highlight the features in the data.

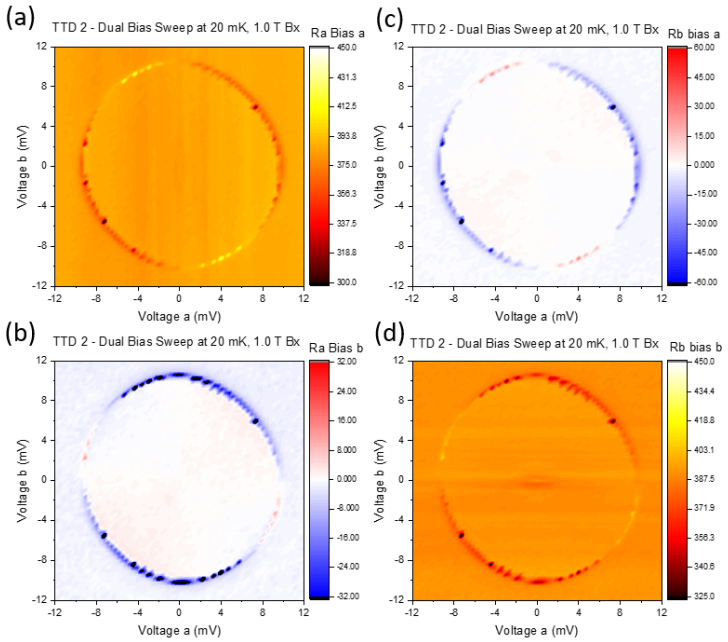

Figure 5.29 Three terminal device (TTD) 2 resistance matrix measured with B_x of 1.0 Tesla shows little difference from the plots from TTD 1 in Figure 5.26. The low bias features are suppressed by the in-plain field while the high bias features are unaffected. The sporadic dark points on the circular features are due to the large step size in *DC* bias for these sweeps. The B_x in-plane field is applied parallel to the superconducting wire in TTD2.

5.3.4 Physical Insight from Dual Bias Sweep

The dual bias sweeps provide additional information about the physics underlying the resistance features in the three terminal devices. The interpretation of several of the features is consistent with the behavior with opposite bias including the UCF, reentrant resistance, and Andreev reflection feature centered at zero bias. The opposite bias sweeps provide some additional information on the nature of the high bias resistance. Several of the features continue to defy explanation, even with the increased information on how they behave versus opposite bias.

The mid bias resistance modulations from the local resistance do not show any dependence on opposite bias, consistent with their interpretation of UCF. The disordered paths in the TI wire away from the superconductor should behave in a normal metallic fashion. In analysis not shown, the high opposite bias curve can be subtracted as an offset from each line to highlight variation with opposite bias. The result is a smooth plot were no oscillations are present.

The high bias resistance dips exhibit expected and anomalous opposite bias dependence in different regions. The feature traces out a path in the dual bias sweep that is a weighted average of the voltage squared. If the feature were due to a critical current in the Nb wire, then the feature should track a line where the sum of the two currents are constant. The simplest mechanism that tracks the bias squared is power dissipation in a resistor. In the symmetric device, TTD 2, the two contacts have almost identical biases that the dips are present at. In TTD 1, with a factor of 2 resistance difference, the feature in the transport of each contact is closer in current than in voltage.

The weak dependence of the low bias resistance dip on the opposite bias is consistent with an Andreev reflection dome. The high bias features that tracked the field dependence of the critical current of the Nb wire show up as circular features in the dual bias sweeps. This is consistent with an effect that is dependent on the weighted sum of the squares of the currents, not the sum of the currents themselves. An introductory physics example of this functional form is of the power

dissipated in a resistor. The dependence of the zero-bias resistance can be used as a calibration between opposite bias and effective temperature. Figure 5.30 shows the opposite bias, and the effective temperature corresponding to the altered zero bias resistance. The plot shows a clear change in slope at 3.5 mV in TTD 1a. The change in slope represents a new conversion factor between current and effective temperature which could come about when a superconducting region goes normal and begins to contribute to the resistance.

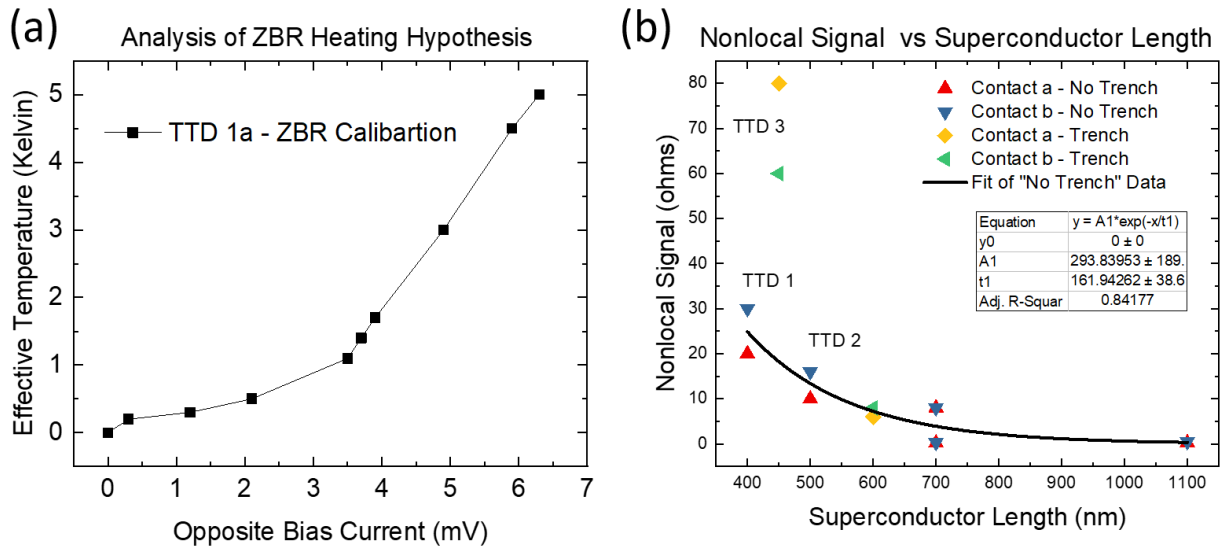

Figure 5.30 Using the temperature dependence of the zero-bias resistance as a thermometer shows what the effective temperature of the device. This can be used to test the effect of the opposite *DC* bias on the effective device temperature shown in (a). The kink in the effective temperature at 3.5 mV shows that the zero bias suppression is not purely due to resistive heating of the device. A summary of all 6 three-terminal devices measured (b) shows an exponential decay in the strength of the asymmetric nonlocal signature for devices without a trench. The resulting decay length of 161+/-38 nm is the same order of magnitude as the coherence length in Nb thin films, which should be the relevant length scale for crossed Andreev reflection and elastic co-tunneling to occur.

Measuring the entire resistance matrix in the dual bias sweeps provides some insight into where different features are in the electrical path. The high bias resistance dips are identical in measurements that are taken at the same time. This implies that the source of the effect is from the common current path of both devices. In the local and nonlocal measurements, the only common current path is the SC-TI interface. Similar resistance dips at a gap edge were measured

in nonlocal measurements in Al-Au[49] systems as outlined in Ch 3. The authors did not provide an underlying mechanism causing the resistance dips above the gap. In addition to the dependence on the opposite bias, the resistance dips change over to a resistance peak when the two leads are biased in opposite directions, passing current across the TI strip. The resistance peak is mirrored in the local resistance as an increase from the background resistance whereas the resistance dips are subtractions from the resistance offset. Confoundingly, the trivial explanation of resistive heating does should not depended on the direction of the current and does not explain why there would be a lack of feature when the currents pass through the TI wire, or why the dip would turn into a peak for the correct bias configuration. The underlying physics causing the resistance dips at high bias continues to be a question that does not have a straight forward answer.

At medium bias there is a nonlocal asymmetry that is odd in both bias voltages. Without comparing it to the local resistance, the best explanation is the inverse galvanic effect[50]. This is caused when a spin imbalance induces a current in a spin polarized lead and has only been observed in ferromagnetic systems. The spin-momentum locking of the surface state provides the spin polarized injected current. With the spin imbalance in place, the spins diffuse across the superconductor and into the TI. Once across the superconductor, the surface state dictates which direction the current will flow based on the induced spin imbalance. This effect captures the asymmetry in the nonlocal resistance that is odd in each bias.

The length dependence of the asymmetry in the nonlocal signal in Figure 5.30b. There is a clear decay of the magnitude of the asymmetry with increasing width of the Nb wire. For devices with a trench in the TI, the decay is significantly sharper than in devices with a TI connection underneath the SC wire. For the devices without a contact, the decay length scale is 161+/-38 nm. Fitting an exponential with zero offset to the two devices with trenches yields a decay length scale

of 65+/-28 nm, which is much shorter than the decay length of the devices without a trench between the two contacts. It is not clear why the coherence length in the superconductor is so much shorter than in the proximitized TI surface states that bridge the SC wire in the devices without a trench. It is clear from the exponential decay length scales that the asymmetrical effect seen in the nonlocal transport is a signature of the proximitized superconducting region. The next section will further seek to shed light on the properties of this region using another well-established probe of superconducting order, Josephson interferometry.

6. Josephson Interferometry on SC-TI Bilayers

With strong evidence for proximitized superconductivity (SC) in the TI strip, Josephson interferometry is a natural technique to look for evidence of the exotic order parameter symmetry that has been predicted for the system. Theoretical work has shown that the mixing of topological insulator (TI) and s-wave superconductor (SC) properties will result in spineless p-wave like SC in the proximity region[16]. In the next section I will present Josephson interferometry measurements aimed at shedding light on the order parameter symmetry of the proximitized region. Signatures of interest that are evidence for p-wave SC include an asymmetrical diffraction pattern due to a complex order parameter[64] as seen in the UPt3, hysteresis resulting from domains[18] as seen in Sr_2RuO_4, and an angle dependence of the critical current due to directional dependence of the gap properties[60].

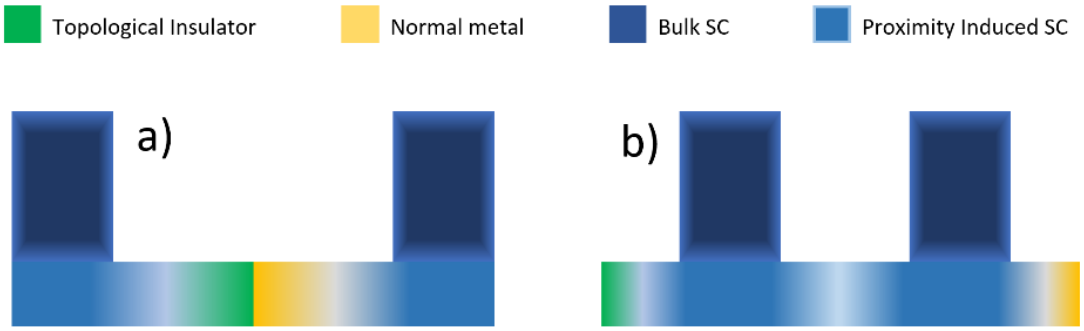

Figure 6.1 The Josephson junctions in this chapter are fabricated by engineering a barrier with a topological insulator-normal metal interface (a). When the junction is cooled to low temperature (b) the proximity effect from the bulk superconducting leads induces superconductivity across the barrier. The extent that this region represents an exotic superconducting state is the focus of this part of the investigation.

The design of the Josephson interferometry devices is an extension of the model described in Figure 5.19 and is shown in Figure 6.1. The main principle of the design is that there is a region of extended proximity-induced SC in the TI. With two superconductors that are brought

close together, the proximity regions will begin to overlap enabling the barrier region to carry a supercurrent. The power of the Josephson interferometry experiment relies on having one of the two leads for the Josephson junction have an isotropic order parameter. Normally this is achieved by contacting a bulk unconventional SC with a normal metal and a conventional s-wave SC. In these experiments the unconventional SC is the proximitized region of the TI, which is contacted with a gold thin film, that in turn is in contact with a SC niobium lead. This section will include data from 2 corner junctions measured at different junction lengths and 1 control edge junction.

6.1 Bilayer Corner Junction 1 – 500 nA Ic, 12-ohm RN

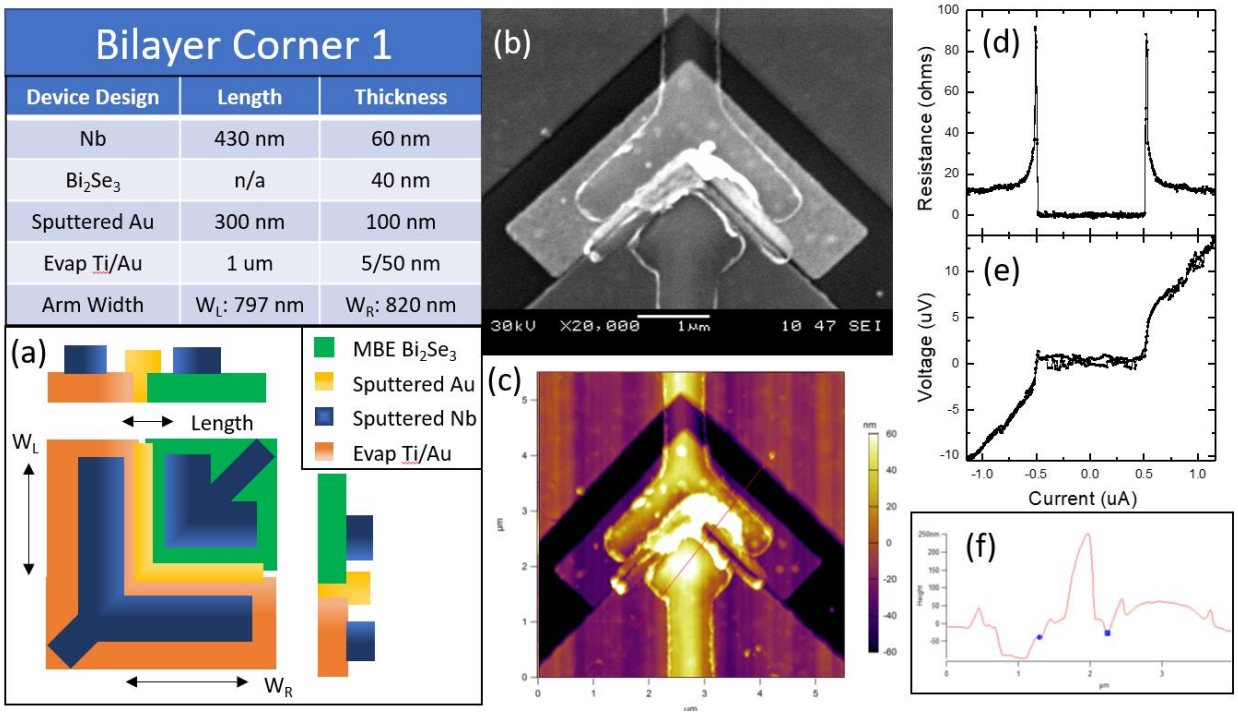

Figure 6.2 The Bilayer Corner junction 1 (BLC 1) dimensions are shown in the table for each arm of the corner junction. (a) Diagram of materials and labeling of orientations of length and width in the table. (b) Scanning electron microscope image of BLC 1 showing the regions depicted in b). d) Atomic force microscope image of BLC 1 corroborating the geometry shown in (b). (d) Resistance vs current plot at 20 mK in zero field showing a clear critical current and a normal state resistance of 12 ohms. (e) Voltage vs current plot showing the DC measurement of the critical current in the device. (f) line cut shown in d) of the BLC 1 profile.

Bilayer Corner junction 1 (BLC 1) was designed to look for signatures of unconventional SC in the field and temperature dependence of its critical current. As shown in Figure 6.2, the two arms of the junction are near 800 nm long and are at a 90-degree angle to each other. The separation of the superconducting leads is 430 nm as measured in an SEM after measurement. When cooled to 20 mK, the zero-field critical current of the junction is 500 nA with a sharp critical current in both the differential resistance measurement as well as the DC measurement shown in Figure 6.2d and Figure 6.2e respectively. A critical current is necessary to show that the device has a weak superconducting link, however field and temperature dependence are needed to show that the critical current is not the result of a micro short in the junction. A micro bridge would not provide useful information on the nature of the superconducting order parameter.

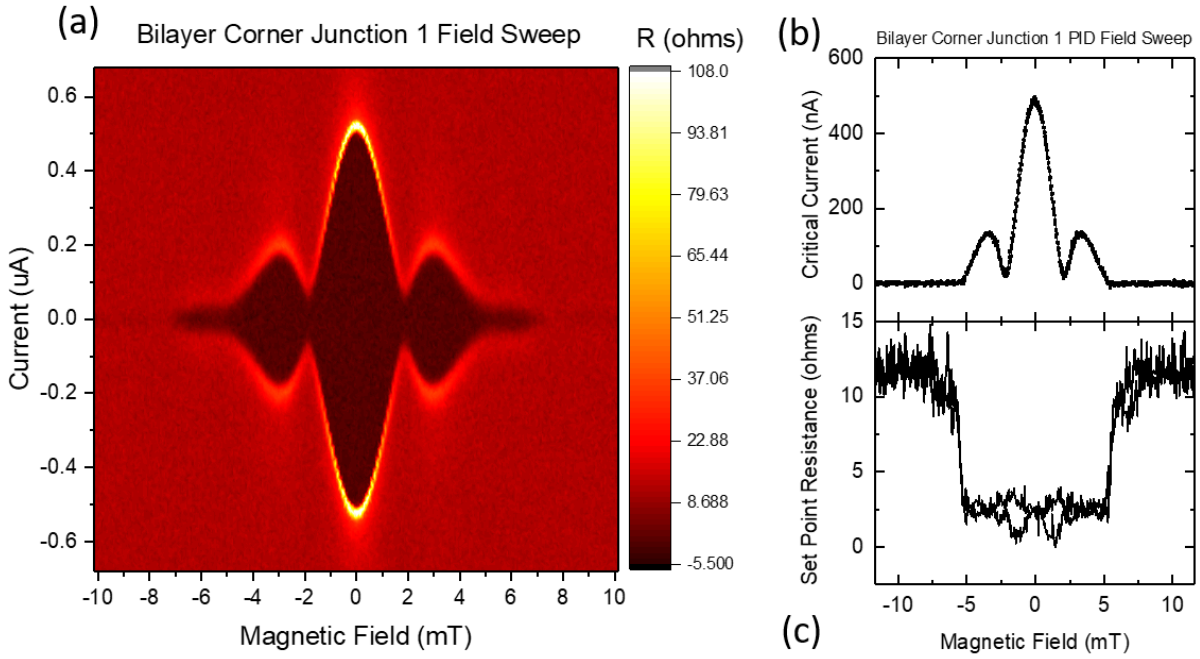

Figure 6.3 a) Resistance map of bilayer corner junction 1 (BLC 1) as a function of applied current and magnetic field. The black region corresponds to the superconducting region where the differential resistance is uniformly at the noise floor of the measurement setup. (b) PID feedback method of measuring the field dependence of the critical current by adjusting the bias current based on a resistance setpoint. (c) field dependence of the resistance set point measured in taking the plot in (b). The high field regions where the setpoint goes above 5 ohms are signatures that the zero-bias resistance is above the setpoint.

The magnetic field dependence of the critical current was measured with two methods to probe possible signatures of unconventional SC in the proximitized bilayer device. In Figure 6.3a the resistance mapping method shows Josephson like behavior of the critical current with field. The peak of the critical current is located at zero field, without any offsets removed from the data. There are two clear lobes with symmetrically lifted first nodes. The second node is slightly lifted with the third lobe being almost entirely suppressed. The critical current at the position of the fourth lobe is entirely suppressed. The nodes of the critical current are not at uniform spacings as would be expected from a Josephson junction with a uniform critical current. Instead the nodes occur at 1.9 mT and 5.1 mT, inconsistent with simulations of a uniform Josephson junction. The resistance map of BLC 1 shows a clear critical current exhibiting Josephson like behavior with some features inconsistent with a uniform supercurrent distribution.

Using the PID method to measure the diffraction pattern reproduces the lifting of the first lobe and the suppression of the critical current at higher field but shows no signs of field hysteresis in the junction. Measuring the magnetic field with this method is extremely sensitive to hysteresis in the magnetic field. The plot in Figure 6.3 b is a trace and retrace, so if there were evidence of hysteretic behavior from domains or trapped flux, this method would measure it. None is seen. It is of no surprise that this method does not resolve a critical current above 5 mT. Figure 6.3 c shows the measured process variable that is compared to the setpoint for determining the bias current to apply. The increase in the measured resistance above 5 mT shows that zero bias resistance of the device goes above the 2.5-ohm setpoint of the PID loop. A keen eye will note the small hysteresis in the resistance setpoint between the first nodes of the diffraction pattern. This can be explained by a lagging of the PID loop behind the high rate of change of the critical current with field in this regime. The monotonic increase in critical current is not lost with this

lagging, so there is no need to worry that the critical current is distorted. The PID loop method show no signs of magnetic hysteresis in the critical current in the junctions.

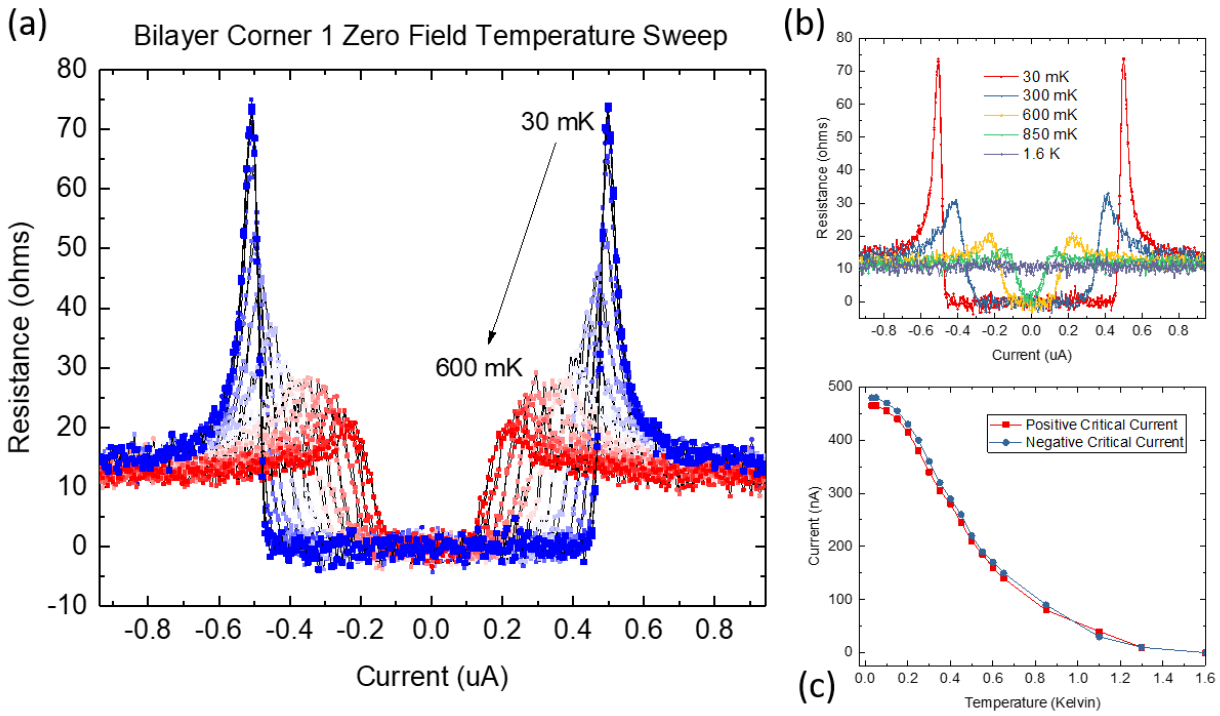

Figure 6.4 (a) Temperature sweep of bilayer corner junction 1 (BLC 1) at zero field. Blue sweeps are cooler, red sweeps are hotter. (b) select temperature resistance vs current plots for BLC 1 from 30 mK to 1.6 Kelvin. (c) Critical current versus temperature plot showing a temperature dependence consistent with a diffusive Josephson junction.

The temperature dependence of the junction can provide information on the nature of the barrier in the junction being diffusive versus ballistic[54]. In Figure 6.4, the temperature dependence of the critical current is shown. There is a sharp critical current from 30 mK up to 850 mK where the zero bias resistance begins to rise above zero. The temperature dependence of the critical current in Figure 6.4c shows a slow decrease in magnitude at low temperature before a regime of steep decay with temperature. At higher temperatures the steep decay slows as the critical current slowly decays below the noise floor at 1.6 Kelvin. This behavior of the critical current is consistent with a conventional superconducting junction with a diffusive superconducting barrier. The key feature of the temperature dependence that demonstrates this is

the leveling off of the critical current at low temperatures. Identifying the junction barrier as a diffusive metal has strong implications that simplify the simulation of the junction behavior with field.

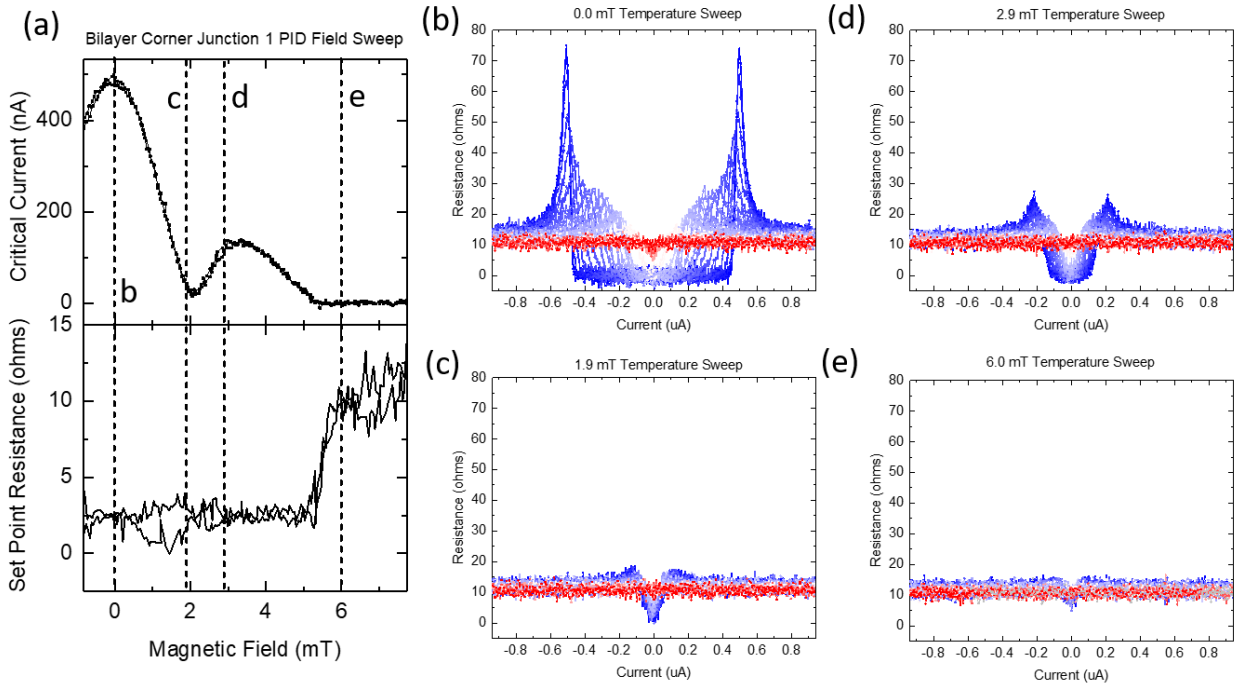

Figure 6.5 a) Cortical current vs magnetic field. Labels correspond to the plots in (b-e). In all the plots, blue corresponds to the lowest temperature measured of 30 mK while the red curve corresponds to 1.6 Kelvin, the highest temperature measured b) Zero field temperature dependence of the resistance vs current plot. (c) Temperature dependence of the resistance vs current plot at the first node of the diffraction pattern. (d) Temperature dependence of the resistance vs current plot at the first love of the diffraction pattern. (e) Temperature dependence of the resistance vs current plot at high field. All plots have the same resistance and current ranges.

To further exhibit the behavior of the junction, the temperature dependence of the critical current was taken at specific fields as shown in Figure 6.5. The four fields were selected to compare the shape of the IV curves at significant points in the diffraction pattern. The plots show that the critical current monotonically decays from a maximum critical current at base temperature to a constant resistance with bias at high temperature. Figure 6.5e shows that there is a small nonlinear component to the resistance, centered on zero bias at high field. The collection of data

from BLC 1 shows Josephson like behavior, however it is not consistent with a uniform Josephson junction tunneling into an s-wave superconductor.

6.2 Bilayer Corner Junction 2 – 200 nA, Rn = 12 ohms

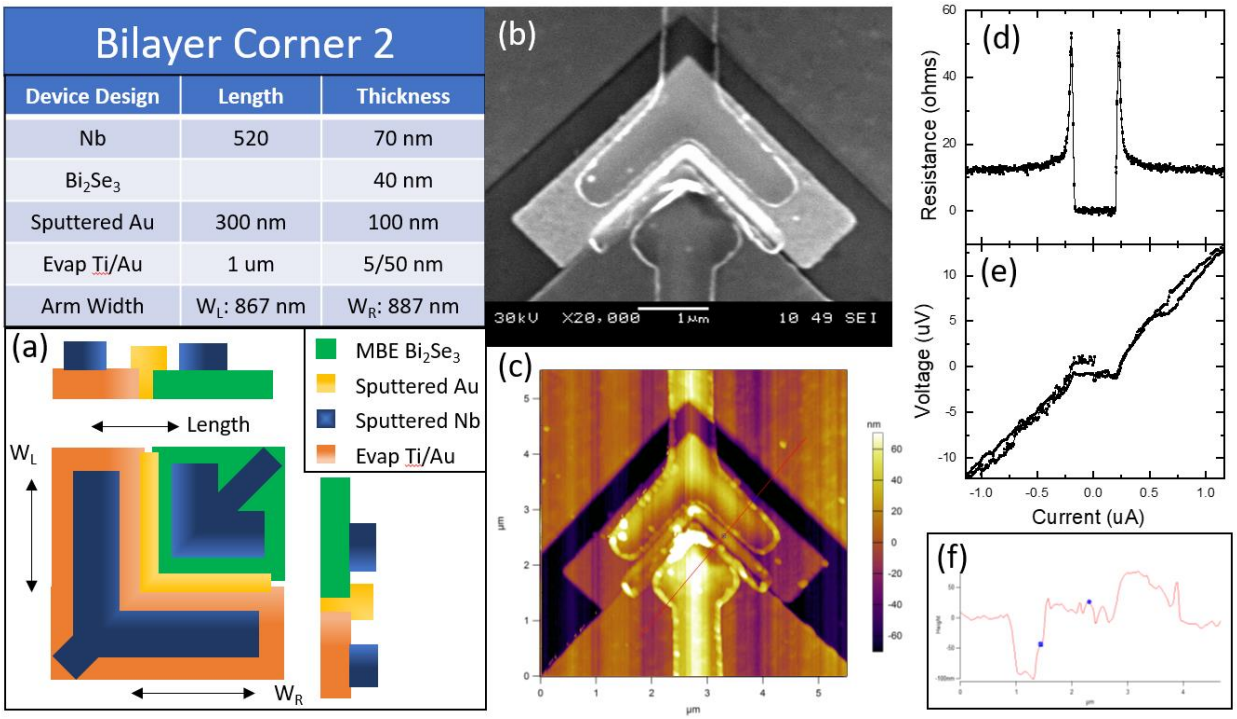

Figure 6.6 A table with the bilayer corner junction 2 (BLC2) device dimensions for each material used is shown. (a) Geometry of BLC 2 with length and width shown in reference to the table dimensions. (b) Scanning electron microscope image of BLC 2 shows the increased gap between the top SC lead and the sputtered Au layer. (c) AFM image of the device. (d) Resistance vs current plot showing a sharp critical current at 250 nA. (e) DC measurement of the low temperature transport exhibits a critical current at the same current it is seen in the differential resistance. (f) line cut shown in d) showing the profile of the device.

The second largest critical current measured in a corner junction was on BLC 2, with a critical current of 200 nA. Nominally the only difference between the two devices is that the SC leads on the evaporated Au contact are 100 nm farther away than in BLC 1. This increase in SC separation results in a smaller critical current, a different effective area of the junction which results in a change of the modulation period of the diffraction pattern. Measurement of the differential resistance shows a clear critical current at 250 nA with a normal state resistance of 12 ohms. The

similarity in resistance between BLC 1 and BLC 2 provides evidence that a majority of the resistance in the junctions comes from the TI lead or the TI-Au interface rather than from the length of the Au portion of the junction.

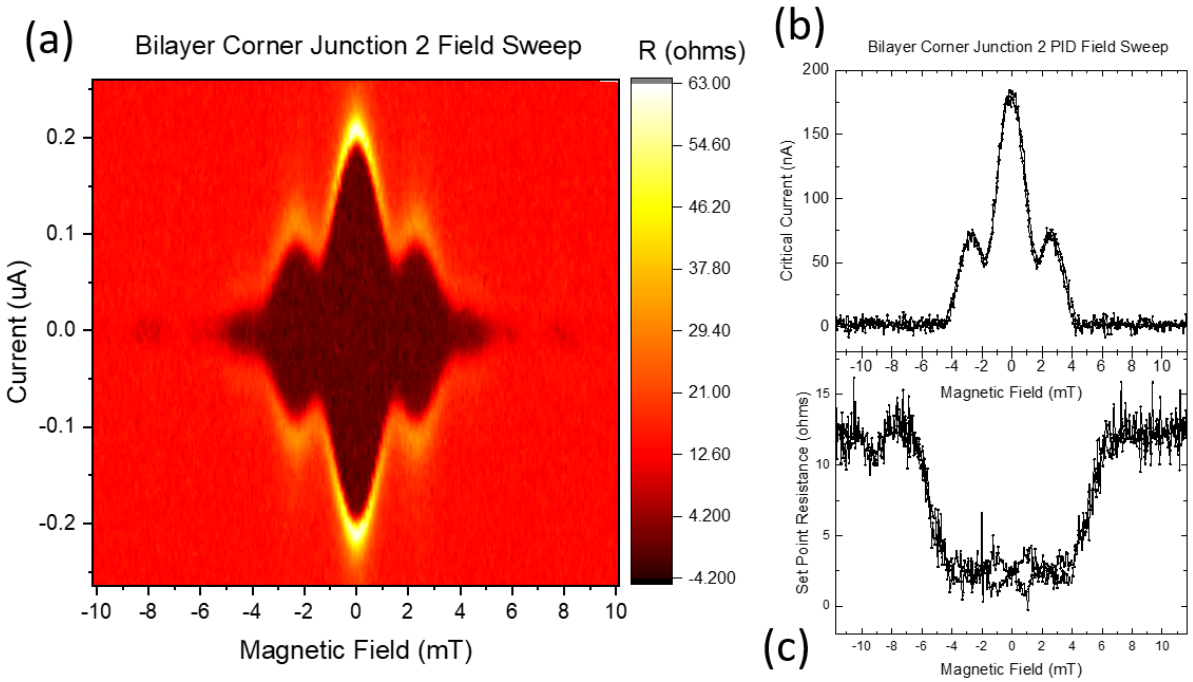

Figure 6.7 The magnetic field dependence of bilayer corner junction 2 (BLC 2). a) resistance map as a function of current and field for BLC 2 with black regions corresponding to the superconducting state. b) PID program measurement of the field dependence of the critical current. c) Plot of the process variable, resistance setpoint, as a function of field as the critical current in b) was being measured. The increase around 4 mT shows that the zero-bias resistance of the junction rose above the 2.5-ohm setpoint at that point.

The diffraction patterns for BLC 2 plotted in Figure 6.7 a and b show qualitatively consistent behavior when compared to BLC 1. The resistance map as a function of bias current and applied magnetic field in Figure 6.7a shows a critical current of 250 nA and a symmetric diffraction pattern around zero field. The PID loop diffraction pattern shows no sign of magnetic hysteresis up to 10 mT, which was also seen in the BLC 1 PID loop field sweep. Both methods of measuring the diffraction pattern show significant node lifting of the first node, a suppressed third lobe, and little beyond that in terms of a critical current. The process variable plotted in Figure

6.7c also shows the small hysteresis in the central lobe of the diffraction pattern where the highest rate of change of critical current with respect to field is located. The measurements of the critical current vs field for BLC 2 are consistent with the results seen in BLC 1.

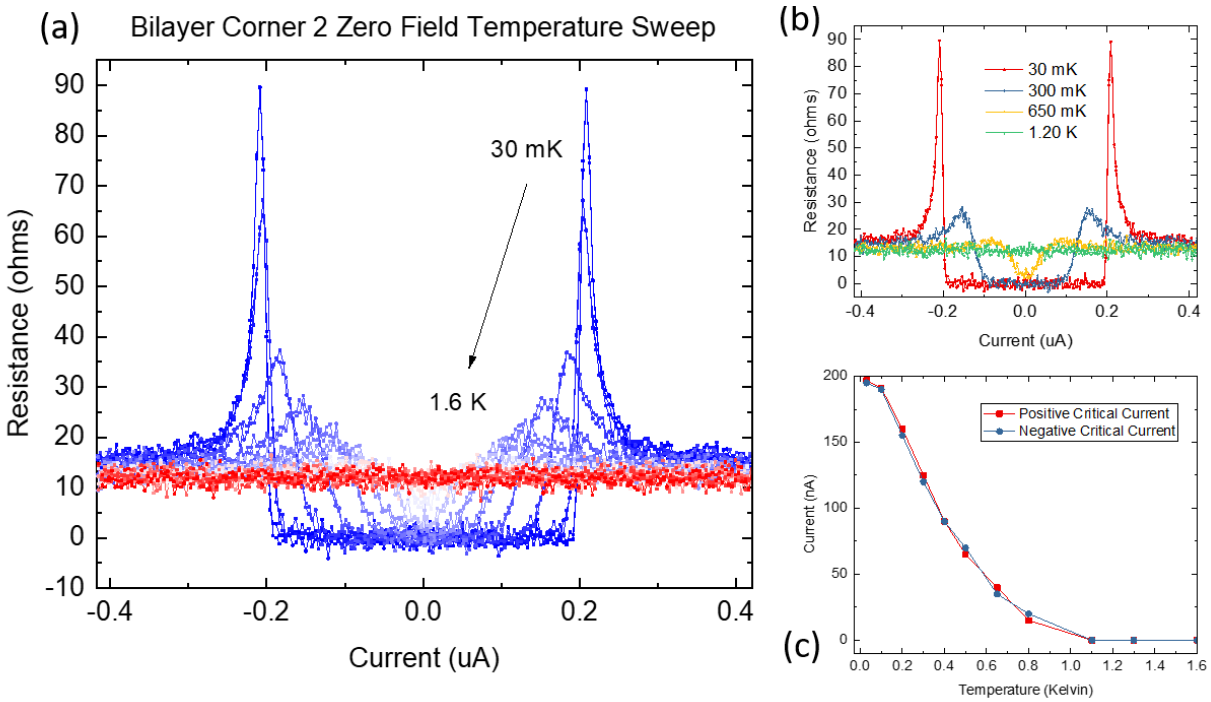

Figure 6.8 Temperature Dependence of bilayer corner junction 2 (BLC 2) at zero field. a) Plot of the resistance vs bias current for several temperatures between 30 mK and 1.6 K. Blue corresponds to the lowest temperature, red corresponds to the hottest temperature. b) select resistance curves showing the shape of the IV at medium temperatures. c) Critical current versus temperature showing both the positive and negative critical current.

The temperature dependence of the critical current also behaves in a similar fashion to BLC 1. At medium temperatures there is a sharp decline in the critical current before it flattens and decays to zero. The low temperature regime shows a flattening of the critical current with temperature that could also be a result of poor thermalization of the electron temperature below 50 mK. With the combination of lower temperature resolution, and a smaller critical current, it is hard to make a firm claim about the junction being in the ballistic regime versus being in the diffusive regime. Considering the materials in question and the clear diffusive nature of BLC 1,

there is no reason to conclude anything other than that BLC 2 is also in the diffusive regime. For completeness, the resistance plots versus temperature at specific fields are shown in Figure 6.9. The first node is lifted so significantly that the base temperature plot looks almost indistinguishable from the plot at the first lobe. The highest field plot in Figure 6.9 shows a small, barely resolvable, nonlinearity for the lowest temperatures before becoming a flat, bias independent resistance.

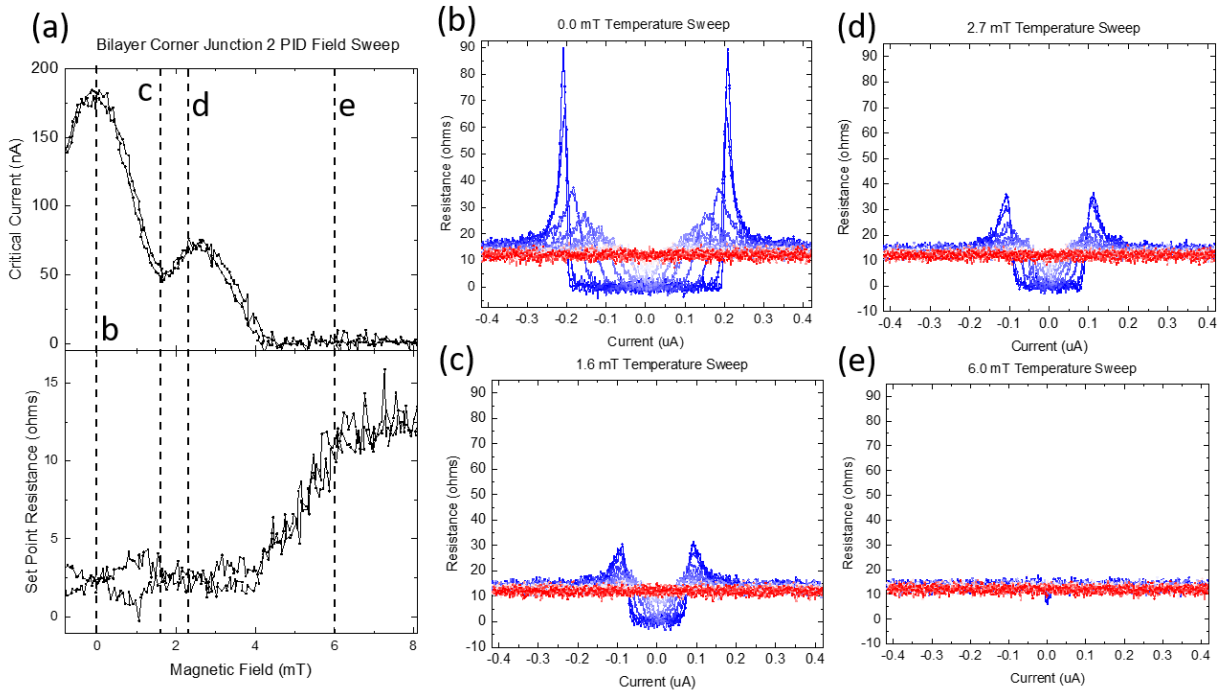

Figure 6.9 Temperature plots of the bias dependent resistance for bilayer corner junction 2 (BLC 2). a) PID diffraction pattern and process variable with labels for the field locations of the other four plots in the figure. b) Temperature dependence of the resistance at zero field (b), the first node (c), the first lobe (d) and at high field (d).

Using the measured dimensions of the corner Josephson junctions, we are able to simulate the behavior of the junction. As outlined in Ch 3, the crossover regime between purely single junction and purely SQuID behavior can result in unintuitive diffraction patterns. The results are shown in Figure 6.10 for the two devices. The periodicity of the adjustment of the location of the first node in the diffraction pattern can be accounted for by the inclusion of a suppressed region of supercurrent. This region acts as a SQuID loop, inducing a jump in the phase difference between

the two angles of the junction. The effect on the diffraction pattern is to shift the location of the first node in field. The lifting of this node is also significant and is best described by a critical current asymmetry. The simulations also capture the decay of the node lifting in the region of competition between the single junction modulation and the SQuID modulation. The washing out of critical current at high field can be attributed to a combination of the field suppression of the extended proximity effect seen in Ch 5, and the suppression of higher lobes due to disorder in the junction. The simulations demonstrate the need for a critical current asymmetry in the junctions resemble the measured diffraction patterns in BLC 1 and BLC 2.

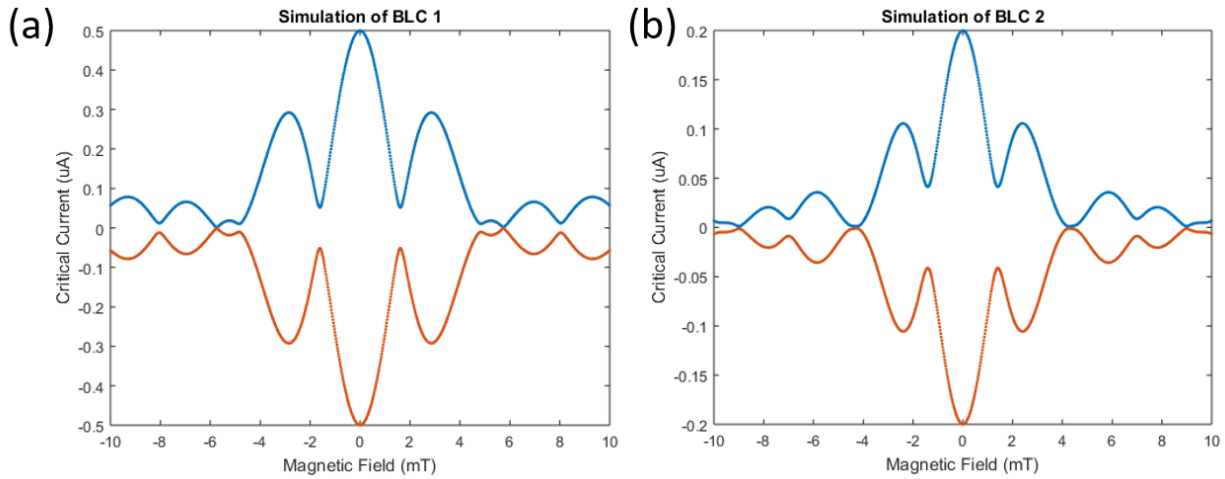

Figure 6.10 Simulations of bilayer corner junction 1 (BLC 1) and bilayer corner junction 2 (BLC 2) using the simulation outlined in the Appendix A. Critical currents of either side of the junction for BLC 1 are 220 nA and 280 nA. Critical currents of either side of the junction for BLC 2 are 75 nA and 125 nA. By fitting to the total critical current, and using the measured device dimensions, simulations of these specific devices were run.

6.3 Bilayer Edge Junction 1 – 200 nA

As a control device, edge Josephson junctions were fabricated without a 90-degree corner. The dimensions of the control device were picked so that the field modulation scale would be similar with the field modulation of the corner junctions. The junction presented here is just over 3 um long and modulates on similar field scales as the corner junctions. The geometry of the

junction is outlined in Figure 6.11, and due to technical difficulties can only be measured with an SC-TI-SC junction in series with it. The two junctions have different areas, so the modulations can be deconstructed. In the resistance plot shown in in Figure 6.11d, the smaller of the two critical currents is due to the bilayer junction whereas the large hysteretic one is from the SC-TI-SC junction. The DC measurements also displays hysteretic behavior with bias current. The normal state resistance of this device is much higher than the other two devices. In this fabrication cycle there was a significantly lower device yield than on the one for the corner junctions. The reason for the different yields is not immediately clear but could be due to a second milling step needed to clean the bonding pad areas from residual material after the normal milling time.

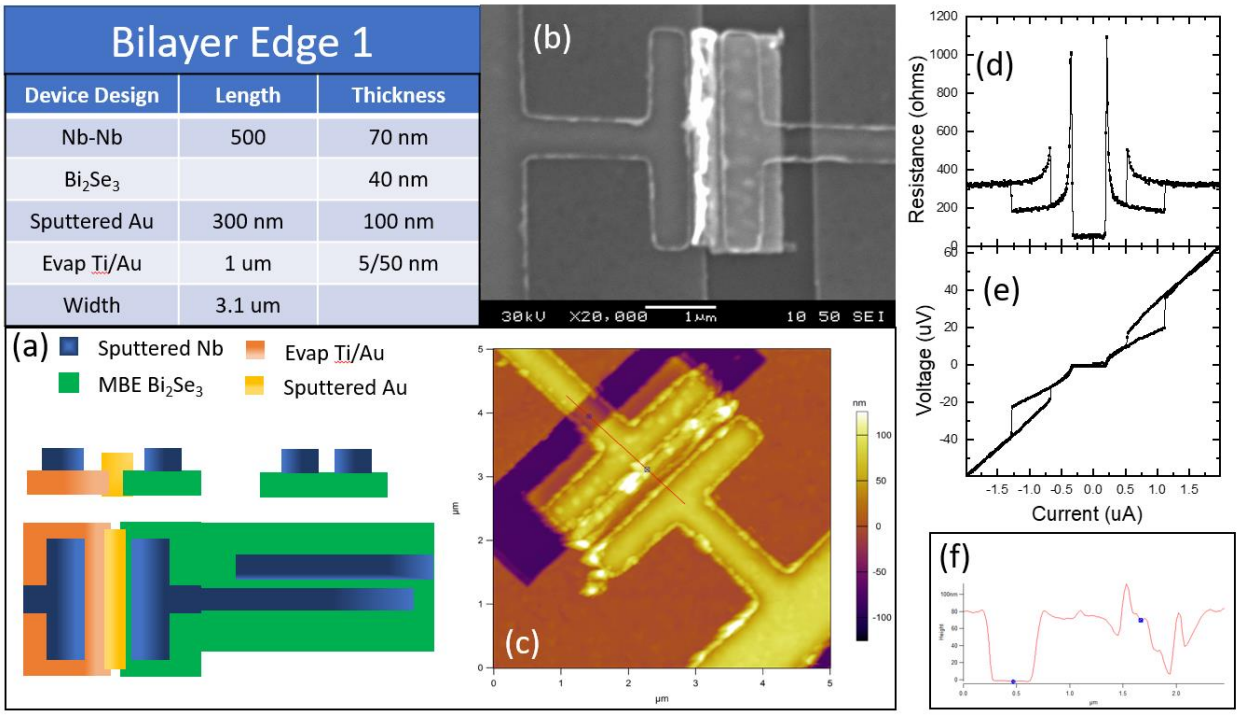

Figure 6.11 a) device geometry for bilayer edge junction 1 (BLE 1). b) Depiction of device geometry with a bilayer edge junction in series with a superconductor-topological insulator-superconductor junction. c) SEM image of the device showing the close alignment of the layers. d) AFM image of the device. e) Resistance vs current shows two critical currents, consistent with two Josephson junctions in series with each other. f) DC IV curve showing the two critical currents measured. g) profile of line cut shown in d).

The resistance and temperature dependence show diffraction patterns with lower nodes, and diffusive behavior respectively. The magnetic field dependence shown in Figure 6.12a. The diffraction pattern is symmetrical with respect to zero field and shows two independent oscillations as would be expected of two Josephson junctions in series. The temperature dependence of the lower critical current, that we attribute to the bilayer junction, shows diffusive behavior with temperature as seen with the corner junctions. This junction provides further evidence that there are not domains in the interfacial SC under investigation. The edge junction provides a control device exhibiting expected single junction behavior with field.

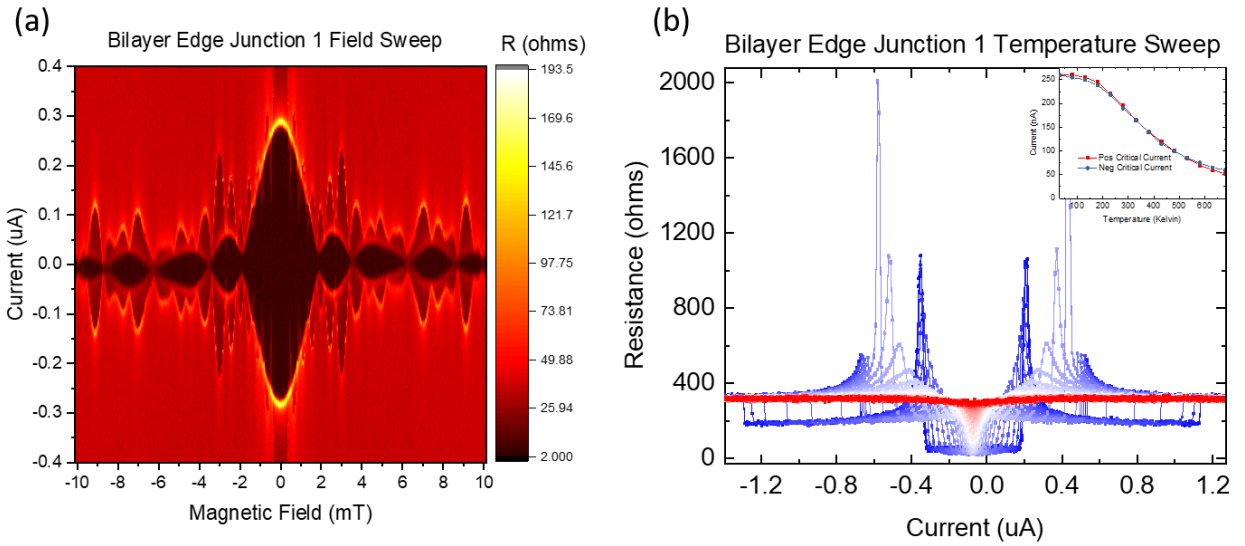

Figure 6.12 Magnetic field and temperature dependence of the bilayer edge junction 1 (BLE 1). (a) Diffraction pattern of BLE 1 and a superconductor-topological insulator Josephson junction in series with each other. (b) Temperature dependence of the resistance versus current. The inset shows the critical current versus field which shows a temperature dependence consistent with a diffusive junction.

7. Conclusions and Future Work

Engineering Hamiltonians is an attractive approach for studying unconventional superconductivity (SC) and realizing exotic electronic states of matter. Topological insulator-superconductor bilayers have been predicted to be strong candidate systems for engineering spinless p-wave SC. This exotic SC should come about from the blending of the spin-momentum locking in the topologically protected surface state with the particle-hole symmetric gap of the superconductor. The main thrust of this work has been to test the properties of Nb-Bi_2Se_3 bilayers for evidence of exotic SC.

First, we presented low temperature transport measurements probing the nature of the SC in bilayers of Nb and Bi_2Se_3. They provided evidence of proximity-induced SC in the topological insulator thin films consistent with a bulk superconductor in contact with a topological insulator. Local transport shows strong evidence for proximitized SC in the topological insulator with an Andreev reflection dome and a reentrant resistance peak centered at zero bias. High bias resistance dips in the local resistance reflect features in the critical current of the Nb wire with variations in temperature, however the dual bias sweeps show current squared dependence. The nonlocal resistance shows an unexpected asymmetric contribution that is odd in both bias currents. At high bias, the Nb-Bi_2Se_3 interface shows an inversion of sharp resistance dips where the two biases are opposite each other. We show evidence for universal conductance fluctuations in the topological insulator wire. The low temperature transport has signatures well described by BTK theory for high transparency interfaces, but also contain unexpected features that could be due to the spin-momentum locking of the surface state electrons.

Future work on local and nonlocal transport should investigate length dependence, gating and making control devices from non-topological materials will continue to shed light on the physics at play in this system. Providing a length dependence of the asymmetry in the nonlocal resistance would provide conclusive evidence to discern between a superconducting and charge imbalance origin. Gate dependence will show whether the Fermi energy is in the bulk, and with materials improvements, will enable probing of the proximitized state at the Dirac point. All the devices presented here had symmetric topological insulator wires as the two leads. Just as comparison between SC-F and SC-N nonlocal measurements provided evidence for spin physics[50], fabricating devices with graphene contacts will provide more contexts to whether the nonlocal asymmetry at low bias is a result of the topological nature of the Bi_2Se_3.

The Josephson interferometry measurements show clear Josephson behavior of the junctions into proximitized Bi_2Se_3. We show that the diffraction patterns from corner junctions can be understood by simulating the corner of the junction as a region with suppressed critical current density. This results in scaling of the nodes of the diffraction pattern due to competition between single junction and SQuID effects. With this interpretation, the node lifting can only be explained by a large asymmetry in the total critical currents of each of the two junctions. This effect is seen in both corner junctions with large critical currents and is not present in a control edge junction. The size of the critical current asymmetry is consistent with a non-isotropic s+p order parameter, although critical current variation due to fabrication could also explain the asymmetry.

Future work on Josephson interferometry should include making wider edge and corner junctions on the same fabrication run as well as exploring the thickness dependence of the Nb film in the bilayer. Making the junction wider will reduce the complexity of untangling the single

junction and SQuID modulation effects. Making both types of devices in the same run will reduce variations in superconductor gap strength and alignment variation that are alternative interpretations of the current work. With an established method for making junctions on the bilayers, testing the thickness dependence of the Nb film should highlight the possible s-wave contribution from the bulk film that is washing out a p-wave contribution from the interface and proximitized region.

This work has contributed to the body of work exploring the physics of proximitized superconducting topological insulators. The work rules out the possibility of domains on the 1 um scale, and magnetic hysteresis from the Josephson interferometry measurements, while remaining consistent with both an s-wave or s+p-wave order parameter. The low temperature transport provides evidence of proximitized topological insulator that exhibits features that track the superconducting properties in the superconducting wire. An unexpected nonlocal resistance odd in the bias of both contacts was observed. In conclusion, the application of two well-known probes of SC, low temperature transport and Josephson interferometry, are contributed to the wider body of work to test the limits of Hamiltonian engineering in the search for unconventional superconducting systems.

8. Bibliography

[1] D. Goodstein and J. Goodstein, “Richard Feynman and the History of Superconductivity,” *Phys. Perspect.*, vol. 2, pp. 30–47, 2000.

[2] H. K. Onnes, “Investigtions into the properties of substances at low temperatures, which have led, amonst other things, to the preparation of liquid helium,” *Nobel Lect.*, vol. 4, pp. 306–336, 1913.

[3] W. Meissner and R. Ochsenfeld, “Ein neuer effekt bei eintritt der supraleitfaehigkeit,” *Naturwissenschaften*, vol. 21, no. 44, pp. 787–788, 1933.

[4] M. Tinkham, *Introduction to superconductivity*. 1996.

[5] W. S. Corak, B. B. Goodman, C. B. Satterthwaite, and A. Wexler, “Exponential temperature dependence of the electronic specific heat of superconducting vanadium,” *Phys. Rev.*, vol. 96, no. 5, pp. 1442–1444, 1954.

[6] M. A. Biondi, M. P. M. Garfunkel, and A. O. A. McCoubrey, “Millimeter Wave Absorption in Superconducting Aluminum,” *Phys. Rev.*, vol. 102, p. 127, 1955.

[7] R. E. Glover and M. Tinkham, “Transmission of superconducting films at millimeter-microwave and far infrared frequencies [2],” *Phys. Rev.*, vol. 104, no. 3, pp. 844–845, 1956.

[8] A. P. Drozdov, M. I. Eremets, I. A. Troyan, V. Ksenofontov, and S. I. Shylin, “Conventional superconductivity at 203 kelvin at high pressures in the sulfur hydride system,” *Nature*, vol. 525, no. 7567, pp. 73–76, 2015.

[9] J. Bardeen, L. N. Cooper, and J. R. Schrieffer, “Theory of superconductivity,” *Phys. Rev.*, vol. 108, no. 5, pp. 1175–1204, 1957.

[10] V. Ginzburg and L. Landau, “VL Ginzburg and LD Landau, J. Exptl. Theoret. Phys.(USSR) 20, 1064 (1950),” *J. Exptl Theor. Phys. USSR*, vol. 20, p. 1064, 1950.

[11] P.-G. De Gennes, *Superconductivity of metals and alloys*. 2018.

[12] L. P. Gorkov, "Microscopic Derivation of the Ginzburg-Landau Equations in the Theory of Superconductivity," *J. Exptl. Theor. Phys. 36, 1918-1923*, vol. 36, no. 6, pp. 1364–1367, 1959.

[13] J. Clarke and A. Braginski, *The SQUID Handbook: Fundamentals and Technology of SQUIDS and SQUID Systems*, vol. 21, no. 5. 2004.

[14] M. Z. Hasan and C. L. Kane, "Colloquium: Topological insulators," *Rev. Mod. Phys.*, vol. 82, no. 4, pp. 3045–3067, Nov. 2010.

[15] X. L. Qi and S. C. Zhang, "Topological insulators and superconductors," *Rev. Mod. Phys.*, vol. 83, no. 4, 2011.

[16] L. Fu and C. Kane, "Superconducting Proximity Effect and Majorana Fermions at the Surface of a Topological Insulator," *Phys. Rev. Lett.*, vol. 100, no. 9, p. 096407, Mar. 2008.

[17] G. R. Stewart, "Unconventional superconductivity," *Adv. Phys.*, vol. 66, no. 2, pp. 75–196, 2017.

[18] F. Kidwingira, J. D. Strand, D. J. Van Harlingen, and Y. Maeno, "Dynamical superconducting order parameter domains in Sr2RuO4.," *Science*, vol. 314, no. 5803, pp. 1267–71, Nov. 2006.

[19] Dan Bahr, "Probing the Chiral Domain Structure and Dynamics in Sr2RuO4 with nanoscale JJs," *Dissertation*, 2011.

[20] E. Majorana, "A SYMMETRIC THEORY OF ELECTRONS AND POSITRONS," vol. 14, pp. 171–184, 1937.

[21] L. Majidi and R. Asgari, "Specular Andreev reflection in thin films of topological insulators," *Phys. Rev. D - Part. Fields, Gravit. Cosmol.*, vol. 93, no. 19, pp. 1–9, 2016.

[22] A. Y. Kitaev, "Fault-tolerant quantum computation by anyons," *Ann. Phys. (N. Y).*, vol.

303, no. 1, pp. 2–30, Jan. 2003.

[23] F. D. M. Haldane, “Nobel lecture: Topological quantum matter,” *Rev. Mod. Phys.*, vol. 89, no. 4, pp. 1–10, 2017.

[24] J. M. Kosterlitz and D. J. Thouless, “Long range order and metastability in two dimensional solids and superfluis.,” *J. Phys. C Solid State Phys.*, vol. 5, p. L124, 1972.

[25] D. J. Thouless and J. M. Kosterlitz, “Ordering, metastability and phase transitions in two-dimensional systems,” *J. Phys. C Solid State Phys.*, vol. 6, no. 7, pp. 1181–1203, 1973.

[26] D. J. Thouless, M. Kohmoto, M. P. Nightingale, and M. Den Nijs, “Quantized hall conductance in a two-Dimensional periodic potential,” *Phys. Rev. Lett.*, vol. 49, no. 6, pp. 405–408, 1982.

[27] E. Gibney and D. Castelvecchi, “Noel for 2D Exotic Matter,” *Nature*, vol. 538, no. 7623, p. 18, 2016.

[28] Mermin and Ashcroft, *Solid State Physics*. 1976.

[29] L. Fu, C. L. Kane, and E. J. Mele, “Topological Insulators in Three Dimensions,” vol. 106803, no. March, pp. 1–4, 2006.

[30] M. Sprinkle, D. Siegel, Y. Hu, J. Hicks, A. Tejeda, A. Taleb-Ibrahimi, P. Le Fèvre, F. Bertran, S. Vizzini, H. Enriquez, S. Chiang, P. Soukiassian, C. Berger, W. A. De Heer, A. Lanzara, and E. H. Conrad, “First direct observation of a nearly ideal graphene band structure,” *Phys. Rev. Lett.*, vol. 103, no. 22, pp. 1–4, 2009.

[31] H. Zhang, C.-X. Liu, X.-L. Qi, X. Dai, Z. Fang, and S.-C. Zhang, “Topological insulators in Bi2Se3, Bi2Te3 and Sb2Te3 with a single Dirac cone on the surface,” *Nat. Phys.*, vol. 5, no. 6, pp. 438–442, 2009.

[32] K. Gottfried and T.-M. Yan, *Quantum Mechanics: Fundementals*, Second edi. 2003.

[33] M. Brahlek, N. Koirala, N. Bansal, and S. Oh, “Transport properties of topological insulators: Band bending, bulk metal-to-insulator transition, and weak anti-localization,”

Solid State Commun., vol. 215–216, no. 1, pp. 54–62, 2015.

[34] B. A. Bernevig, T. L. Hughes, and S. Zhang, "Quantum Spin Hall Effect and Topological Phase Transition in HgTe Quantum Wells," vol. 322, no. DECEMBER, pp. 1845–1848, 2008.

[35] M. König, S. Wiedmann, C. Brüne, A. Roth, H. Buhmann, L. W. Molenkamp, X. Qi, and S. Zhang, "Quantum Spin Hall Insulator State in HgTe Quantum Wells," *Science (80-.).*, vol. 318, no. November, pp. 766–771, 2007.

[36] D. Hsieh, D. Qian, L. Wray, Y. Xia, Y. S. Hor, R. J. Cava, and M. Z. Hasan, "A topological Dirac insulator in a quantum spin Hall phase," *Nature*, vol. 452, no. 7190, pp. 970–974, 2008.

[37] J. C. Y. Teo, L. Fu, and C. L. Kane, "Surface States of the Topological Insulator Bi_{1-x}Sb_x," pp. 1–15, 2008.

[38] D. Hsieh, Y. Xia, D. Qian, L. Wray, J. H. Dil, F. Meier, J. Osterwalder, L. Patthey, J. G. Checkelsky, N. P. Ong, A. V. Fedorov, H. Lin, A. Bansil, D. Grauer, Y. S. Hor, R. J. Cava, and M. Z. Hasan, "A tunable topological insulator in the spin helical Dirac transport regime," *Nature*, vol. 460, no. 7259, pp. 1101–1105, 2009.

[39] N. Koirala, M. Brahlek, M. Salehi, L. Wu, J. Dai, J. Waugh, T. Nummy, M. G. Han, J. Moon, Y. Zhu, D. Dessau, W. Wu, N. P. Armitage, and S. Oh, "Record Surface State Mobility and Quantum Hall Effect in Topological Insulator Thin Films via Interface Engineering," *Nano Lett.*, vol. 15, no. 12, pp. 8245–8249, 2015.

[40] N. Bansal, Y. S. Kim, E. Edrey, M. Brahlek, Y. Horibe, K. Iida, M. Tanimura, G. H. Li, T. Feng, H. D. Lee, T. Gustafsson, E. Andrei, and S. Oh, "Epitaxial growth of topological insulator Bi2Se3film on Si(111) with atomically sharp interface," *Thin Solid Films*, vol. 520, no. 1, pp. 224–229, 2011.

[41] H. D. Li, Z. Y. Wang, X. Kan, X. Guo, H. T. He, Z. Wang, J. N. Wang, T. L. Wong, N. Wang, and M. H. Xie, "The van der Waals epitaxy of Bi2Se3on the vicinal Si(111) surface: An approach for preparing high-quality thin films of a topological insulator," *New*

J. Phys., vol. 12, no. 111, pp. 0–11, 2010.

[42] N. Bansal, Y. S. Kim, M. Brahlek, E. Edrey, and S. Oh, "Thickness-independent transport channels in topological insulator Bi 2Se 3 thin films," *Phys. Rev. Lett.*, vol. 109, no. 11, pp. 1–5, 2012.

[43] G. Eilenberger, "Transformation of Gorkov's equation for type II superconductors into transport-like equations," *Zeitschrift für Phys.*, vol. 214, no. 2, pp. 195–213, 1968.

[44] K. D. Usadel, "Generalized diffusion equation for superconducting alloys," *Phys. Rev. Lett.*, vol. 25, no. 8, pp. 507–509, 1970.

[45] G. E. Blonder, M. Tinkham, and T. M. Klapwijk, "Transition from metallic to tunneling regimes in superconducting microconstrictions," no. April, 1982.

[46] A. D. K. Finck, C. Kurter, Y. S. Hor, and D. J. Van Harlingen, "Phase coherence and andreev reflection in topological insulator devices," *Phys. Rev. X*, vol. 4, no. 4, pp. 1–9, 2014.

[47] A. Brinkman and A. A. Golubov, "Crossed Andreev reflection in diffusive contacts: Quasiclassical Keldysh-Usadel formalism," *Phys. Rev. B - Condens. Matter Mater. Phys.*, vol. 74, no. 21, pp. 1–5, 2006.

[48] M. P. Stehno, "Investigations of Nonlocal Transport and Current Noise in," 2012.

[49] P. Cadden-Zimansky and V. Chandrasekhar, "Nonlocal correlations in normal-metal superconducting systems," *Phys. Rev. Lett.*, vol. 97, no. 23, pp. 1–4, 2006.

[50] M. J. Wolf, F. Hübler, S. Kolenda, H. V. Löhneysen, and D. Beckmann, "Spin injection from a normal metal into a mesoscopic superconductor," *Phys. Rev. B - Condens. Matter Mater. Phys.*, vol. 87, no. 2, pp. 1–7, 2013.

[51] C. H. L. Quay, D. Chevallier, C. Bena, and M. Aprili, "Spin imbalance and spin-charge separation in a mesoscopic superconductor," *Nat. Phys.*, vol. 9, no. 2, pp. 84–88, 2013.

[52] S. Kolenda, M. J. Wolf, D. S. Golubev, A. D. Zaikin, and D. Beckmann, "Nonlocal

transport and heating in superconductors under dual-bias conditions," *Phys. Rev. B - Condens. Matter Mater. Phys.*, vol. 88, no. 17, pp. 1–9, 2013.

[53] B. Josephson, "Supercurrents through barriers," *Adv. Phys.*, no. June 2013, pp. 37–41, 1965.

[54] M. Veldhorst, M. Snelder, M. Hoek, T. Gang, V. K. Guduru, X. L. Wang, U. Zeitler, W. G. van der Wiel, a a Golubov, H. Hilgenkamp, and a Brinkman, "Josephson supercurrent through a topological insulator surface state.," *Nat. Mater.*, vol. 11, no. 5, pp. 417–21, May 2012.

[55] C. D. Nugroho, V. Orlyanchik, and D. J. Van Harlingen, "Low frequency resistance and critical current fluctuations in Al-based Josephson junctions," *Appl. Phys. Lett.*, vol. 102, no. 14, p. 142602, 2013.

[56] D. M. Badiane, L. I. Glazman, M. Houzet, and J. S. Meyer, "Ac Josephson effect in topological Josephson junctions," *Comptes Rendus Phys.*, vol. 14, no. 9–10, pp. 840–856, Nov. 2013.

[57] Barone, "Physics and applications of the Josephson effect," *Nuovo Cim. D*, 1984.

[58] D. A. Wollman, D. J. Van Harlingen, W. C. Lee, D. M. Ginsberg, and A. J. Leggett, "Experimental Determination of Supercondcuting Pairing State in YBCO from Phase Coherence of YBCO0PB dc Squids," *PRL*, vol. 71, no. 13, pp. 2134–2137, 1993.

[59] D. Wollman and D. Van Harlingen, "Evidence for d . y. Pairing from the Magnetic Field Modulation of YBa2Cu307-Pb Josephson Junctions," *Phys. Rev. ...*, vol. 74, no. 5, pp. 797–801, 1995.

[60] J. D. Strand, "Determining the superconducting order parameter of UPt3 with Josephson junction interferometry," 2010.

[61] Y. Maeno, T. M. Rice, and M. Sigrist, "The Intriguing Superconductivity of Strontium Ruthenate," *Phys. Today*, vol. 54, no. 1, pp. 42–47, 2001.

[62] P. Björnsson, Y. Maeno, M. Huber, and K. Moler, “Scanning magnetic imaging of Sr2RuO4,” *Phys. Rev. B*, vol. 72, no. 1, pp. 1–4, Jul. 2005.

[63] J. Jang, D. G. Ferguson, V. Vakaryuk, R. Budakian, S. B. Chung, P. M. Goldbart, and Y. Maeno, “Observation of half-height magnetization steps in Sr2RuO4.,” *Science*, vol. 331, no. 6014, pp. 186–8, Jan. 2011.

[64] J. Strand, D. Van Harlingen, J. Kycia, and W. Halperin, “Evidence for Complex Superconducting Order Parameter Symmetry in the Low-Temperature Phase of UPt3 from Josephson Interferometry,” *Phys. Rev. Lett.*, vol. 103, no. 19, p. 197002, Nov. 2009.

[65] J. Clarke and A. I. Braginski, *The SQUID Handbook*, vol. 1. 2005.

[66] R. Lo Frano, D. Aquaro, and N. Olivi, “Characterization of the thermal conductivity for ceramic pebble beds,” 2015, no. November.

[67] M. Samanta, K. Pal, P. Pal, U. V Waghmare, and K. Biswas, “Localized Vibrations of Bi Bilayer Leading to Ultralow Lattice Thermal Conductivity and High Thermoelectric Performance in Weak Topological Insulator n- Type BiSe,” 2018.

[68] M. J. Assael, S. Botsios, K. Gialou, and I. N. Metaxa, “Thermal Conductivity of Polymethyl Methacrylate (PMMA) and Borosilicate Crown Glass BK7,” vol. 26, no. 5, 2005.

[69] P. A. Lee, A. D. Stone, and H. Fukuyama, “Universal conductance fluctuations in metals: Effects of finite temperature, interactions, and magnetic field,” *Phys. Rev. B*, vol. 35, no. 3, pp. 1039–1070, 1987.

[70] P. Zareapour, A. Hayat, S. Y. F. Zhao, M. Kreshchuk, A. Jain, D. C. Kwok, N. Lee, S.-W. Cheong, Z. Xu, A. Yang, G. D. Gu, S. Jia, R. J. Cava, and K. S. Burch, “Proximity-induced high-temperature superconductivity in the topological insulators Bi_2Se_3 and Bi_2Te_3.,” *Nat. Commun.*, vol. 3, p. 1056, Jan. 2012.

[71] P. Raychaudhuri, D. Jaiswal-Nagar, G. Sheet, S. Ramakrishnan, and H. Takeya, “Evidence of gap anisotropy in superconducting YNi2B2C using directional point-contact

spectroscopy," *Phys. Rev. Lett.*, vol. 93, no. 15, pp. 1–4, 2004.

[72] S. Kashiwaya and Y. Tanaka, "Tunnelling effects on surface bound states in unconventional superconductors Tunnelling effects on surface bound states in unconventional," 2000.

[73] S. Nadj-Perge, I. K. Drozdov, J. Li, H. Chen, S. Jeon, J. Seo, A. H. MacDonald, B. A. Bernevig, and A. Yazdani, "Topological matter. Observation of Majorana fermions in ferromagnetic atomic chains on a superconductor.," *Science*, vol. 346, no. 6209, pp. 602–7, 2014.

[74] V. Mourik, K. Zuo, S. M. Frolov, S. R. Plissard, E. P. a. M. Bakkers, and L. P. Kouwenhoven, "Signatures of Majorana Fermions in," *Science (80-.).*, vol. 336, no. 6084, p. 1003, 2012.

A.Josephson Junction Simulations

A.1 Simulation Explanation and Applications

In this work, it became necessary to test my understanding of the physics we thought was at play and how that would, or would not, show itself in the data. Building a computational model that I could play with provided an important avenue to test my understanding of conventional Josephson physics. It was also necessary to inform device design in the experimental process to better tease out the nature of the new physics we were looking for. In its most basic form, the simulation breaks the junction up into many localized junctions that each have a local phase difference of the superconducting order parameter and maximizes the total supercurrent with respect to an arbitrary phase factor at a single point in the junction. New physics is added by changing what influences the supercurrent. This approach most importantly assumes that the junction critical current depends exponentially on distance. A second important assumption that the simulation makes is that the flux generated by a circulating supercurrent is small so that the self-field effects can be ignored. The work here builds on simulations that were written in the Van Harlingen group and used to understand Josephson behavior in unconventional superconducting systems[1]–[4]. This serves as a detailed introduction to the model and builds to the crossover between single junction and SQuID physics applied in this thesis.

Using MATLAB as the programing language for the simulation was intentional for its ability to perform matrix operations quickly. The kernel of the program revolves around building a matrix and operating on that matrix to find the maximum critical current for each field before plotting it. I had experience writing code in MATLAB from previous work which lowered the barrier of entry to that language. It also is able to plot the data with highly configurable plots and at the time was provided free of charge in the university webstore. These factors provided a stage

for me to build a Josephson junction simulation up layer by layer to understand how new physics in the junctions would show itself in the data.

A.1.1 Simulation Building Blocks

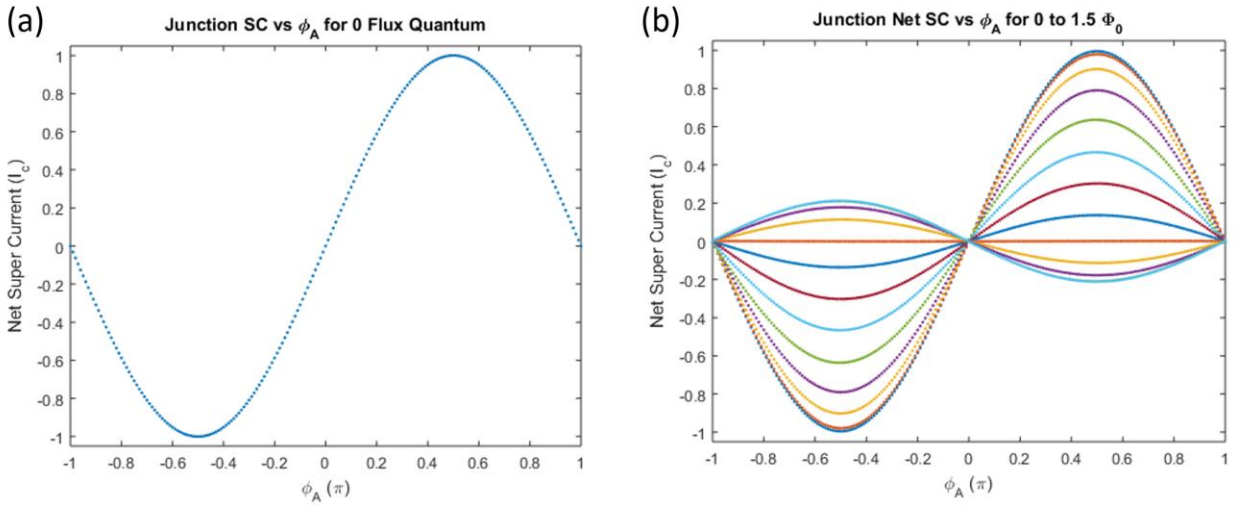

Figure A.1 The output from v00 of the simulation (a) shows the net supercurrent for the junction as a function of the arbitrary phase ϕ_A. This version can be run several times with different fields as show in (b) to see the effect of a magnetic field on the critical current of the junction. Note that the maximum critical current occurs at a ϕ_A value of $\pi/2$ from 0 to 1 flux quantum in the junction before switching to $-\pi/2$.

At the core of the simulation is a matrix of local supercurrents that together show the behavior of the junction with the included phenomena. Each row in the matrix corresponds to a position along the junction, *x*, while each column corresponds to each entry of the arbitrary phase value, ϕ_A, that is varied to maximize the supercurrent. The position and arbitrary phase dependent supercurrent is

$$I_S(x, \phi_A) = I_C(x)\, sin(\phi_A + \sum \nabla\phi\,(x)\Delta x) \tag{1}$$

where I_c is a vector of the position dependent critical current densities and the phase at each point depends on the arbitrary phase, ϕ_A. The sum of the contributions to the phase gradient along the junction contributes to the local phase drop across each section of the junction. With I_s calculated,

the total critical current for each value of ϕ_A is calculated by summing columns together to integrate along the junction width. Maximization and minimization of the critical current are completed by identifying the maximum and minimum total critical current respectively. Depending on what new physics is being investigated, variables other than the maximum critical current can be recorded. For understanding the abstract behavior of the phase of the superconducting order parameter, the value of ϕ_A, the local phase drop as a function of position, and the local supercurrent as a function of position are useful to save and plot. This level of the simulation captures the Josephson physics[5] of a single critical current measurement and is the foundation for understanding more complex junction behavior.

A.1.2 Simulations of Single Junction Physics

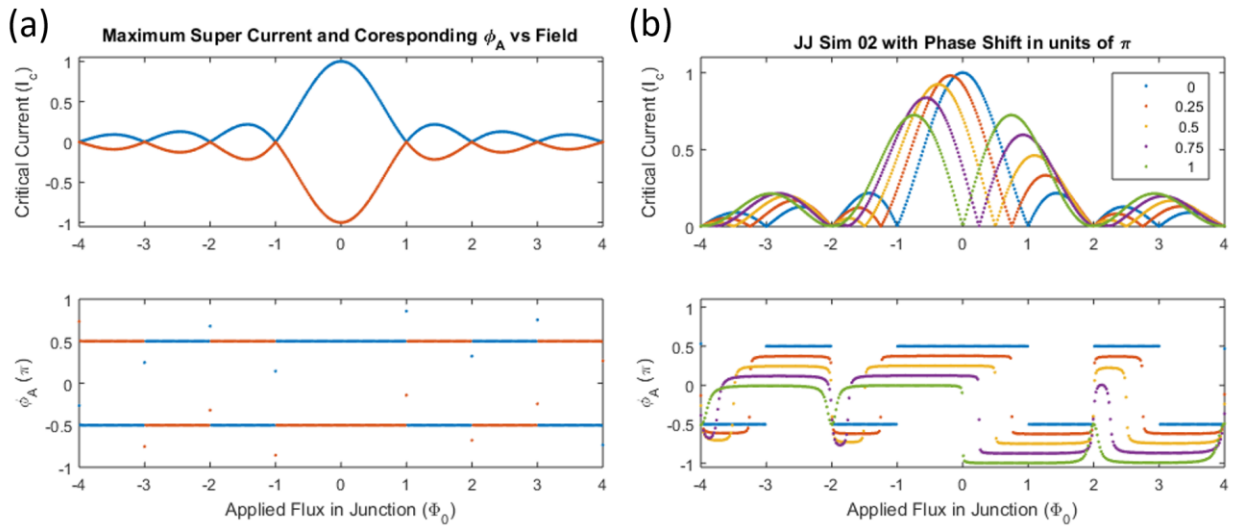

Figure A.2 The magnetic field dependence of the critical current and central phase difference in a Josephson junction are shown in (a) as simulated with v01. Ic decays with field up to 1 magnetic flux quantum in the junction before rising again. The central phase of the maximum critical current is constant at $\pi/2$ up to a single flux quantum in the junction before switching to $-\pi/2$. Some unconventional superconductors have momentum dependent phase shifts due to the symmetry of their superconducting order parameter. Simulations (b) of junctions with an intrinsic phase shift between 0 and π show a broken symmetry, but remain symmetric for shifts of 0 and π. The legend shows the current phase relationship phase shift in units of π.

With the ability to simulate a single critical current measurement established, additional physics is then added to the simulation starting with an applied magnetic field. Due to the coupling of the charged cooper pairs to the vector potential, the magnetic field adds a constant phase gradient to the junction[5], [6]. This phase gradient causes a position dependent phase drop across the junction which in turn suppresses the net critical current. The net critical current drops from 1 at no field to 0 with 1 flux quantum in the junction before increasing again with ϕ_A now at $-\pi/2$ rather than $\pi/2$. With the addition of field, the simulation captures the magnetic field dependence of the critical current shown in figure 8.2a. This provides an apples to apples comparison of numerical results with data from experiments probing exotic physics using the Josephson effect.

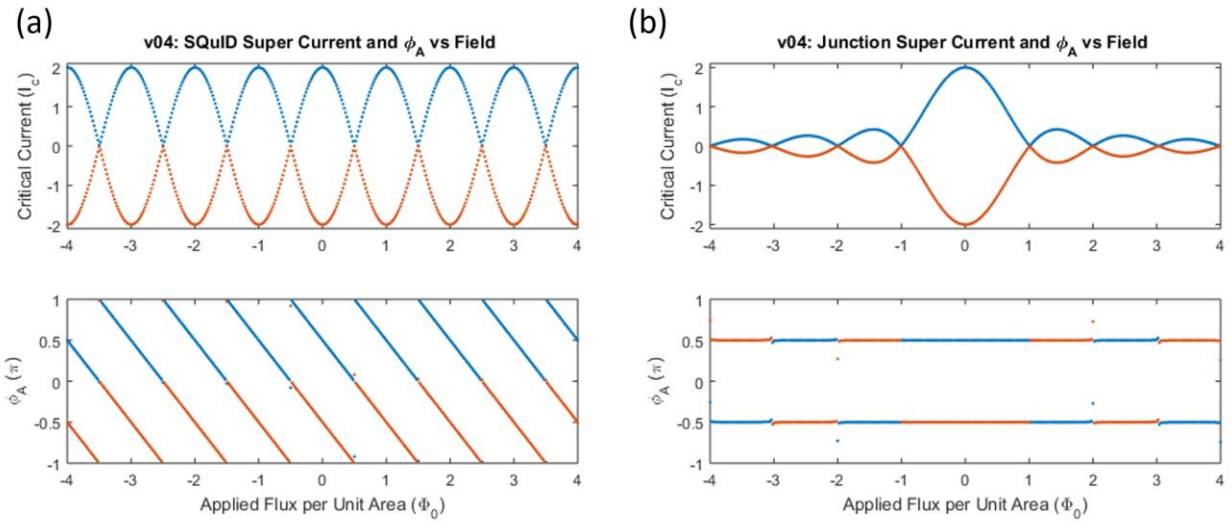

Figure A.3 The output from v04 shows the ability to simulate SQuID (a) and single Josephson junction physics (b). SQuID behavior is simulated by making the SQuID area 1 and the junction areas much smaller than 1. To simulate single junction physics, set the SQuID loop area equal to 0, and set the two halves of the device to areas of 0.5.

A classic example of probing exotic physics with Josephson physics is the demonstration of a d-wave order parameter symmetry in copper oxide superconductors[3]. Using junctions that span a 90-degree corner, Wollman et. al. demonstrated[7] that there is a phase shift of π between the two lobes of the superconducting order parameter in YBCO. We can simulate the physics in

these junctions by adding another loop to vary the strength of the new physics being studied, in this case the intrinsic phase shift of the superconductor. The phase gradient, $\nabla\phi(x)$, has a delta function at the corner, causing there to be an added phase shift of π between the two halves of the junction. In Figure A.2b, the field dependence of the critical current is plotted for 5 intrinsic phase shifts between 0 and π. For zero phase shift, the junction is symmetric with a critical current maximum at zero field. In the case of a π phase shift, the field dependence is still symmetric, but the zero-field critical current is a minimum. These results are consistent with Josephson interferometry experiments outline in the main text of this thesis.

A.1.3 Simulations of SQuID and Single Junction Physics

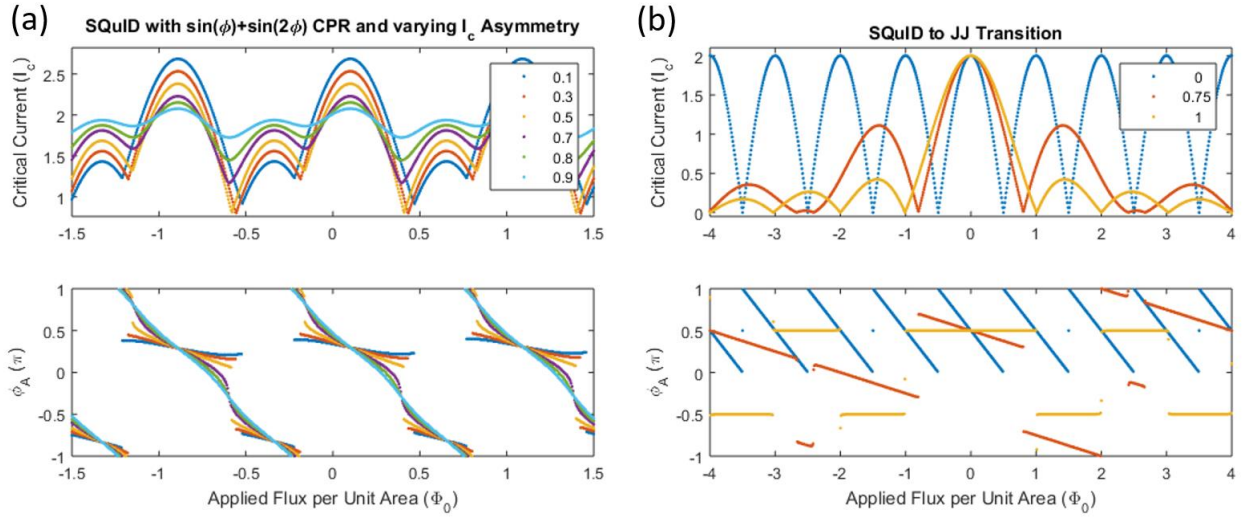

Figure A.4 Calculating the asymmetry needed to measure the current phase relationship in an asymmetric squid with $\sin(\phi)$ and $(Gpar)\sin(2\phi)$ terms in the current phase relationship. The asymmetry is characterized by $I_{C1}(Gpar) = (1 - Gpar)I_{C1}$ and $I_{C2}(Gpar) = (1 + Gpar)I_{C2}$ where *Gpar* is the parameter shown in the legend. For the research in this thesis, the cross over regime in areas from purely SQuID physics to purely single junction physics shows a change in the location of the node of the junction. These results are from v05 of the simulation included below.

With a single junction simulation in place, we can use it as a building block to simulate a superconducting quantum interference device, or SQuID. To do this, the building block simulation is doubled to account for the second junction. Instead of an arbitrary phase for the second junction,

the phase at the edge will be determined by combining the local phase drop at the edge of the first junction with a field dependent discontinuity. This phase step corresponds to the flux threading the SQuID loop that the two junctions form. Adding this layer of complexity enables the simulation of Josephson junction physics and SQuID physics with the same code as shown Figure A.3. Checking the limiting behavior of the simulation in each of the cases provides evidence that both SQuID and single junction physics are handled correctly in the simulation. The crossover regime shown in Figure A.4b is discussed in more detail in the text.

An application of SQuIDs that has recently re-emerged with fruitful results is the measurement of the current phase relationship of an exotic junction with an asymmetric squid[8]. When both junctions have equal maximum critical currents, the maximization takes the phase across each one into account equally. This leads to a discontinuity in the phase winding at half a flux quantum in the squid loop where circulating currents start adding field to the loop rather than screening it out. When one junction has a larger critical current than the other one, it will be weighted more heavily in the maximization. As this goes to the extreme, one junction will stay at $\pi/2$ phase difference, and the flux threading the loop will wind the phase in the other junction. The magnetic field dependence of the device critical current will then match the current phase relationship of the smaller junction with a periodicity determined by the SQuID loop area. From simulating different junction asymmetries, a critical current ratio of 1:10 balances the modulation amplitude with removal of distortion from phase discontinuities due to flux quantization. An example of a SQuID with varying amounts of asymmetry is shown in Figure A.4**Error! Reference source not found.**a. The smaller critical current junction includes both a $\sin(\phi)$ term and a $\sin(2\phi)$ term in the current phase relationship.

A.1.4 Adding SI Units to the Simulation

For the research in this thesis, the region of interest is when the SQuID and Junction areas are of comparable size. A simulation of this regime is shown in **Error! Reference source not found.**, with a more in-depth discussion of relevant physics in the main body of the thesis. The main result is that the apparent area of the junction as determined by the node position can be influenced by the competition between SQuID and single junction physics. The last step in the development of the simulation is to change the units to reflect values that are measured in lab. Lengths are measured in μm, magnetic fields in mT, and currents in μA. This enables direct simulation of actual junctions by measuring the dimensions with an atomic force microscope or a scanning electron microscope. This is accomplished by dividing the applied field by a factor [5] of 2.06 mT μm^2. This results in units outlined in Table A1 below.

Measurement	Units	Symbol
Length	micro meters	μm
Area	micro meters squared	μm^2
Magnetic field	milli Tesla	mT
Current	Micro Amperes	μA
Phase	radians	unitless

Table A.1 Units of various parameters in the simulation v07 with SI units. The conversion to SI units is done by dividing the applied field by 2.06 mT μm^2 and entering all other parameters in units listed here.

This simulation provided an important tool for developing and testing possible physical explanations for the behavior of the junctions in this work. A more in-depth discussion of its direct application to the work in this thesis can be found in the main text. Building a numerical model of our devices also provided me an opportunity to test my own understanding of Josephson

physics. In writing the model, I also learned the details of other uses of the Josephson effect to investigate exotic physics in superconducting systems. My hope is that this tool will continue to be useful for graduate students using the Josephson effect to study exotic superconducting systems.

A.2 Single Junction Simulations: JJSimV_00 – JJSimV02

A.2.1 JJSimV00_JusttheBasics.m

```
%% JJSimV00_JusttheBasics.m
% written by Erik Huemiller

% The Goal of this version of the program is to show the kernel of the
% more complex Josephson junction simulation programs.

%% Clearing memory and input screen.
clear; clc; close all;
%% Defining the Parameters of the Simulaiton
   %Dividing the junction up into discrete sections
      xmin = -51;
      xmax =  51;
      xsize=xmax-xmin+1;
      x(1:xsize,1) = (1:xsize)-1+xmin;
      xnorm = x/xsize;

   %Super Current parameters
      SCurrentMag = 1;
      SCurrentNoiseMag =.01;
      SCurrentNoise = (SCurrentNoiseMag*(2*rand(xsize,1)-1));

%Setting up Sweep Parameters
   %Phase Vector Generation
      psize=201;
      PhaseA_min=-1*pi;
      PhaseA_max=1*pi;
      PhaseA = PhaseA_min:(PhaseA_max-PhaseA_min)/(psize-1):PhaseA_max;

   %Flux Encolsed in the Junction
      FluxinJunc=0/2;

%Calculating Parameters from Initial Conditions
   SCurrentDensity=(SCurrentMag*ones(xsize,1)+SCurrentNoise)*ones(1,psize)/xsize;

%% Main Body of Simulation
%Calcuating Field Contributions to the Phase Drop
```

```
PhaseF = 2*pi*FluxinJunc*xnorm; % vector in units of radians

%Combining Phase drops to find the local drops across the junction
PhaseDrop = ones(xsize,1)*PhaseA+PhaseF*ones(1,psize);

%Calculating the matrix that is the Super Current (SCurrent)across
%the junction at each position for each value of PhaseA.
SCurrentLoc = SCurrentDensity.*sin(PhaseDrop);

%Numerically integrating the Super Current (SCurrentLoc) along the
%junction at each PhaseA to find the total super current carried.
SCurrentNet = sum(SCurrentLoc);

%% Plotting the outputs
%Plot the SCurrentNet vs the Phase1 value for the Junction
%figure;
hold on;
   plot(PhaseA/pi,SCurrentNet,'.');
   xlabel ('\phi_A (\pi)');ylabel('Net Super Current (I_c)');
   ylim([-1.05*SCurrentMag 1.05*SCurrentMag]);
   box on;

% Making the title for the plot
   BField = num2str(FluxinJunc);
   title(strcat(['Junction SC vs \phi_A for ' BField ' Flux Quantum']));
```

A.2.2 A.2.1 JJSimV01_SimplestJunctionSim.m

```
%% JJSimV01_SimplestJunctionSim.m
 % written by Erik Huemiller

 % The goal of this version of the program is to add a flux loop and
 % critical current maximization to v00.  This enables us to compare it to
 % something we measure in lab, the critical current.

%% Clearing memory and input screen.
clear; clc; close all;

%% Defining the Parameters of the Simulaiton
   %Dividing the junction up into discrete sections
      xmin = -51;
      xmax =  51;
      xsize=xmax-xmin+1;
      x(1:xsize,1) = (1:xsize)-1+xmin;
      xnorm = x/xsize;
   %Defining Super Current parameters
      SCurrentMag =1;
```

```
    SCurrentNoiseMag =.001;
  SCurrentNoise = (SCurrentNoiseMag/xsize*(2*rand(xsize,1,1)-1));

%Setting up Sweep Parameters
  %Phase Vector Generation, will be the column (2nd index)
    psize=505;
    PhaseA_min = -1.0 * pi;
    PhaseA_max =  1.0 * pi;
    PhaseA_SS = (PhaseA_max-PhaseA_min)/(psize-1);
    PhaseA = PhaseA_min:PhaseA_SS:PhaseA_max;% vector (radians)
  %Flux Vector Generation, will be the 'f' for loop
    fsize=401; f=1;
    FluxinJunc_min= -4;
    FluxinJunc_max=  4 ;
    FluxinJunc_SS = (FluxinJunc_max-FluxinJunc_min)/(fsize-1);
    FluxinJunc(1,:) = FluxinJunc_min:FluxinJunc_SS:FluxinJunc_max;
    PhaseF=2*pi*xnorm*FluxinJunc; % vector in units of radians

%Calculating Parameters from Initial Conditions
  SCurrentDensity = (SCurrentMag/xsize*ones(xsize,1)+SCurrentNoise);

%Pre Allocating memory for the arrays to decrease runtime
  % for maximum critical current
  SCurrentNet_max = zeros(1,fsize);
  Index_max=zeros(1,fsize);
  PhaseA_maxSC=zeros(1,fsize);
  PhaseDrop_maxSC = zeros(xsize,fsize);
  SCurrentLoc_maxSC = zeros(xsize,fsize);

  % for minimum critical current
  SCurrentNet_min = zeros(1,fsize);
  Index_min=zeros(1,fsize);
  PhaseA_minSC=zeros(1,fsize);
  PhaseDrop_minSC = zeros(xsize,fsize);
  SCurrentLoc_minSC = zeros(xsize,fsize);

%% Main Body of the Simulation
 for f=1:fsize
  %Combining Phase drops to find the local drops across the junction
  PhaseDrop=ones(xsize,1)*PhaseA+PhaseF(:,f)*ones(1,psize);

  %Calculating the matrix that is the Super Current (SCurrentLoc) across
  %the junction at each position for each value of PhaseA.
  SCurrentLoc=SCurrentDensity*ones(1,psize).*sin(PhaseDrop);

  %Numerically integrating the Super Current (SCurrentLoc) along the
```

```
    %junction at each PhaseA to find the total super current carried.
    SCurrentNet=sum(SCurrentLoc); %sums along x to get a row

    %Finding the Magnitude and the Index of the maximum
    %supercurrent across the junction at the current field strength
    [SCurrentNet_max(f),Index_max(f)]=max(SCurrentNet);

    %Recording the interesting values when the current is maximized
    PhaseA_maxSC(1,f) = PhaseA(1,Index_max(f)); % vector (radians)
    PhaseDrop_maxSC (:,f) = PhaseDrop(:,Index_max(f));
    SCurrentLoc_maxSC (:,f) = SCurrentLoc(:,Index_max(f));


    %Finding the Magnitude and the Index of the minimum
    %supercurrent across the junction at the current field strength
    [SCurrentNet_min(f),Index_min(f)]=min(SCurrentNet);

    %Recording the interesting values when the current is minimized
    PhaseA_minSC(1,f) = PhaseA(1,Index_min(f)); % vector (radians)
    PhaseDrop_minSC (:,f) = PhaseDrop(:,Index_min(f));
    SCurrentLoc_minSC (:,f) = SCurrentLoc(:,Index_min(f));
 end

%Ploting the maximum supercurrent vs the field in the junction
figure; subplot(2,1,1);
    plot(FluxinJunc,SCurrentNet_max,'.'); hold on;
    plot(FluxinJunc,SCurrentNet_min,'.');
    ylabel('Critical Current (I_c)'); ylim([-1.05*SCurrentMag 1.05*SCurrentMag]);
    title('Maximum Super Current and Coresponding \phi_A vs Field')

%Ploting the PhaseA value that maximizes the critical current
subplot(2,1,2); hold on;
    plot(FluxinJunc,PhaseA_maxSC/pi,'.');
    plot(FluxinJunc,PhaseA_minSC/pi,'.');
    xlabel('Applied Flux in Junction (\Phi_0)');
    ylabel('\phi_A (\pi)'); ylim([PhaseA_min/pi PhaseA_max/pi]);
    box on;
```

A.2.3 JJSimV02_SingleJunctionBaseSim.m

```
%% JJSimV02_SingleJunctionBaseSim.m
 % written by Erik Huemiller

 % The goal of this version of the program is to take JJSimV01 and add a
 % loop that varies the strength exotic physics.

 % This version is set up to provide a prototyping bed, so the exotic
```

```
 % physics is yours to include

%% Clearing memory and input screen.
clear; clc; close all;
%% Defining the Parameters of the Simulaiton
   %Dividing the junction up into discrete sections
      xmin = -100;
      xmax =  100;
      xsize=xmax-xmin+1;
      x(1:xsize,1) = (1:xsize)-1+xmin;
      xnorm = x/xsize;
   %Defining Super Current parameters
      SCurrentMag = 1;
      SCurrentNoiseMag = 0.01;
    SCurrentNoise = (SCurrentNoiseMag/xsize*(2*rand(xsize,1,1)-1));

%Setting up Sweep Parameters
   %Phase Vector Generation, will be the column (2nd index)
      psize=301;
      PhaseA_min = -2.0 * pi;
      PhaseA_max =  2.0 * pi;
      PhaseA_SS = (PhaseA_max-PhaseA_min)/(psize-1);
      PhaseA = PhaseA_min:PhaseA_SS:PhaseA_max;% vector (radians)

   %Flux Vector Generation, will be the 'f' loop
      fsize = 601; f=1;
      FluxinJunc_min = -3;
      FluxinJunc_max =  3 ;
      FluxinJunc_SS = (FluxinJunc_max-FluxinJunc_min) / (fsize-1);
      FluxinJunc(1,:) = FluxinJunc_min:FluxinJunc_SS:FluxinJunc_max;
      PhaseF = 2*pi * xnorm * FluxinJunc; % vector in units of radians

   %Iteration Vector Generation, will be the 'g' parameter loop
      gsize=2; g=1;
      Gpar_min = 0;
      Gpar_max =  1 ;
      Gpar_SS = (Gpar_max-Gpar_min) / (gsize-1);
      Gpar(1,:) = Gpar_min:Gpar_SS:Gpar_max;

%Calculating Parameters from Initial Conditions
   SCurrentDensity = (SCurrentMag/xsize*ones(xsize,1)+SCurrentNoise);

%Pre Allocating memory for the arrays to decrease runtime
   % for maximum critical current
   SCurrentNet_max = zeros(1,fsize,gsize);
   Index_max = zeros(1,fsize,gsize);
```

```
    PhaseA_maxSC = zeros(1,fsize,gsize);
    PhaseDrop_maxSC = zeros(xsize,fsize,gsize);
    SCurrentLoc_maxSC = zeros(xsize,fsize,gsize);

    % for minimum critical current
    SCurrentNet_min = zeros(1,fsize,gsize);
    Index_min=zeros(1,fsize,gsize);
    PhaseA_minSC=zeros(1,fsize,gsize);
    PhaseDrop_minSC = zeros(xsize,fsize,gsize);
    SCurrentLoc_minSC = zeros(xsize,fsize,gsize);

%% Main Body of the Simulation
for g = 1: gsize
     for f=1:fsize

        %Combining Phase drops to find the local drops across the junction
        PhaseDrop = ones(xsize,1)*PhaseA+PhaseF(:,f)*ones(1,psize);

        %Calculating the matrix that is the Super Current (SCurrentLoc) across
        %the junction at each position for each value of PhaseA.
        SCurrentLoc = SCurrentDensity*ones(1,psize).*sin(PhaseDrop);

        %Numerically integrating the Super Current (SCurrentLoc) along the
        %junction at each PhaseA to find the total super current carried.
        SCurrentNet = sum(SCurrentLoc); %sums along x to get a row

        %Finding the Magnitude and the Index of the maximum
        %supercurrent across the junction at the current field strength
        [SCurrentNet_max(1,f,g),Index_max(f,g)] = max(SCurrentNet);

        %Recording the interesting values when the current is maximized
        PhaseA_maxSC(1,f,g) = PhaseA(1,Index_max(f,g)); % vector (radians)
        PhaseDrop_maxSC (:,f,g) = PhaseDrop(:,Index_max(f,g));
        SCurrentLoc_maxSC (:,f,g) = SCurrentLoc(:,Index_max(f,g));

        %Finding the Magnitude and the Index of the minimum
        %supercurrent across the junction at the current field strength
        [SCurrentNet_min(1,f,g),Index_min(f,g)] = min(SCurrentNet);

        %Recording the interesting values when the current is minimized
        PhaseA_minSC(1,f,g) = PhaseA(1,Index_min(f,g)); % vector (radians)
        PhaseDrop_minSC (:,f,g) = PhaseDrop(:,Index_min(f,g));
        SCurrentLoc_minSC (:,f,g) = SCurrentLoc(:,Index_min(f,g));
     end
end
```

```
%% Plotting Relevant Data
%Ploting the maximum supercurrent vs the field in the junction
figure; subplot(2,1,1);
   plot(FluxinJunc,squeeze(SCurrentNet_max),'.'); hold on;
   plot(FluxinJunc,squeeze(SCurrentNet_min),'.');

   ylabel('Critical Current'); ylim([-1.1*SCurrentMag 1.1*SCurrentMag]);
   title('JJ Sim 02 with Dummy Gpar Values');
   legend(num2str(transpose(chop(Gpar,3))));

%Ploting the PhaseA value that maximizes the critical current
subplot(2,1,2);
   plot(FluxinJunc,squeeze(PhaseA_maxSC)/pi,'.'); hold on;
   plot(FluxinJunc,squeeze(PhaseA_minSC)/pi,'.');
   xlabel('Flux in Junction (\Phi_0)');
   ylabel('PhaseA (\pi)'); ylim([PhaseA_min/pi PhaseA_max/pi])
```

A.2.4 JJSimV02_PhaseShift.m

```
%% JJSimV02_PhaseShift.m
 % written by Erik Huemiller

 % The goal of this version of the program is to take JJSimV01 and add a
 % loop that varies the strength exotic physics.

 % In this example, the intrinsic phase shift of the junction
 % is tuned to show what happens in corer junctions where one of the
 % superconductors has a momentum dependent phase shift.

%% Clearing memory and input screen.
clear; clc; close all;
%% Defining the Parameters of the Simulaiton
   %Dividing the junction up into discrete sections
      xmin = -100;
      xmax =  100;
      xsize=xmax-xmin+1;
      x(1:xsize,1) = (1:xsize)-1+xmin;
      xnorm = x/xsize;
   %Defining Super Current parameters
      SCurrentMag = 1;
      SCurrentNoiseMag = 0.0001;
      SCurrentNoise = (SCurrentNoiseMag/xsize*(2*rand(xsize,1,1)-1));

%Setting up Sweep Parameters
   %Phase Vector Generation, will be the column (2nd index)
      psize=501;
      PhaseA_min = -1.0 * pi;
```

```
    PhaseA_max =  1.0 * pi;
    PhaseA_SS = (PhaseA_max-PhaseA_min)/(psize-1);
    PhaseA = PhaseA_min:PhaseA_SS:PhaseA_max;% vector (radians)

  %Flux Vector Generation, will be the 'f' loop
    fsize = 400; f=1;
    FluxinJunc_min = -4;
    FluxinJunc_max =  4 ;
    FluxinJunc_SS = (FluxinJunc_max-FluxinJunc_min) / (fsize-1);
    FluxinJunc(1,:) = FluxinJunc_min:FluxinJunc_SS:FluxinJunc_max;
    PhaseF = 2*pi * xnorm * FluxinJunc; % vector in units of radians

  %Iteration Vector Generation, will be the 'g' parameter loop
    gsize = 5; g=1;
    Gpar_min = 0;
    Gpar_max =  pi ;
    Gpar_SS = (Gpar_max-Gpar_min) / (gsize-1);
    Gpar(1,:) = Gpar_min:Gpar_SS:Gpar_max;
    PhaseG = zeros(xsize,gsize);
    PhaseG(xsize + xmin:end,:) = ones(xmax + 1,1)*Gpar;

%Calculating Parameters from Initial Conditions
  SCurrentDensity = (SCurrentMag/xsize*ones(xsize,1)+SCurrentNoise);

%Pre Allocating memory for the arrays to decrease runtime
  % for maximum critical current
  SCurrentNet_max = zeros(1,fsize,gsize);
  Index_max = zeros(1,fsize,gsize);
  PhaseA_maxSC = zeros(1,fsize,gsize);
  PhaseDrop_maxSC = zeros(xsize,fsize,gsize);
  SCurrentLoc_maxSC = zeros(xsize,fsize,gsize);

  % for minimum critical current
  SCurrentNet_min = zeros(1,fsize,gsize);
  Index_min=zeros(1,fsize,gsize);
  PhaseA_minSC=zeros(1,fsize,gsize);
  PhaseDrop_minSC = zeros(xsize,fsize,gsize);
  SCurrentLoc_minSC = zeros(xsize,fsize,gsize);

%% Main Body of the Simulation
for g = 1: gsize
   for f=1:fsize
    %Combining Phase drops to find the local drops across the junction
    PhaseE = PhaseF(:,f)*ones(1,psize) + PhaseG(:,g)*ones(1,psize);
    PhaseDrop = ones(xsize,1)*PhaseA + PhaseE;
```

```
        %Calculating the matrix that is the Super Current (SCurrentLoc) across
        %the junction at each position for each value of PhaseA.
        SCurrentLoc = SCurrentDensity*ones(1,psize).*sin(PhaseDrop);

        %Numerically integrating the Super Current (SCurrentLoc) along the
        %junction at each PhaseA to find the total super current carried.
        SCurrentNet = sum(SCurrentLoc); %sums along x to get a row


        %Finding the Magnitude and the Index of the maximum
        %supercurrent across the junction at the current field strength
        [SCurrentNet_max(1,f,g),Index_max(f,g)] = max(SCurrentNet);

        %Recording the interesting values when the current is maximized
        PhaseA_maxSC(1,f,g) = PhaseA(1,Index_max(f,g)); % vector (radians)
        PhaseDrop_maxSC (:,f,g) = PhaseDrop(:,Index_max(f,g));
        SCurrentLoc_maxSC (:,f,g) = SCurrentLoc(:,Index_max(f,g));

        %Finding the Magnitude and the Index of the minimum
        %supercurrent across the junction at the current field strength
        [SCurrentNet_min(1,f,g),Index_min(f,g)] = min(SCurrentNet);

        %Recording the interesting values when the current is minimized
        PhaseA_minSC(1,f,g) = PhaseA(1,Index_min(f,g)); % vector (radians)
        PhaseDrop_minSC (:,f,g) = PhaseDrop(:,Index_min(f,g));
        SCurrentLoc_minSC (:,f,g) = SCurrentLoc(:,Index_min(f,g));
    end
end
%% Plotting Relevant Data
%Ploting the maximum supercurrent vs the field in the junction
figure; subplot(2,1,1);
   plot(FluxinJunc,squeeze(SCurrentNet_max),'.'); hold on;
   %plot(FluxinJunc,squeeze(SCurrentNet_min),'.');

   ylabel('Critical Current (I_c)');
   ylim([0 1.1*SCurrentMag]);%ylim([-1.1*SCurrentMag 1.1*SCurrentMag]);
   title('JJ Sim 02 with Phase Shift in units of \pi');
   legend(num2str(transpose(chop(Gpar/pi,3))));

%Ploting the PhaseA value that maximizes the critical current
subplot(2,1,2);
   plot(FluxinJunc,squeeze(PhaseA_maxSC)/pi,'.'); hold on;
   %plot(FluxinJunc,squeeze(PhaseA_minSC)/pi,'.');
   xlabel('Applied Flux in Junction (\Phi_0)');
   ylabel('\phi_A (\pi)'); ylim(1.05*[PhaseA_min/pi 1.05*PhaseA_max/pi]);
```

A.3 SQuID Simulations: JJSimv04 – JJ SimV05

A.3.1 JJSimV04_SimplestSQuID.m

```
%% JJSimV04_SimplestSQuID.m
 % written by Erik Huemiller

 % The goal of this version of the program is to adapt JJSimV02 to be a
 % SQuID simulation.  This involves adding a second junction and including
 % a SQuID loop dependent term to the phase in one of the junctions.

 % The base Sim version only includes the fundemental Josephson physics for
 % a SQuID.  No exotic physics is included.

%% Clearing memory and input screen.
clear; clc; close all;
%% Defining the Parameters of the Simulaiton

%Dividing the junction up into discrete sections
   % Junction 1
      x1min = -100;
      x1max =  0;
      x1_area = 0.4;
      x1size=x1max-x1min+1;
      x1(1:x1size,1) = (1:x1size)-1+x1min;
      x1norm = x1_area * x1/x1size;
   % Junction 2
      x2min = 0;
      x2max =  101;
      x2_area = 0.4;
      x2size=x2max-x2min+1;
      x2(1:x2size,1) = (1:x2size)-1+x2min;
      x2norm = x2_area * x2/x2size;

%Defining Super Current parameters
   % Junction 1
      SCurrent1Mag = 1;
      SCurrentNoise1Mag = 0.01;
      SCurrentNoise1 = (SCurrentNoise1Mag/x1size*(2*rand(x1size,1,1)-1));
   % Junction 2
      SCurrent2Mag = 1;
      SCurrentNoise2Mag = 0.01;
      SCurrentNoise2 = (SCurrentNoise2Mag/x2size*(2*rand(x2size,1,1)-1));
   % SQuID loop area
      SLarea = 1;

%Setting up Sweep Parameters
```

```
   %Phase Vector Generation, will be the column (2nd index)
      psize = 501;
      PhaseA_min = -1.0 * pi;
      PhaseA_max =  1.0 * pi;
      PhaseA_SS = (PhaseA_max-PhaseA_min)/(psize-1);
      PhaseA = PhaseA_min:PhaseA_SS:PhaseA_max;% vector (radians)

   %Flux Vector Generation, will be the 'f' loop
      fsize = 401; f=1;
      FluxinJunc_min = -4;
      FluxinJunc_max =  4 ;
      FluxinJunc_SS = (FluxinJunc_max-FluxinJunc_min) / (fsize-1);
      FluxinJunc(1,:) = FluxinJunc_min:FluxinJunc_SS:FluxinJunc_max;
       Phase1F = 2*pi * x1norm * FluxinJunc; % vector in units of radians
       Phase2F = 2*pi * x2norm * FluxinJunc; % vector in units of radians
       PhaseSF = 2*pi * ones(x2size,1)* SLarea * FluxinJunc;

%Calculating Parameters from Initial Conditions
   SCurrent1Density = (SCurrent1Mag/x1size*ones(x1size,1)+SCurrentNoise1);
   SCurrent2Density = (SCurrent2Mag/x2size*ones(x2size,1)+SCurrentNoise2);

%Pre Allocating memory for maximum critical current
      SCurrentNet_max = zeros(1,fsize);
      Index_max = zeros(1,fsize);
      PhaseA_maxSC = zeros(1,fsize);
   % Junction 1
      PhaseDrop1_maxSC = zeros(x1size,fsize);
      SCurrent1Loc_maxSC = zeros(x1size,fsize);
   % Junction 2
      PhaseDrop2_maxSC = zeros(x2size,fsize);
      SCurrent2Loc_maxSC = zeros(x2size,fsize);

%Pre Allocating memory for minimum critical current
      SCurrentNet_min = zeros(1,fsize);
      Index_min = zeros(1,fsize);
      PhaseA_minSC = zeros(1,fsize);
   % Junction 1
      PhaseDrop1_minSC = zeros(x1size,fsize);
      SCurrent1Loc_minSC = zeros(x1size,fsize);
   % Junction 2
      PhaseDrop2_minSC = zeros(x2size,fsize);
      SCurrent2Loc_minSC = zeros(x2size,fsize);

%% Main Body of the Simulation
 for f=1:fsize
   %Combining Phase drops to find the local drops across the junction
```

```
    PhaseE1 = Phase1F(:,f)*ones(1,psize);
    PhaseDrop1 = ones(x1size,1)*PhaseA+PhaseE1;

    PhaseE2 = Phase2F(:,f)*ones(1,psize)+ PhaseSF(:,f)*ones(1,psize);
    PhaseDrop2 = ones(x2size,1)*PhaseA+PhaseE2;

    %Calculating the matrix that is the current (SCurrentLoc) across
    %the junction at each position for each value of PhaseA.
    SCurrentLoc1 = SCurrent1Density*ones(1,psize).*sin(PhaseDrop1);
    SCurrentLoc2 = SCurrent2Density*ones(1,psize).*sin(PhaseDrop2);

    %Numerically integrating the Super Current (SCurrentLoc) along the
    %junction at each PhaseA to find the total super current carried.
    SCurrentNet1 = sum(SCurrentLoc1); %sums along x to get a row
    SCurrentNet2 = sum(SCurrentLoc2); %sums along x to get a row
    SCurrentNetTot = SCurrentNet1 + SCurrentNet2;

    %Finding the Magnitude and the Index of the maximum
    %supercurrent across the junction at the current field strength
    [SCurrentNet_max(1,f),Index_max(f)] = max(SCurrentNetTot);

    %Recording the interesting values when the current is maximized
    PhaseA_maxSC(1,f) = PhaseA(1,Index_max(f)); % vector (radians)

    PhaseDrop1_maxSC (:,f) = PhaseDrop1(:,Index_max(f));
    PhaseDrop2_maxSC (:,f) = PhaseDrop2(:,Index_max(f));

    SCurrent1Loc_maxSC (:,f) = SCurrentLoc1(:,Index_max(f));
    SCurrent2Loc_maxSC (:,f) = SCurrentLoc2(:,Index_max(f));

    %Finding the Magnitude and the Index of the minimum
    %supercurrent across the junction at the current field strength
    [SCurrentNet_min(1,f),Index_min(f)] = min(SCurrentNetTot);

    %Recording the interesting values when the current is minimized
    PhaseA_minSC(1,f) = PhaseA(1,Index_min(f)); % vector (radians)

    PhaseDrop1_minSC (:,f) = PhaseDrop1(:,Index_min(f));
    PhaseDrop2_minSC (:,f) = PhaseDrop2(:,Index_min(f));

    SCurrent1Loc_minSC (:,f) = SCurrentLoc1(:,Index_min(f));
    SCurrent2Loc_minSC (:,f) = SCurrentLoc2(:,Index_min(f));
  end

%% Plotting Relevant Data
%Ploting the maximum supercurrent vs the field in the junction
```

```
figure; subplot(2,1,1);
   plot(FluxinJunc,squeeze(SCurrentNet_max),'.'); hold on;
   plot(FluxinJunc,squeeze(SCurrentNet_min),'.');

   ylabel('Critical Current (I_c)');
   ylim([1.05*min(min(SCurrentNet_min)) 1.05*max(max(SCurrentNet_max))]);
   title('v04: SQuID Super Current and \phi_A vs Field ');

%Ploting the PhaseA value that maximizes the critical current
subplot(2,1,2);
   plot(FluxinJunc,squeeze(PhaseA_maxSC)/pi,'.'); hold on;
   plot(FluxinJunc,squeeze(PhaseA_minSC)/pi,'.');
   xlabel('Applied Flux per Unit Area (\Phi_0)');
   ylabel('\phi_A (\pi)'); ylim([PhaseA_min/pi PhaseA_max/pi]);
%% JJSimV05_SQuIDBaseSim.m
 % written by Erik Huemiller

 % The goal of this version of the program is to adapt JJSimV04 to be able
 % to simulate exotic physics.  This involves adding a "g" loop that
 % iterates the strength of the exotic physics.

 % The base Sim version only includes the fundemental Josephson physics for
 % a SQuID.  It includes a "g" loop, but no exotic physics is included.

%% Clearing memory and input screen.
clear; clc; close all;
%% Defining the Parameters of the Simulaiton

%Dividing the junction up into discrete sections
   % Junction 1
      x1min = -100;
      x1max =  0;
      x1_area = .01;
      x1size=x1max-x1min+1;
      x1(1:x1size,1) = (1:x1size)-1+x1min;
      x1norm = x1_area * x1/x1size;
   % Junction 2
      x2min = 0;
      x2max =  101;
      x2_area = .01;
      x2size=x2max-x2min+1;
      x2(1:x2size,1) = (1:x2size)-1+x2min;
      x2norm = x2_area * x2/x2size;

%Defining Super Current parameters
   % Junction 1
```

```
    SCurrent1Mag = 1;
    SCurrentNoise1Mag = 0.01;
    SCurrentNoise1 = (SCurrentNoise1Mag/x1size*(2*rand(x1size,1,1)-1));
  % Junction 2
    SCurrent2Mag = 1;
    SCurrentNoise2Mag = 0.01;
    SCurrentNoise2 = (SCurrentNoise2Mag/x2size*(2*rand(x2size,1,1)-1));
  % SQuID loop area
    SLarea = 1;

%Setting up Sweep Parameters
  %Phase Vector Generation, will be the column (2nd index)
    psize = 301;
    PhaseA_min = -1.0 * pi;
    PhaseA_max =  1.0 * pi;
    PhaseA_SS = (PhaseA_max-PhaseA_min)/(psize-1);
    PhaseA = PhaseA_min:PhaseA_SS:PhaseA_max;% vector (radians)

  %Flux Vector Generation, will be the 'f' loop
    fsize = 601; f=1;
    FluxinJunc_min = -3;
    FluxinJunc_max =  3 ;
    FluxinJunc_SS = (FluxinJunc_max-FluxinJunc_min) / (fsize-1);
    FluxinJunc(1,:) = FluxinJunc_min:FluxinJunc_SS:FluxinJunc_max;
    Phase1F = 2*pi * x1norm * FluxinJunc; % vector in units of radians
    Phase2F = 2*pi * x2norm * FluxinJunc; % vector in units of radians
    PhaseSF = 2*pi * ones(x2size,1)* SLarea * FluxinJunc;

  %Iteration Vector Generation, will be the 'g' parameter loop
    gsize=2; g=1;
    Gpar_min = 0;
    Gpar_max = 1 ;
    Gpar_SS = (Gpar_max-Gpar_min) / (gsize-1);
    Gpar(1,:) = Gpar_min:Gpar_SS:Gpar_max;

%Calculating Parameters from Initial Conditions
  SCurrent1Density = (SCurrent1Mag/x1size*ones(x1size,1)+SCurrentNoise1);
  SCurrent2Density = (SCurrent2Mag/x2size*ones(x2size,1)+SCurrentNoise2);

%Pre Allocating memory for maximum critical current
    SCurrentNet_max = zeros(1,fsize,gsize);
    Index_max = zeros(1,fsize,gsize);
    PhaseA_maxSC = zeros(1,fsize,gsize);
  % Junction 1
    PhaseDrop1_maxSC = zeros(x1size,fsize,gsize);
    SCurrent1Loc_maxSC = zeros(x1size,fsize,gsize);
```

```
   % Junction 2
      PhaseDrop2_maxSC = zeros(x2size,fsize,gsize);
      SCurrent2Loc_maxSC = zeros(x2size,fsize,gsize);

%Pre Allocating memory for minimum critical current
      SCurrentNet_min = zeros(1,fsize,gsize);
      Index_min = zeros(1,fsize,gsize);
      PhaseA_minSC = zeros(1,fsize,gsize);
   % Junction 1
      PhaseDrop1_minSC = zeros(x1size,fsize,gsize);
      SCurrent1Loc_minSC = zeros(x1size,fsize,gsize);
   % Junction 2
      PhaseDrop2_minSC = zeros(x2size,fsize,gsize);
      SCurrent2Loc_minSC = zeros(x2size,fsize,gsize);

%% Main Body of the Simulation
for g = 1: gsize
    for f=1:fsize
      %Combining Phase drops to find the local drops across the junction
      PhaseE1 = Phase1F(:,f)*ones(1,psize);
      PhaseDrop1 = ones(x1size,1)*PhaseA+PhaseE1;

      PhaseE2 = Phase2F(:,f)*ones(1,psize)+ PhaseSF(:,f)*ones(1,psize);
      PhaseDrop2 = ones(x2size,1)*PhaseA+PhaseE2;

      %Calculating the matrix that is the current (SCurrentLoc) across
      %the junction at each position for each value of PhaseA.
      SCurrentLoc1 = SCurrent1Density*ones(1,psize).*sin(PhaseDrop1);
      SCurrentLoc2 = SCurrent2Density*ones(1,psize).*sin(PhaseDrop2);

      %Numerically integrating the Super Current (SCurrentLoc) along the
      %junction at each PhaseA to find the total super current carried.
      SCurrentNet1 = sum(SCurrentLoc1); %sums along x to get a row
      SCurrentNet2 = sum(SCurrentLoc2); %sums along x to get a row
      SCurrentNetTot = SCurrentNet1 + SCurrentNet2;

      %Finding the Magnitude and the Index of the maximum
      %supercurrent across the junction at the current field strength
      [SCurrentNet_max(1,f,g),Index_max(f,g)] = max(SCurrentNetTot);

      %Recording the interesting values when the current is maximized
      PhaseA_maxSC(1,f,g) = PhaseA(1,Index_max(f,g)); % vector (radians)

      PhaseDrop1_maxSC (:,f,g) = PhaseDrop1(:,Index_max(f,g));
      PhaseDrop2_maxSC (:,f,g) = PhaseDrop2(:,Index_max(f,g));
```

```
        SCurrent1Loc_maxSC (:,f,g) = SCurrentLoc1(:,Index_max(f,g));
        SCurrent2Loc_maxSC (:,f,g) = SCurrentLoc2(:,Index_max(f,g));

        %Finding the Magnitude and the Index of the minimum
        %supercurrent across the junction at the current field strength
        [SCurrentNet_min(1,f,g),Index_min(f,g)] = min(SCurrentNetTot);

        %Recording the interesting values when the current is minimized
        PhaseA_minSC(1,f,g) = PhaseA(1,Index_min(f,g)); % vector (radians)

        PhaseDrop1_minSC (:,f,g) = PhaseDrop1(:,Index_min(f,g));
        PhaseDrop2_minSC (:,f,g) = PhaseDrop2(:,Index_min(f,g));

        SCurrent1Loc_minSC (:,f,g) = SCurrentLoc1(:,Index_min(f,g));
        SCurrent2Loc_minSC (:,f,g) = SCurrentLoc2(:,Index_min(f,g));
    end
end
%% Plotting Relevant Data
%Ploting the maximum supercurrent vs the field in the junction
figure; subplot(2,1,1);
    plot(FluxinJunc,squeeze(SCurrentNet_max),'.'); hold on;
    plot(FluxinJunc,squeeze(SCurrentNet_min),'.');

    ylabel('Critical Current (I_c)');
    ylim([1.05*min(min(SCurrentNet_min)) 1.05*max(max(SCurrentNet_max))]);
    title('SQuID with Varying Asymmetry  ');
    legend(num2str(transpose(chop(Gpar,3))));

%Ploting the PhaseA value that maximizes the critical current
subplot(2,1,2);
    plot(FluxinJunc,squeeze(PhaseA_maxSC)/pi,'.'); hold on;
    plot(FluxinJunc,squeeze(PhaseA_minSC)/pi,'.');
    xlabel('Applied Flux per Unit Area (\Phi_0)');
    ylabel('\phi_A (\pi)'); ylim([PhaseA_min/pi PhaseA_max/pi]);
```

A.3.2 JJSimV05_SQuID_AsymSin2phiCPR.m

```
%% JJSimV05_SQuID_AsymSin2phiCPR.m
 % written by Erik Huemiller

 % The goal of this version of the program is to adapt JJSimV04 to be able
 % to simulate exotic physics in the CPR measurement.  This includes adding
 % a sin(2phi) term tothe CPR and changing its strength.

%% Clearing memory and input screen.
clear; clc; close all;
%% Defining the Parameters of the Simulaiton
```

```
%Dividing the junction up into discrete sections
   % Junction 1
      x1min = -100;
      x1max =  0;
      x1_area = .01;
      x1size=x1max-x1min+1;
      x1(1:x1size,1) = (1:x1size)-1+x1min;
      x1norm = x1_area * x1/x1size;
   % Junction 2
      x2min = 0;
      x2max =  101;
      x2_area = .01;
      x2size=x2max-x2min+1;
      x2(1:x2size,1) = (1:x2size)-1+x2min;
      x2norm = x2_area * x2/x2size;

%Defining Super Current parameters
   % Junction 1
      SCurrent1Mag = .1;
      SCurrentNoise1Mag = 0.01;
      SCurrentNoise1 = (SCurrentNoise1Mag/x1size*(2*rand(x1size,1,1)-1));
   % Junction 2
      SCurrent2Mag = 1;
      SCurrentNoise2Mag = 0.01;
      SCurrentNoise2 = (SCurrentNoise2Mag/x2size*(2*rand(x2size,1,1)-1));
   % SQuID loop area
      SLarea = 1;

%Setting up Sweep Parameters
   %Phase Vector Generation, will be the column (2nd index)
      psize = 201;
      PhaseA_min = -1.0 * pi;
      PhaseA_max =  1.0 * pi;
      PhaseA_SS = (PhaseA_max-PhaseA_min)/(psize-1);
      PhaseA = PhaseA_min:PhaseA_SS:PhaseA_max;% vector (radians)

   %Flux Vector Generation, will be the 'f' loop
      fsize = 501; f=1;
      FluxinJunc_min = -5;
      FluxinJunc_max =  5 ;
      FluxinJunc_SS = (FluxinJunc_max-FluxinJunc_min) / (fsize-1);
      FluxinJunc(1,:) = FluxinJunc_min:FluxinJunc_SS:FluxinJunc_max;
      Phase1F = 2*pi * x1norm * FluxinJunc; % vector in units of radians
      Phase2F = 2*pi * x2norm * FluxinJunc; % vector in units of radians
      PhaseSF = 2*pi * ones(x2size,1)* SLarea * FluxinJunc;
```

```
   %Iteration Vector Generation, will be the 'g' parameter loop
      gsize=4; g=1;
      Gpar_min = 0;
      Gpar_max = 1 ;
      Gpar_SS = (Gpar_max-Gpar_min) / (gsize-1);
      Gpar(1,:) = Gpar_min:Gpar_SS:Gpar_max;

%Calculating Parameters from Initial Conditions
   SCurrent1Density = (SCurrent1Mag/x1size*ones(x1size,1)+SCurrentNoise1);
   SCurrent2Density = (SCurrent2Mag/x2size*ones(x2size,1)+SCurrentNoise2);

%Pre Allocating memory for maximum critical current
      SCurrentNet_max = zeros(1,fsize,gsize);
      Index_max = zeros(1,fsize,gsize);
      PhaseA_maxSC = zeros(1,fsize,gsize);
   % Junction 1
      PhaseDrop1_maxSC = zeros(x1size,fsize,gsize);
      SCurrent1Loc_maxSC = zeros(x1size,fsize,gsize);
   % Junction 2
      PhaseDrop2_maxSC = zeros(x2size,fsize,gsize);
      SCurrent2Loc_maxSC = zeros(x2size,fsize,gsize);

%Pre Allocating memory for minimum critical current
      SCurrentNet_min = zeros(1,fsize,gsize);
      Index_min = zeros(1,fsize,gsize);
      PhaseA_minSC = zeros(1,fsize,gsize);
   % Junction 1
      PhaseDrop1_minSC = zeros(x1size,fsize,gsize);
      SCurrent1Loc_minSC = zeros(x1size,fsize,gsize);
   % Junction 2
      PhaseDrop2_minSC = zeros(x2size,fsize,gsize);
      SCurrent2Loc_minSC = zeros(x2size,fsize,gsize);
%% Main Body of the Simulation
for g = 1: gsize
    for f=1:fsize
      %Combining Phase drops to find the local drops across the junction
      PhaseE1 = Phase1F(:,f)*ones(1,psize);
      PhaseDrop1 = ones(x1size,1)*PhaseA+PhaseE1;

      PhaseE2 = Phase2F(:,f)*ones(1,psize)+ PhaseSF(:,f)*ones(1,psize);
      PhaseDrop2 = ones(x2size,1)*PhaseA+PhaseE2;

      %Calculating the matrix that is the current (SCurrentLoc) across
      %the junction at each position for each value of PhaseA.
      SCurrentLoc1 =
(1)*SCurrent1Density*ones(1,psize).*(sin(PhaseDrop1)+Gpar(g)*sin(2*PhaseDrop1));
```

```
        SCurrentLoc2 =
(1)*SCurrent2Density*ones(1,psize).*(sin(PhaseDrop2)+Gpar(g)*sin(2*PhaseDrop2));

        %Numerically integrating the Super Current (SCurrentLoc) along the
        %junction at each PhaseA to find the total super current carried.
        SCurrentNet1 = sum(SCurrentLoc1); %sums along x to get a row
        SCurrentNet2 = sum(SCurrentLoc2); %sums along x to get a row
        SCurrentNetTot = SCurrentNet1 + SCurrentNet2;

        %Finding the Magnitude and the Index of the maximum
        %supercurrent across the junction at the current field strength
        [SCurrentNet_max(1,f,g),Index_max(f,g)] = max(SCurrentNetTot);

        %Recording the interesting values when the current is maximized
        PhaseA_maxSC(1,f,g) = PhaseA(1,Index_max(f,g)); % vector (radians)

        PhaseDrop1_maxSC (:,f,g) = PhaseDrop1(:,Index_max(f,g));
        PhaseDrop2_maxSC (:,f,g) = PhaseDrop2(:,Index_max(f,g));

        SCurrent1Loc_maxSC (:,f,g) = SCurrentLoc1(:,Index_max(f,g));
        SCurrent2Loc_maxSC (:,f,g) = SCurrentLoc2(:,Index_max(f,g));

        %Finding the Magnitude and the Index of the minimum
        %supercurrent across the junction at the current field strength
        [SCurrentNet_min(1,f,g),Index_min(f,g)] = min(SCurrentNetTot);

        %Recording the interesting values when the current is minimized
        PhaseA_minSC(1,f,g) = PhaseA(1,Index_min(f,g)); % vector (radians)

        PhaseDrop1_minSC (:,f,g) = PhaseDrop1(:,Index_min(f,g));
        PhaseDrop2_minSC (:,f,g) = PhaseDrop2(:,Index_min(f,g));

        SCurrent1Loc_minSC (:,f,g) = SCurrentLoc1(:,Index_min(f,g));
        SCurrent2Loc_minSC (:,f,g) = SCurrentLoc2(:,Index_min(f,g));
    end
end
%% Plotting Relevant Data
%Ploting the maximum supercurrent vs the field in the junction
figure; subplot(2,1,1);
   plot(FluxinJunc,squeeze(SCurrentNet_max),'.'); hold on;
   %plot(FluxinJunc,squeeze(SCurrentNet_min),'.');

   ylabel('Critical Current (I_c)');
   ylim([0.95*min(min(SCurrentNet_max)) 1.05*max(max(SCurrentNet_max))]);
   title('SQuID with Varying sin(2\phi) Strength  ');
   legend(num2str(transpose(chop(Gpar,2))));
```

```
%Ploting the PhaseA value that maximizes the critical current
subplot(2,1,2);
   plot(FluxinJunc,squeeze(PhaseA_maxSC)/pi,'.'); hold on;
   %plot(FluxinJunc,squeeze(PhaseA_minSC)/pi,'.');
   xlabel('Applied Flux per Unit Area (\Phi_0)');
   ylabel('\phi_A (\pi)'); ylim([PhaseA_min/pi PhaseA_max/pi]);
```

A.3.3 JJSimV05_SQuID_SQuIDtoJJcrossover.m

```
%% JJSimV05_SQuID_SQuIDtoJJcrossover.m
 % written by Erik Huemiller

 % The goal of this version of the program is to adapt JJSimV04 to be able
 % to simulate the area crossover region between single junction physics
 % and SQuID physics.

%% Clearing memory and input screen.
clear; clc; close all;
%% Defining the Parameters of the Simulaiton
%Dividing the junction up into discrete sections
   % Junction 1
      x1min = -100;
      x1max =  0;
      x1_area = .5;
      x1size=x1max-x1min+1;
      x1(1:x1size,1) = (1:x1size)-1+x1min;
      x1norm = x1_area * x1/x1size;
   % Junction 2
      x2min = 0;
      x2max =  101;
      x2_area = .5;
      x2size=x2max-x2min+1;
      x2(1:x2size,1) = (1:x2size)-1+x2min;
      x2norm = x2_area * x2/x2size;

%Defining Super Current parameters
   % Junction 1
      SCurrent1Mag = 1;
      SCurrentNoise1Mag = 0.01;
      SCurrentNoise1 = (SCurrentNoise1Mag/x1size*(2*rand(x1size,1,1)-1));
   % Junction 2
      SCurrent2Mag = 1;
      SCurrentNoise2Mag = 0.01;
      SCurrentNoise2 = (SCurrentNoise2Mag/x2size*(2*rand(x2size,1,1)-1));
   % SQuID loop area
      SLarea = 1;
```

```
%Setting up Sweep Parameters
   %Phase Vector Generation, will be the column (2nd index)
      psize = 501;
      PhaseA_min = -1.0 * pi;
      PhaseA_max =  1.0 * pi;
      PhaseA_SS = (PhaseA_max-PhaseA_min)/(psize-1);
      PhaseA = PhaseA_min:PhaseA_SS:PhaseA_max;% vector (radians)

   %Flux Vector Generation, will be the 'f' loop
      fsize = 801; f=1;
      FluxinJunc_min = -4;
      FluxinJunc_max =  4 ;
      FluxinJunc_SS = (FluxinJunc_max-FluxinJunc_min) / (fsize-1);
      FluxinJunc(1,:) = FluxinJunc_min:FluxinJunc_SS:FluxinJunc_max;
%        Phase1F = 2*pi * 0.1 * x1norm * FluxinJunc; % vector in units of radians
%        Phase2F = 2*pi * 0.1 * x2norm * FluxinJunc; % vector in units of radians
%        PhaseSF = 2*pi * ones(x2size,1)* SLarea * FluxinJunc;

   %Iteration Vector Generation, will be the 'g' parameter loop
      gsize=3; g=1;
      Gpar_min = 0;
      Gpar_max = 1 ;
%        Gpar_SS = (Gpar_max-Gpar_min) / (gsize-1);
%        Gpar(1,:) = Gpar_min:Gpar_SS:Gpar_max;
      Gpar(1,:) = [0 0.75 1];

%Calculating Parameters from Initial Conditions
   SCurrent1Density = (SCurrent1Mag/x1size*ones(x1size,1)+SCurrentNoise1);
   SCurrent2Density = (SCurrent2Mag/x2size*ones(x2size,1)+SCurrentNoise2);

%Pre Allocating memory for maximum critical current
      SCurrentNet_max = zeros(1,fsize,gsize);
      Index_max = zeros(1,fsize,gsize);
      PhaseA_maxSC = zeros(1,fsize,gsize);
   % Junction 1
      PhaseDrop1_maxSC = zeros(x1size,fsize,gsize);
      SCurrent1Loc_maxSC = zeros(x1size,fsize,gsize);
   % Junction 2
      PhaseDrop2_maxSC = zeros(x2size,fsize,gsize);
      SCurrent2Loc_maxSC = zeros(x2size,fsize,gsize);

%Pre Allocating memory for minimum critical current
      SCurrentNet_min = zeros(1,fsize,gsize);
      Index_min = zeros(1,fsize,gsize);
      PhaseA_minSC = zeros(1,fsize,gsize);
```

```
    % Junction 1
      PhaseDrop1_minSC = zeros(x1size,fsize,gsize);
      SCurrent1Loc_minSC = zeros(x1size,fsize,gsize);
    % Junction 2
      PhaseDrop2_minSC = zeros(x2size,fsize,gsize);
      SCurrent2Loc_minSC = zeros(x2size,fsize,gsize);

%% Main Body of the Simulation
for g = 1: gsize
   Phase1F = 2*pi * Gpar(g) * x1norm * FluxinJunc; % vector in units of radians
   Phase2F = 2*pi * Gpar(g) * x2norm * FluxinJunc; % vector in units of radians
   PhaseSF = 2*pi * (1-Gpar(g))* ones(x2size,1)* SLarea * FluxinJunc;
    for f=1:fsize
      %Combining Phase drops to find the local drops across the junction
      PhaseE1 = Phase1F(:,f)*ones(1,psize);
      PhaseDrop1 = ones(x1size,1)*PhaseA+PhaseE1;

      PhaseE2 = Phase2F(:,f)*ones(1,psize)+ PhaseSF(:,f)*ones(1,psize);
      PhaseDrop2 = ones(x2size,1)*PhaseA+PhaseE2;

      %Calculating the matrix that is the current (SCurrentLoc) across
      %the junction at each position for each value of PhaseA.
      SCurrentLoc1 = SCurrent1Density*ones(1,psize).*sin(PhaseDrop1);
      SCurrentLoc2 = SCurrent2Density*ones(1,psize).*sin(PhaseDrop2);

      %Numerically integrating the Super Current (SCurrentLoc) along the
      %junction at each PhaseA to find the total super current carried.
      SCurrentNet1 = sum(SCurrentLoc1); %sums along x to get a row
      SCurrentNet2 = sum(SCurrentLoc2); %sums along x to get a row
      SCurrentNetTot = SCurrentNet1 + SCurrentNet2;

      %Finding the Magnitude and the Index of the maximum
      %supercurrent across the junction at the current field strength
      [SCurrentNet_max(1,f,g),Index_max(f,g)] = max(SCurrentNetTot);

      %Recording the interesting values when the current is maximized
      PhaseA_maxSC(1,f,g) = PhaseA(1,Index_max(f,g)); % vector (radians)

      PhaseDrop1_maxSC (:,f,g) = PhaseDrop1(:,Index_max(f,g));
      PhaseDrop2_maxSC (:,f,g) = PhaseDrop2(:,Index_max(f,g));

      SCurrent1Loc_maxSC (:,f,g) = SCurrentLoc1(:,Index_max(f,g));
      SCurrent2Loc_maxSC (:,f,g) = SCurrentLoc2(:,Index_max(f,g));

      %Finding the Magnitude and the Index of the minimum
      %supercurrent across the junction at the current field strength
```

```
        [SCurrentNet_min(1,f,g),Index_min(f,g)] = min(SCurrentNetTot);

        %Recording the interesting values when the current is minimized
        PhaseA_minSC(1,f,g) = PhaseA(1,Index_min(f,g)); % vector (radians)

        PhaseDrop1_minSC (:,f,g) = PhaseDrop1(:,Index_min(f,g));
        PhaseDrop2_minSC (:,f,g) = PhaseDrop2(:,Index_min(f,g));

        SCurrent1Loc_minSC (:,f,g) = SCurrentLoc1(:,Index_min(f,g));
        SCurrent2Loc_minSC (:,f,g) = SCurrentLoc2(:,Index_min(f,g));
    end
end
%% Plotting Relevant Data
%Ploting the maximum supercurrent vs the field in the junction
figure; subplot(2,1,1);
   plot(FluxinJunc,squeeze(SCurrentNet_max),'.'); hold on;
   %plot(FluxinJunc,squeeze(SCurrentNet_min),'.');

   ylabel('Critical Current (I_c)');
   ylim([-.05 1.05*max(max(SCurrentNet_max))]);
   title('SQuID to JJ Transition  ');
   legend(num2str(transpose(chop(Gpar,3))));

%Ploting the PhaseA value that maximizes the critical current
subplot(2,1,2);
   plot(FluxinJunc,squeeze(PhaseA_maxSC)/pi,'.'); hold on;
   %plot(FluxinJunc,squeeze(PhaseA_minSC)/pi,'.');
   xlabel('Applied Flux per Unit Area (\Phi_0)');
   ylabel('\phi_A (\pi)'); ylim([PhaseA_min/pi PhaseA_max/pi]);
```

A.4 Apendix A Bibliography

[1] F. Kidwingira, J. D. Strand, D. J. Van Harlingen, and Y. Maeno, "Dynamical superconducting order parameter domains in Sr2RuO4.," *Science*, vol. 314, no. 5803, pp. 1267–71, Nov. 2006.

[2] Dan Bahr, "Probing the Chiral Domain Structure and Dynamics in Sr2RuO4 with nanoscale JJs," *Dissertation*, 2011.

[3] D. Wollman and D. Van Harlingen, "Evidence for d . y. Pairing from the Magnetic Field Modulation of YBa2Cu307-Pb Josephson Junctions," *Phys. Rev. ...*, vol. 74, no. 5, pp. 797–801, 1995.

[4] C. Kurter, A. D. K. Finck, Y. S. Hor, and D. J. Van Harlingen, "Evidence for an anomalous current-phase relation of a dc SQUID with tunable topological junctions," *arXiv Prepr. arXiv*.

[5] M. Tinkham, *Introduction to superconductivity*. 1996.

[6] J. Clarke and A. Braginski, *The SQUID Handbook: Fundamentals and Technology of SQUIDS and SQUID Systems*, vol. 21, no. 5. 2004.

[7] D. A. Wollman, D. J. Van Harlingen, W. C. Lee, D. M. Ginsberg, and A. J. Leggett, "Experimental Determination of Supercondcuting Pairing State in YBCO from Phase Coherence of YBCO0PB dc Squids," *PRL*, vol. 71, no. 13, pp. 2134–2137, 1993.

[8] G. Nanda, P. Rakyta, R. Kleiner, D. Koelle, K. Watanabe, T. Taniguchi, L. M. K. Vandersypen, and S. Goswami, "Current-Phase Relation of Ballistic Graphene Josephson Junctions," 2017.